Eliminating Out-of-Band Loss in Thermophotovoltaic Systems Utilizing Cell-Side Spectral Control

by

Tobias E. Burger

A dissertation submitted in partial fulfillment
of the requirements for the degree of
Doctor of Philosophy
(Chemical Engineering)
in the University of Michigan
2022

Doctoral Committee:

Assistant Professor Andrej Lenert, Chair
Professor Stephen R. Forrest
Assistant Professor Xiwen Gong
Professor Suljo Linic

Tobias E. Burger

tobiasbu@umich.edu

ORCID iD: 0000-0002-2815-0591

Dedication

To my father, Art, and my mother, Julie

To my partner, Katey

Acknowledgments

I would not have been able to achieve this lifelong dream without the support of many people in my life. I would like to take this opportunity to thank those who have helped me personally and academically in the pursuit of my Ph.D.

First and foremost, I would like to thank my advisor, Dr. Andrej Lenert. Andrej, you have been a thoughtful mentor and a patient teacher. Thank you for doing the painstaking work of teaching me to clearly communicate my research. Thank you for being just as excited as I am when I show up to our meetings with good results. And lastly, thank you for valuing my input and treating me as your partner in research. I wouldn't be the researcher I am today without your mentorship.

To the members of the Lenert lab, Sean, Zach, Hannah, Bosun, and Alex, thank you for making research fun. It's been an absolute privilege to share this experience with you. Bosun, you have mastered fabrication techniques and started developing your own processes in remarkable time. I can't wait to see what you do next.

To my research mentor, Dr. Dejiu Fan, thank you for taking me under your wing during the early years of my graduate studies. I owe all of my cleanroom and fabrication expertise to you. I couldn't have accomplished the works in this thesis without your contributions.

I would also like to acknowledge my other research collaborators. Thank you, Prof. Forrest, Byungjun, Rebecca, Jihun, Bosun, Sean, Caroline, and Vinod for your contributions to this thesis.

On a more personal note, I'd like to thank my life-long friends from back home and the friends I've made during my time in graduate school. To Seth, Nick, Mitch, Danielle, Paul, Sean, Rachel, Patrick, Emily, Zach, Alex, Ben, Jacques, and others – thank you for helping to make my time in Ann Arbor one of the best chapters of my life so far. I've made lifelong friends here, and I'll miss you so much when I leave.

To my father, Art, and my mother, Julie, thank you for everything you have given me. Thank you for getting me into soccer and for attending all my games. Thank you for driving me to Socorro for the state science fair and for taking me out to dinner when I lost. Thank you for inspiring me to do great things with my life and putting me in a position to succeed when I try. I couldn't have done any of this without your support.

Lastly, I want to thank my partner, Katey. You've made this all worthwhile. I can't wait to see what's next for us.

Table of Contents

List of Tables

List of Figures

Abstract

Thermophotovoltaic (TPV) generators have emerged as promising heat engines for use in a wide range of emerging energy generation and storage applications. This approach to energy conversion leverages the photovoltaic effect to convert locally emitted thermal radiation (heat) to electrical power. TPVs are positioned to facilitate the growth of intermittent, renewable energy sources because they can deliver power quickly and efficiently in response to sudden changes in energy demand at various scales. Through integration with thermal batteries, TPVs may enable one of the most affordable and energy-dense approaches for grid-scale electricity storage. TPVs are further well-suited for utilization in distributed co-generation, an alternative to centralized power generation that may reduce energy loss associated with waste heat and electricity transmission.

Despite the appeal of TPVs for use in these promising energy generation and storage technologies, TPV conversion efficiencies remain well below their thermodynamic limits. Practical deployment of the technology is therefore predicated on continued advances in performance. The fundamental challenge of thermophotovoltaics pertains to regulation of the radiative heat transfer between the thermal emitter and the photovoltaic cell. Given the moderate temperature of the thermal emitter, only a small fraction (~20%) of power is usable by the photovoltaic cell. The remaining, unusable power must be properly managed to avoid substantial loss. The present work aims to eliminate radiative loss in thermophotovoltaic systems to improve their conversion efficiencies.

This thesis begins with an exhaustive review of the TPV literature that features a thermodynamic framework for meaningful comparison of dissimilar works. This review helps to recognize leading materials and design choices and identifies opportunities for continued improvements. Spectral inefficiencies are shown to persist as the largest loss pathway for TPVs.

The first of three experimental demonstrations herein involves the realization of thin-film InGaAs optical structures through non-destructive epitaxial techniques. This technique enables recovery and subsequent reuse of the expensive crystalline growth substrate for reduced cell costs. Further, optimized dielectric claddings are shown to improve the spectral performance of the optical structures. Specifically, use of a MgF_2 rear spacer enables record-high out-of-band reflectance of 96%, an improvement over cells with conventional metallic rear reflectors.

Secondly, this thesis demonstrates a novel cell architecture featuring air pockets buried beneath a InGaAs/InP heterostructure absorber with near-complete (98.5%) reflectance of out-of-band power. This spectral advance enables record-high conversion efficiency of 32% under illumination by a 1455K SiC emitter, representing an 8% efficiency improvement over a control cell.

Lastly, this thesis describes the development of an entirely new approach to spectral management based on partially transparent cells. Optical analysis of a proof-of-concept optical structure decouples radiative loss in the heterostructure absorber and the supporting substrate to show a pathway to a new regime featuring <1% out-of-band absorptance. Beyond improved conversion efficiency, mitigation of radiative loss as presented here may enable expansion of the TPV application space to include cell materials and heat sources previously considered impractical.

Chapter 1: Introduction

1.1 Thermophotovoltaic energy conversion

Thermophotovoltaic (TPV) generators utilize the photovoltaic effect to convert heat into electrical power (Figure 1.1). Many potential heat sources can be interfaced with TPVs, including combustion of fossil fuels, nuclear power, concentrated solar thermal, variable renewable electricity, and high-temperature waste heat streams. As heat is supplied to the thermal emitter, it drives radiative emission to the cold-side photovoltaic cell. Absorption of high-energy (in-band) photons in the cell excites electron-hole pairs, while low-energy (out-of-band) thermal radiation may be suppressed or recuperated to minimize the heat input. Ultimately, photoexcited carriers are separated, inducing a voltage across the junction that drives current across a load.

In many ways, thermophotovoltaic generators are similar to solar photovoltaic systems. Both technologies utilize the photovoltaic effect to convert absorbed photons to usable electrical power. They differ, however, because of differences in the nature of the heat source (i.e., the emitter). Solar PV cells convert visible and UV photons emitted by the sun, which has a temperature of ~5800K. Thermal emitters in TPV systems, on the other hand, typically operate in the range of 1000-2000K. Therefore, photons are largely emitted in the IR. As a consequence, TPV cells are generally comprised of narrow bandgap absorbers that are photosensitive to the emitted thermal

radiation. Further, because of the relative proximity of the emitter to the cell, the intensity of incident radiation is greater than solar incidence. Therefore, the resulting power density is typically >100x higher than that of solar photovoltaics.

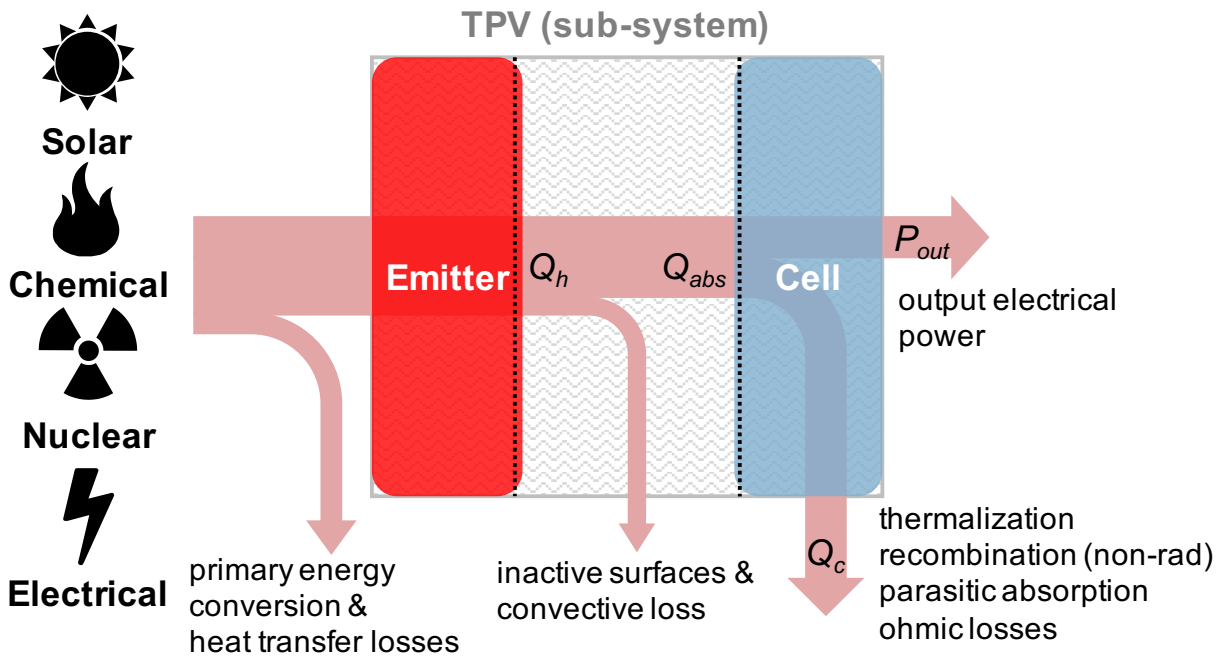

Figure 1.1. Energy transport and conversion in a thermophotovoltaic generator. Upstream conversion of an energy source heats the thermal emitter, generating radiation that interacts with the cell. Photoexcitation (by in-band radiation) and separation of charge carriers in the cell enables power generation (P_{out}). A portion of incident radiation is reflected by the cell and returned to the emitter (i.e., photon recycling/recuperation). Q_h denotes net energy flow out of the emitter and Q_{abs} denotes radiation absorbed at the cell. Loss pathways within the TPV sub-system include (i) emission to non-current-generating surfaces in the cavity (e.g., edges, contact lines, etc.) and convective loss from the emitter, and (ii) cell inefficiencies, such as thermalization, non-radiative recombination, out-of-band absorption, and Ohmic losses. Upstream inefficiencies related to conversion of the energy source and heat transfer to the emitter depend on the source and are not attributed to the TPV sub-system in this work.

1.2 Application space

1.2.1 Power on demand

TPV generators offer several advantages over conventional cycles owing to their ability to respond quickly to sudden electricity demands on the electrical grid.[1,2] Grid-scale storage is increasingly necessary to facilitate a transition from fossil fuels to intermittent renewable energy sources, such as solar and wind. Beyond reducing carbon emissions, diversification of primary energy sources and implementation of rapidly dispatchable power can help improve grid resilience. Studies suggest that TPVs may offer competitive modular costs, lower maintenance costs, and faster ramp rates than combined cycle systems.[2,3] Further, solid-state engines like TPVs are well-suited for operation with constant-temperature heat, whereas turbines suffer from entropic losses associated with heating of the working fluid.[3] In one envisioned application (Figure 1.2a), a high-temperature thermal energy storage material, such as Si, could offer energy storage for up to several months.[1] Charging would be accomplished via resistive heating, while TPV generators would be used to discharge the stored thermal energy during periods of high demand. This approach to energy storage is expected to offer higher energy densities and lower cost of energy than electrochemical approaches, such as Li-ion batteries.

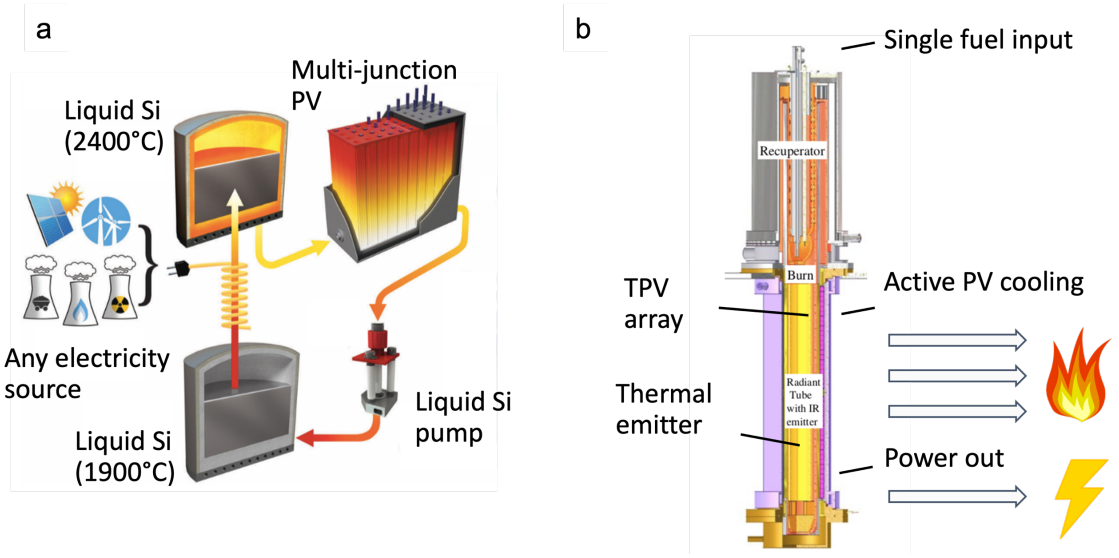

Figure 1.2. Thermophotovoltaics in energy generation and storage applications. (a) Schematic of proposed thermal energy grid storage application. Electricity is converted to heat through Joule heating, then stored in a high-temperature liquid medium. TPV panels may then be used to convert stored heat back to electricity during periods of high demand. Reproduced with permission from Ref. [1] Copyright Royal Society of Chemistry. (b) Schematic of proposed thermophotovoltaic generator with electrical and thermal output for small-scale co-generation. Reproduced with permission from Ref. [4] Copyright IOP Publishing.

1.2.2 Power near the point of use

The solid-state design of TPV generators makes the technology suitable for small-scale power generation near the point of use (i.e., kW scale). This approach may eliminate losses inherent to MW scale energy production, far from the point of use, by eliminating transmission losses and enabling the functional utilization of waste heat for space and water heating. The feasibility of using TPVs for residential co-generation has been evaluated through detailed system design and simulation,[5] economic analysis,[6] and development of a compact furnace-generator[4] (Figure 1.2b).

1.2.3 Wafer reuse for decreased cell costs

TPVs remain prohibitively expensive for widespread use in these and other application spaces. Specifically, the high-quality growth substrates required for fabrication of high-performance cells

persist as the largest single cost of TPV modules.[7] Recovery of a substrate and subsequent reuse for growth of multiple cells can therefore reduce module costs considerably. Recent advances in semiconductor manufacturing have enabled fabrication of high-quality, thin-film (<10 μm) cells, characterized by the removal of the parent wafer after growth,[8–10] but reuse of the substrate after removal has not yet been demonstrated for cells in TPV systems. Recovery of the substrate requires non-destructive liftoff of the epitaxial layer(s), which has been experimentally realized previously outside the field of TPVs.[11,12] Widespread implementation of TPVs will likely necessitate adaptation of this approach to reduce cell costs.

1.3 Conversion efficiency as a figure of merit

Despite the appeal of TPVs for a range of applications, current TPV generators operate at conversion efficiencies well below their thermodynamic limits. Thermophotovoltaic conversion efficiency η_{TPV} is defined as the ratio of output power P_{out} to the net energy flow out of the emitter Q_h.

$$\eta_{TPV} = \frac{P_{out}}{Q_h} \tag{1.1}$$

This metric is largely dependent on how effectively energy losses are mitigated at each conversion step. Important loss pathways include emission and absorption of out-of-band photons, thermalization of in-band photons, electron-hole pair recombination, Ohmic losses along the current conduction pathway, and parasitic heat losses to the surroundings.

To gain a better understanding of how these loss pathways affect performance, η_{TPV} is further written in terms of a product of several performance metrics:

$$\eta_{TPV} = \frac{P_{out}}{Q_h} = (SE \cdot IQE)(VF)(FF)(CE) \tag{1.2}$$

where *SE* is spectral efficiency, *IQE* is internal quantum efficiency, *VF* is voltage factor, *FF* is fill factor, and *CE* is cavity efficiency. Individually, these metrics are defined as:

$$\eta_{TPV} = \left(\frac{J_{sc}V_g}{Q_{abs}}\right)\left(\frac{V_{oc}}{V_g}\right)\left(\frac{P_{out}}{J_{sc}V_{oc}}\right)\left(\frac{Q_{abs}}{Q_h}\right) \tag{1.3}$$

Where J_{sc} is the short-circuit current, V_g is the bandgap voltage, and V_{oc} is the open-circuit voltage.

1.3.1 Spectral management

The product of *SE* and *IQE* quantitatively describes the conversion of radiative heat absorbed by the cell Q_{abs} into short-circuit current J_{sc} multiplied by the cell bandgap voltage V_g, as shown in Equation 1.3. This product is a measure of how effectively radiative power is managed by the cell and emitter (i.e., spectral management).

(i) Spectral efficiency

While emission and subsequent absorption of in-band photons are necessary for power generation, suppression and/or reflection of out-of-band photons are, concurrently, critical for achieving high conversion efficiency.[13] Spectral efficiency *SE* captures the importance of both considerations.

$$SE = \frac{E_g \cdot \int_{E_g}^{\infty} \varepsilon_{eff}(E) \cdot b(E,T_h)\, dE}{\int_0^{\infty} \varepsilon_{eff}(E) \cdot E \cdot b(E,T_h)\, dE} \tag{1.4}$$

Here, E is photon energy, E_g is the bandgap energy, and T_h is the hot side (i.e., thermal emitter) temperature. The blackbody spectral photon flux $b(E,T)$ is given by:

$$b(E,T) = \frac{2\pi E^2}{c^2 h^3 \left(\exp\left(\frac{E}{k_B T}\right) - 1\right)} \tag{1.5}$$

where c is the speed of light in vacuum, h is Planck's constant, and k_B is Boltzmann's constant. The effective spectral emissivity of the emitter-cell pair, ε_{eff}, is given by:

$$\varepsilon_{eff} = \frac{\varepsilon_e \varepsilon_c}{\varepsilon_e + \varepsilon_c - \varepsilon_e \varepsilon_c} \tag{1.6}$$

where ε_e is the emitter emissivity and ε_c is the cell emissivity. Equivalently, the effective spectral emissivity can be written in terms of the spectral reflectance of the emitter, R_e, and of the cell, R_c[9]:

$$\varepsilon_{eff} = \frac{(1-R_e)(1-R_c)}{1-R_e R_c} \tag{1.7}$$

The spectral efficiency discussed here shares similarities with the photon over-excitation factor[14] and the ultimate efficiency.[13] However, *SE* considers the net radiative exchange between the emitter and the PV cell, thereby considering the effects of multiple reflections across the cavity. Notably, spectral efficiency is a function of both the spectral emissivity of the thermal emitter and the PV cell.

SE shares the same upper bound as the ultimate efficiency, which is shown in Figure 1.3 for a cell or an emitter with a single cutoff energy, E_{cutoff}, that matches the bandgap. For a finite, out-of-band emissivity, $\varepsilon_{out,}$ there is an optimal bandgap which maximizes the spectral efficiency. This optimum arises because of the tradeoff between photocurrent and bandgap energy – i.e., for a given emission temperature, the photocurrent decreases as the bandgap increases.

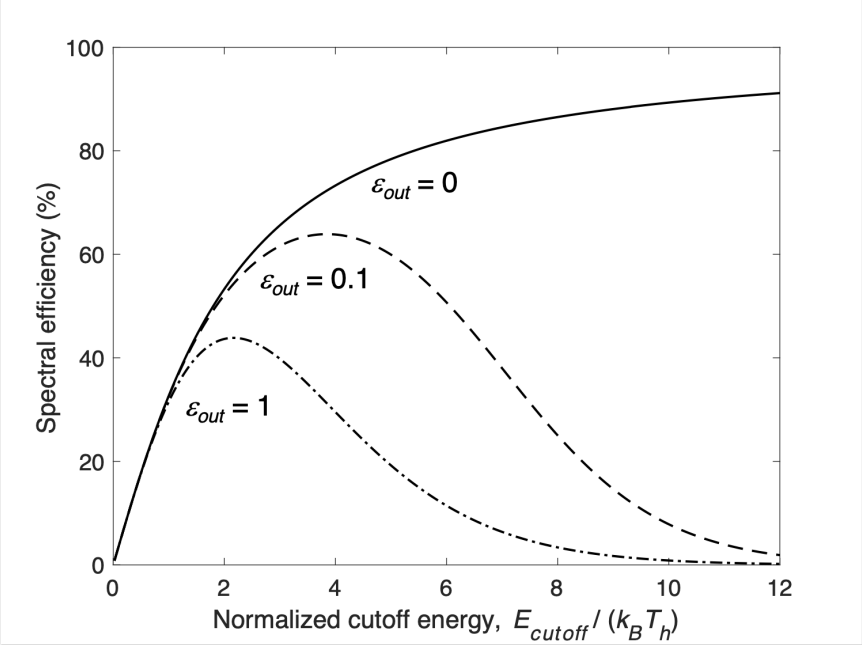

Figure 1.3. Spectral efficiency limits. Spectral efficiency shown as a function of normalized cutoff energy for perfect in-band (i.e., above-bandgap) absorption ($\varepsilon_{in} = 1$). Limits are calculated for three out-of-band (i.e., sub-bandgap) conditions: total suppression ($\varepsilon_{out} = 0$), intermediate suppression ($\varepsilon_{out} = 0.1$), and no suppression ($\varepsilon_{out} = 1$).

Spectral inefficiencies affecting *SE* include absorption of out-of-band photons, reflectance of in-band photons, and thermalization (i.e., relaxation) of carriers following absorption of high-energy in-band photons. Figure 1.4 shows how control of the radiative exchange may be engineered at the hot side, (i.e., emissive spectral control) and at the cold side (i.e., absorptive spectral control). While intrinsic material properties alone offer limited spectral control for TPV generators, targeted engineering of components has been shown to promote above-bandgap photon transport and impede sub-bandgap transport. Photonic design of emitter micro-scale geometry is a common strategy to promote above-bandgap emission while simultaneously suppressing sub-bandgap emission at the hot side. While strategies for absorptive spectral control at the PV cell typically consist of the use of front-surface filters (FSFs) and/or back-surface reflectors (BSRs). While diminishing returns are expected as a single component approaches ideal suppression of out-of-

band radiation, simultaneous use of selective components is practically advantageous, as selective cells may suppress radiative transfer in wavelength ranges poorly managed by the selective emitter, and vice versa. These approaches are explored in detail in *Chapter 2*.

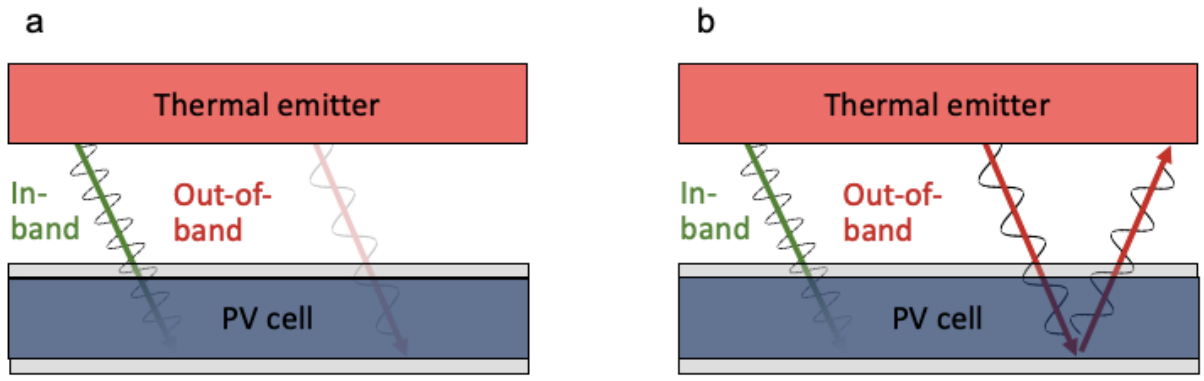

Figure 1.4. Selective radiative transport in a TPV system. (a) Emissive spectral control. Selective emitter materials are engineered to selectively emit in-band radiation while suppressing out-of-band emission. (b) Absorptive spectral control. Cells utilize a back surface reflector (BSR) or front surface filter (FSF) to reflect out-of-band radiation back to the thermal emitter. This photon recuperation process serves to reduce the net radiative power loss from the emitter, even if it exhibits broadband emission otherwise.

(ii) Internal Quantum Efficiency

Internal quantum efficiency *IQE* is a spectrally dependent measurement of photoexcitation and charge carrier collection. *IQE* may be expressed quantitatively as the ratio of charge carriers collected to the number of photons *absorbed* by the cell.

Poor *IQE* may indicate the presence of parasitic loss channels for above-bandgap photons. Specifically, absorption of convertible photons in metallic or heavily doped layers, such as BSRs and contacts, can lower *IQE*. Additionally, *IQE* losses can be indicative of a low-quality absorber

material or unoptimized geometry in which the charge carrier diffusion length is shorter than the cell's characteristic collection path.

1.3.2 Charge carrier management

Once charges are photogenerated, cells must efficiently collect those charges while maximizing output voltage The voltage factor *VF* and the fill factor *FF* jointly quantify the quality of charge carrier management in a cell.

(i) Voltage factor

Effective utilization of the bandgap is an important measure of cell performance. The ratio of open-circuit voltage V_{oc} to the bandgap voltage V_g is defined as the voltage factor *VF*:

$$VF = \frac{V_{oc}}{V_g} = \frac{q \cdot V_{oc}}{E_g} \tag{1.8}$$

where q is the elementary charge of an electron. Carrier recombination events represent the primary voltage loss pathway, so *VF* may serve as a measure of cell quality. Low quality materials (i.e., those with high defect densities) are susceptible to high rates of non-radiative recombination, resulting in decreased V_{oc}. Further, narrow bandgap cells exhibit lower *VF* since a larger fraction of the room-temperature emission spectrum lies above the bandgap, resulting in increased radiative recombination.

(ii) Bulk recombination pathways

Absorption of above-bandgap radiation in a photoactive semiconductor drives excitation of a valence electron to the conduction band, resulting in the formation of an electron-hole pair. Electron-hole pairs can either be separated and extracted as electrical current or recombine,

dissipating energy into the material. Electron-hole pair recombination can occur non-radiatively, which results in the dissipation of energy as heat. Radiative recombination results in the emission of a photon. Figure 1.5 depicts each of these recombination mechanisms.

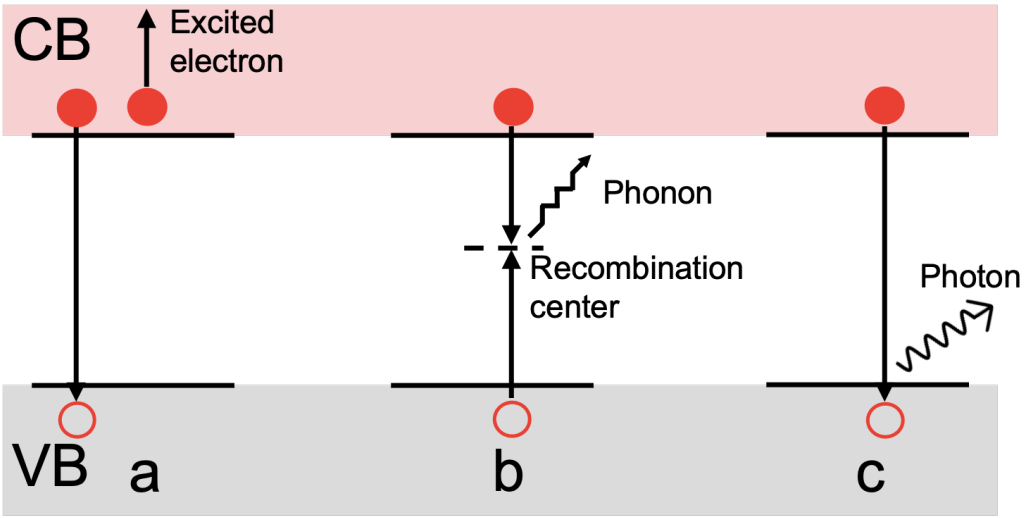

Figure 1.5. Bulk recombination pathways. (a) Auger recombination. (b) Shockley-Reed-Hall recombination. (c) Radiative recombination. The shaded gray region depicts the valence band (VB). The shaded red region depicts the conduction band (CB).

Auger recombination describes interband electron-hole recombination events, during which energy is transferred to a third charge carrier (electron or hole) not involved in the transition (Figure 1.5a). The rate of Auger recombination is highly dependent on the injected charge carrier population. Accordingly, Auger recombination typically dominates in highly doped regions and at high voltages.

Shockley-Reed-Hall (SRH) recombination describes intraband relaxation of an electron from a forbidden energy state (between bands) to the valence band, during which energy is dissipated as a phonon (Figure 1.5b). Forbidden energy states are typically occupied when a charge carrier

becomes trapped at a recombination center, such as a crystal defect. SRH recombination is prominent at exposed surfaces of the crystal where abrupt lattice interruption results in high concentrations of threading dislocations and unpaired valence electrons. SRH recombination at crystal surfaces (surface recombination) is particularly problematic in thin-film devices, which exhibit higher aspect ratio than conventional devices. SRH recombination usually dominates at low voltages and is augmented in low-quality crystals.

Radiative emission describes interband electron-hole recombination events, during which energy is emitted as a photon (Figure 1.5c). Photons emitted by radiative recombination have energy similar to the bandgap and can therefore generate additional electron hole pairs or escape the front surface of the semiconductor.

(iii) Fill factor

The maximum power point (MPP) describes the operating condition that results in peak power generation from a PV cell. Peak power generation occurs at forward bias V_{MPP} and current density J_{MPP}. The maximum power itself, P_{MPP}, is then the product of V_{MPP} and J_{MPP}. Fill factor (FF) is defined as the ratio of P_{out} to the product of V_{oc} and the short-circuit current density, J_{sc}:

$$FF = \frac{P_{out}}{V_{oc} \cdot J_{sc}} = \frac{J_{MPP} \cdot V_{MPP}}{J_{sc} \cdot V_{oc}} \tag{1.9}$$

Fill factor is primarily affected by the cell's series and shunt resistances, R_s and R_{sh}, respectively.

(iv) Series resistance

In the presence of series resistance, a portion of the generated power is dissipated as heat along the current's path. Contributions to R_s include bulk resistance along the longitudinal depth of the cell,

sheet resistance along the lateral direction, interfacial resistance at the contacts, and line losses along the length of the contact fingers and busbar. Proper design of highly conductive, selective contacts at the edges of the cell and optimized design of the contact grid geometry can help to minimize resistive losses. However, care should be taken in selecting the appropriate objective function when optimizing the grid design for TPV cells. In solar PV, an opaque top contact grid will shade the active layer and decrease output power, directly affecting the efficiency. For TPV cells, however, a reflective top grid could have a substantially smaller effect on conversion efficiency, as photons reflected by the grid can be reabsorbed by the emitter or active regions of the cell.

(v) Shunt resistance

Low shunt resistance can sharply affect a cell's fill factor in the case of low illumination conditions. However, shunting effects are not as important for most TPV cells because of their characteristically high current densities. Nevertheless, fabrication defects and film irregularities, such as pinholes or cracks, can provide a lower resistance path for current flow that bypasses the cell junction, thereby reducing the operating voltage.

1.3.3 Cavity effects

Cavity efficiency, $CE = Q_{abs} / Q_h$, describes the effectiveness of emitter-cell integration and is penalized by imperfect view factor, non-current-generating (i.e., inactive) areas on the cell, such as contact lines, and convective loss from the emitter. It is valuable for identifying problematic scaleup effects, such as parasitic thermal losses, compromises made in component integration, or difficulties fabricating large-area materials while maintaining peak performance. In this thesis, *CE*

is assumed to be 1 unless otherwise stated, such that net power from the emitter $Q_h = Q_{abs}$ (radiative power absorbed by the cell) and $\eta_{TPV} = P_{out}/Q_{abs}$.

1.4 Key computational methods

Here I detail the key computational methods used in this thesis for describing TPV performance metrics. Simulation of conversion efficiency requires separate modeling of the TPV cell's optical and electronic properties.

1.4.1 Transfer matrix optical simulation

Whereas the spectral properties (i.e., reflectance and/or transmittance) of a single interface may be described using the Fresnel equations, describing these properties becomes more complex for multi-layered samples, in which light is partially reflected and partially transmitted at each of multiple material interfaces. Reflections from each interface interfere destructively or constructively depending on phase shift and the resulting overall reflectance is the sum of an infinite number of reflections. The transfer matrix method, in contrast to field-tracing, is a less cumbersome technique for describing spectral properties.[15] This technique leverages continuity conditions at material boundaries to relate the electric field E and magnetic field H between two different points in a medium, see Figure 1.6.

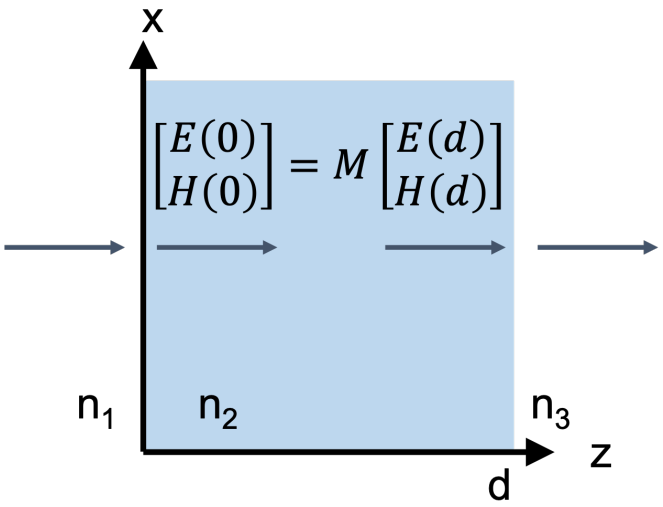

Figure 1.6. Transfer matrix method for optical modeling. The schematic depicts a light beam incident on a multi-layered structure. In this framework, all waves in a single medium (forward and backward) are combined into one wave. n_l denotes the refractive index of the lth layer.

The interference matrix M represents propagation through a layer and relates the electric and magnetic field at the layer's interfaces. In the case of a TM wave, it is given by:

$$M = \begin{bmatrix} \cos(\varphi_2) & ip_2 \sin(\varphi_2) \\ -\frac{1}{p_2}\sin(\varphi_2) & \cos(\varphi_2) \end{bmatrix} \tag{1.10}$$

where $\varphi_2 = \frac{\omega n_2 d cos(\theta_2)}{c}$ and $p_2 = \frac{\cos(\theta_2)}{\frac{n_2}{\mu c}}$. Here, ω is the angular frequency, c is the speed of light, and μ is the magnetic permeability. The flexibility of the transfer matrix method is realized in its extension to thin-film samples with many layers. The total interference matrix of a multilayer structure is given by:

$$M = M_1 M_2 M_3 \ldots M_N = \begin{bmatrix} m_{11} & m_{12} \\ m_{21} & m_{22} \end{bmatrix} \tag{1.11}$$

where N is the number of layers in the structure. Reflection and transmission coefficients are calculated from interference matrix constituents m_{ij}. Full derivation of reflectance and transmission terms for TM and TE waves are provided in reference [15].

In this thesis, I utilize a modified transfer matrix optical modeling technique based on the work of Deng, *et al.*,[16] which can spatially resolve the electric field distribution as a function of depth in an optical sample. This approach enables calculation of absorptance, decoupled by layer in stratified media. This approach decouples the interference matrix *M* into constituent matrices, the propagation matrix P_l, which describes free propagation through a material, and the dynamic matric $D_{l,l+1}$, which describes transfer at the boundary of two materials. These constituent matrices are described in Equations 1.12 and 1.13.

$$P_l = \begin{bmatrix} \exp(-ik_{l,z}d_l) & 0 \\ 0 & \exp(ik_{l,z}d_l) \end{bmatrix} \tag{1.12}$$

$$D_{l,l+1} = \frac{1}{2}\begin{bmatrix} 1+\frac{k_{l+1,z}\varepsilon_{l,z}}{k_{l,z}\varepsilon_{l+1,z}} & 1-\frac{k_{l+1,z}\varepsilon_{l,z}}{k_{l,z}\varepsilon_{l+1,z}} \\ 1=\frac{k_{l+1,z}\varepsilon_{l,z}}{k_{l,z}\varepsilon_{l+1,z}} & 1+\frac{k_{l+1,z}\varepsilon_{l,z}}{k_{l,z}\varepsilon_{l+1,z}} \end{bmatrix} \tag{1.13}$$

Here, $k_{l,z} = \sqrt{\left(\frac{\omega}{c}\right)^2 \varepsilon_l - k_x^2}$ is the *z*-component of the wave vector in the *l*th layer, ε_l is the dielectric constant of the *l*th layer, and k_x is the transverse component of the wave vector.

The standard interference matrix may be recovered from the propagation and dynamic matrices for the full structure according to:

$$M = P_1 D_{1,2} \dots P_{N-1} D_{N-1,N} P_N D_{N,substrate} = \begin{bmatrix} m_{11} & m_{12} \\ m_{21} & m_{22} \end{bmatrix} \tag{1.14}$$

The transfer matrix *T* between the *l*th layer and the sample substrate is then given by

$$T_l = P_l D_{l,l+1} \dots P_{N-1} D_{N-1,N} P_N D_{N,substrate} = \begin{bmatrix} t_{11} & t_{12} \\ t_{21} & t_{22} \end{bmatrix} \tag{1.15}$$

The value of this modified method comes from decoupling the interference matrix; in this framework, layer-specific absorptance may be calculated from matrix constituents m_{ij} and t_{ij}. Full

derivation of this term is provided in reference [16]. An example of layer-selective absorptance modeling is shown in Chapter 3, section 3.3.

1.4.2 Electronic simulation by fitting to experimental dark *J-V* properties

To provide a tool for device modeling and projecting cell performance, the experimental dark *J-V* properties of a PV cell are fit to a double-diode model, which describes the various bulk recombination pathways in the junction.

$$J = J_{diff} + J_{SRH} + J_{sh} + J_{tun} \tag{1.16}$$

Here, $J_{diff} = J_0 \times \left(exp\left(\frac{qV}{k_B T_c}\right) - 1\right)$ is the diffusion current. J_0 is the diffusion saturation current that can be extrapolated from the forward linear region of a log(*J*)-*V* curve in the dark. $J_{SRH} = J_{GR} \times \left(exp\left(\frac{qV}{2k_B T_c}\right) - 1\right)$ is Shockley Read Hall (*SRH*) generation and recombination current. Here, q is the charge of an electron and T_c is the temperature of the cell. In reverse bias, $J_{SRH} \approx J_{GR} = \frac{qn_i W}{\tau_{SRH}}$, where, n_i is intrinsic doping concentration of the active material, W is the depletion width, and τ_{SRH} is the *SRH* lifetime. J_{GR} can be fit from the forward log(*J*)-*V* curve in the dark. $J_{sh} = V/R_{sh}$ is the current for device with shunt resistance R_{sh}, and J_{tun} is reverse tunneling current arising from the small bandgap[17] and trap levels[18] of the active materials. At large current, series resistance (R_s) is also important. Thus, V is substituted by $(V - J \times R_s)$ in the above equations.

Under illumination, the *J-V* characteristic is: $J = J_{diff} + J_{SRH} + J_{sh} + J_{tun} - J_{ph}$, where J_{ph} is the photocurrent density. This term is calculated from the cell's simulated or experimental absorptance and the emissive properties of the emitter as:

$$J_{ph} = q \cdot F \cdot \int_{E_g}^{\infty} \varepsilon_{eff}(E)/\varepsilon_c(E) \cdot EQE(E) \cdot b(E, T_h)\, dE \tag{1.17}$$

where F is the view factor between emitter and cell, ε_c is the effective emissivity of the cavity, and ε_c is the emissivity of the cell. An example of dark *J-V* fitting is shown in Chapter 4, section 4.6.

These optical and electronic modeling techniques allow for prediction of the power generation P_{out} and absorbed radiative power Q_{abs}. Taken together, efficiency may be predicted as the ratio of the two terms.

1.5 Thesis overview

The fundamental challenge of engineering high-performance thermophotovoltaic systems involves the nature of the radiative transfer between the emitter and cell. Given the range of typical emitter temperatures (1000 – 2000K) and cell bandgaps (0.5 – 1.1eV), the majority of emitted power exists out-of-band and is therefore unusable by the cell. Figure 1.7 shows that conversion efficiency is highly sensitive to suppression of out-of-band radiative loss, particularly as out-of-band power approaches zero. As spectral control techniques have previously been limited to 95% suppression of out-of-band loss, significant efficiency gains may be achieved through improved spectral management, alone.

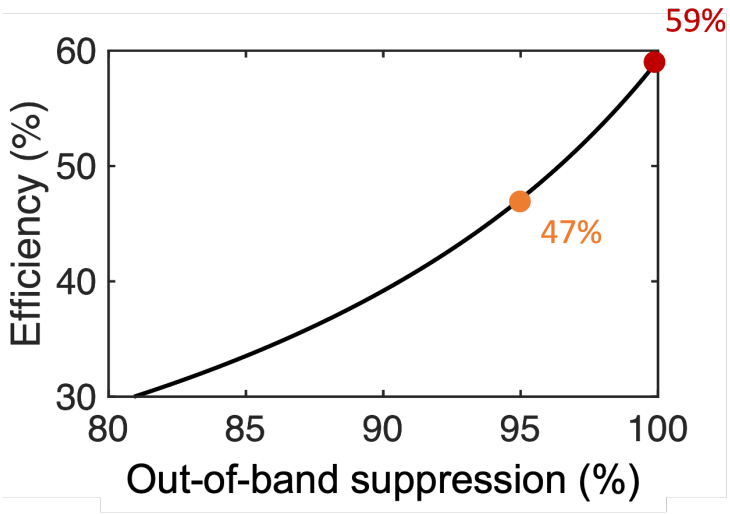

Figure 1.7. Radiative limit efficiency calculations for an InGaAs cell (E_g = 0.74eV) and a 1500K blackbody emitter as a function of out-of-band suppression. Efficiency is limited to 47% for R_{out} = 95%. This value increases to 59% for complete reflectance of out-of-band power (i.e., R_{out} = 100%). Details of the radiative limit calculation are provided in *Chapter 2*.

Given this opportunity for improved performance, the goal of this thesis is to eliminate out-of-band loss in thermophotovoltaic systems. Specifically, I seek to engineer photovoltaic cells with little to no out-of-band absorptance, such that unusable power from the emitter may be recuperated to the fullest extent. I have selected cold-side (i.e., absorptive) spectral control as my target approach for achieving this goal after identifying several opportunities for mitigating out-of-band absorptance in thin-film cells. This approach has the added benefit of relaxing the strict selectivity and stability requirements otherwise placed on the emitter component. The benefits and drawbacks of the selective cell approach are discussed in detail in *Chapter 2.*

I have identified InGaAs, lattice matched to InP (i.e., $In_{0.53}Ga_{0.47}As$), as my target photovoltaic material for this research effort. This alloy composition benefits practically from the commercial availability of high-quality InP substrates for epitaxial growth of the desired films. The material also exhibits optoelectronic properties that make it well-suited for use in thermophotovoltaic

systems, including a direct bandgap of 0.74eV and a strong in-band absorption coefficient. Together, these properties have established $In_{0.53}Ga_{0.47}As$ as a leading photovoltaic material for TPV systems throughout the literature and make it an excellent candidate for the development of low out-of-band loss thin-film cells. Other candidate materials are discussed in *Chapter 2*.

1.6 Thesis outline

This thesis begins with *Chapter 1*, an introduction to the concept of thermophotovoltaic energy conversion. Conversion efficiency was established as the primary performance metric to be used throughout this thesis to benchmark prior works in the literature and contextualize the presented advances. This metric was further decoupled into five separate performance metrics, each of which capture unique loss pathways in the TPV sub-system.

Chapter 2 provides a review of the thermophotovoltaic literature through June of 2020. In this work, I develop a framework based on the detailed balance limit of TPV conversion efficiency and utilize it to contextualize and compare a wide range of experimental works based on various component materials and characterization conditions. Analysis of the literature through this framework allows for the identification of leading approaches and opportunities for future improvements as they pertain to the performance metrics outlined in *Chapter 1*. Overall, this chapter reveals that the largest losses relative to theoretical limits are due to spectral inefficiencies.

Chapter 3 describes the design and optimization of thin-film cell architectures for improving the spectral characteristics of thermophotovoltaic cells. Candidate architectures are realized experimentally through molecular beam epitaxial growth techniques and non-destructive epitaxial

lift off. Optical characterization and simulation techniques reveal that dielectric claddings may be utilized to tailor in-band absorptance and out-of-band reflectance for improved spectral efficiency. Thin-film architectures are shown to offer a pathway to drastic performance improvements over conventional, substrate-containing architectures.

In *Chapter 4*, I detail the design and characterization of a TPV cell with a novel air-bridge architecture, in which the thin-film absorber is suspended over a buried air cavity. This unique structure is shown to drastically reduce out-of-band radiative loss, enabling a 4x reduction to out-of-band loss compared to prior cells with conventional metallic reflectors. This result enables record-high conversion efficiency. Beyond improving absolute efficiency, the spectral improvements enabled by this architecture are shown to reduce the dependence of conversion efficiency on component characteristics, such as cell bandgap and emitter temperature.

Chapter 5 details an entirely new approach to spectral management: use of a partially transparent cell with rear view of a secondary emitter. In this section, I present a proof-of-principle transparent cell and describe how the concept can enable operation of thermophotovoltaics in an entirely new regime. By enabling out-of-band spectral losses below 1%, the transparent concept may fully eliminate the negative dependence of conversion efficiency on increased cell bandgap and decreased emitter temperature. This advance could ultimately enable use of thermophotovoltaic generators in application spaces not previously thought possible.

Lastly, in *Chapter 6*, I summarize the key results presented in this thesis and consider the broader outlook for the field of thermophotovoltaics. I assess some of the challenges facing the field,

including the lack of standardized characterization protocols and the high modular cost of III-V cells. Finally, I describe a couple exciting future directions for TPV cell research, namely the development of Si and tandem TPV cells.

1.7 References

1. Amy, C., Seyf, H.R., Steiner, M.A., Friedman, D.J., and Henry, A. (2019). Thermal energy grid storage using multi-junction photovoltaics. Energy Environ. Sci. *12*, 334–343.
2. Datas, A., Ramos, A., Martí, A., del Cañizo, C., and Luque, A. (2016). Ultra high temperature latent heat energy storage and thermophotovoltaic energy conversion. Energy *107*, 542–549.
3. Seyf, H.R., and Henry, A. (2016). Thermophotovoltaics: a potential pathway to high efficiency concentrated solar power. Energy Environ. Sci. *9*, 2654–2665.
4. Fraas, L.M., Avery, J.E., and Huang, H.X. (2003). Thermophotovoltaic furnace–generator for the home using low bandgap GaSb cells. Semicond. Sci. Technol. *18*, S247–S253.
5. Durisch, W., and Bitnar, B. (2010). Novel thin film thermophotovoltaic system. Sol. Energy Mater. Sol. Cells *94*, 960–965.
6. Bianchi, M., Ferrari, C., Melino, F., and Peretto, A. (2012). Feasibility study of a Thermo-Photo-Voltaic system for CHP application in residential buildings. Appl. Energy *97*, 704–713.
7. Horowitz, K.A., Remo, T.W., Smith, B., and Ptak, A.J. (2018). A Techno-Economic Analysis and Cost Reduction Roadmap for III-V Solar Cells.
8. Wang, C.A. (2004). Antimony Based III-V Thermophotovoltaic Devices. Thermophotovoltaic Gener. Electr. Sixth Conf., 1–29.
9. Omair, Z., Scranton, G., Pazos-Outón, L.M., Xiao, T.P., Steiner, M.A., Ganapati, V., Peterson, P.F., Holzrichter, J., Atwater, H., and Yablonovitch, E. (2019). Ultraefficient thermophotovoltaic power conversion by band-edge spectral filtering. Proc. Natl. Acad. Sci. *116*, 15356–15361.
10. Burger, T., Fan, D., Lee, K., Forrest, S.R., and Lenert, A. (2018). Thin-Film Architectures with High Spectral Selectivity for Thermophotovoltaic Cells. ACS Photonics *5*, 2748–2754.
11. Lee, K., Zimmerman, J.D., Hughes, T.W., and Forrest, S.R. (2014). Non-Destructive Wafer Recycling for Low-Cost Thin-Film Flexible Optoelectronics. Adv. Funct. Mater. *24*, 4284–4291.
12. Lee, K., Shiu, K.T., Zimmerman, J.D., Renshaw, C.K., and Forrest, S.R. (2010). Multiple growths of epitaxial lift-off solar cells from a single InP substrate. Appl. Phys. Lett. *97*, 10–12.
13. Bauer, T. (2011). Thermophotovoltaics: basic principles and critical aspects of system design (Springer Berlin Heidelberg).
14. Mauk, M.G. (2006). Survey of Thermophotovoltaic (TPV) Devices. In Mid-infrared Semiconductor Optoelectronics (Springer London), pp. 673–738.
15. Cheng, G. Energy transfer by waves. Nanoscale Energy Transp. Convers. A Parallel Treat. Electrons, Mol. Phonons, Photons.
16. Deng, X.-H., Liu, J.-T., Yuan, J.-R., Liao, Q.-H., and Liu, N.-H. (2015). A new transfer matrix method to calculate the optical absorption of graphene at any position in stratified media. Europhys. Lett. *109*, 27002.
17. Forrest, S.R., Leheny, R.F., Nahory, R.E., and Pollack, M.A. (1980). $In_{0.53}Ga_{0.47}As$ photodiodes with dark current limited by generation-recombination and tunneling. Appl. Phys. Lett. *37*, 322–325.
18. Riben, A.R., and Feucht, D.L. (1966). Electrical Transport in nGe-pGaAs Heterojunctions†. Int. J. Electron. *20*, 583–599.

Chapter 2: Present Efficiencies and Future Opportunities in Thermophotovoltaics

2.1 Motivation

To accelerate the development of TPVs and realize efficiencies closer to theoretical limits, it is important to identify which aspects of current designs are favorable and where significant technological gaps remain. However, meaningfully comparing experimental TPV literature is challenging because of the variability in emitter and cell temperature and cavity geometry. Consequently, comparison of metrics such as short-circuit current density (J_{sc}) and open-circuit voltage (V_{oc}) alone, which is meaningful in the solar PV literature,[1] is poorly suited for evaluation of TPV performance.

To overcome this barrier, this chapter presents a review of current approaches and identifies major opportunities for future research by comparing leading TPVs across material systems to thermodynamic limits. I would like to acknowledge here the contributions of my co-author, Caroline Sempere, in helping to prepare this review. Caroline led raw data collection efforts and assisted with data analysis for identification of trends in the literature.

In this review, I account for variable testing conditions by comparing major energy conversion steps to their respective fundamental limit, calculated using experiment-specific parameters such as bandgap (E_g), emitter temperature (T_h), and cell temperature (T_c). This limit is defined by the detailed-balance model that considers radiative recombination as the lone carrier loss mechanism (i.e., the radiative limit).[2–4] By accounting for these effects, I can make systematic comparisons across reported efficiencies and identify limitations in spectral and carrier management within leading TPV pairs. Although systematic reviews of the literature have been conducted, notably the work of Mauk,[5] Zhou, *et al.*,[6] Datas, *et al*.,[7] Ferrari, *et al.*,[8] Daneshvar, *et al.*,[9] and Sakakibara, *et al.*,[10] an analysis of how the performance metrics of leading TPVs compare to the radiative limit has not been reported. Lastly, this chapter considers the efficiency gap observed when scaling up and translating TPV emitter-cell pairs toward practical implementation.

This chapter is structured as follows. Section 2.2. outlines the detailed balance framework used to compare experimental TPV literature. Section 2.3 analyzes leading TPV emitter-cell pairs and identifies current limitations in spectral and carrier management based on the figures of merit described in *Chapter 1*. Sections 2.4 and 2.5 provide a review of leading and emerging component-wise approaches for improvement of spectral and carrier management, respectively. Section 2.6 discusses the efficiency gap observed between TPV emitter-cell pairs and more scaled-up systems, which are termed TPV sub-systems.

I note here that this review is primarily based on conversion efficiency as the figure of merit for evaluating state-of-the-art TPV technologies. While commercial application of TPV generators will ultimately rely on cost metrics, assessment of system costs can be challenging given the

technology's current readiness level. Conversion efficiency, which is directly related to cost-sensitive metrics,[11] is better suited for identifying promising component materials for continued development. Furthermore, while the total system efficiency of TPV generators captures upstream primary energy conversion and heat transfer losses, TPV-based energy systems are fundamentally limited by conversion of heat into thermal radiation, and radiation into electricity. Other factors directly impacting total system efficiency depend on the heat source (e.g., solar thermal efficiency, burner efficiency, adiabatic efficiency) and can be derived separately from the metrics used here. Although total system efficiencies of solar-,[12–15] chemical-,[16,17] and nuclear-sourced[18] TPV generators are relatively low (4-8%) compared to well-established energy systems such as natural gas combined-cycle power plants, TPVs are generally too technologically immature to be compared at that level. Substantial research efforts and resources are needed to develop TPV components at the necessary scale for prototypical generators to approach the potential efficiencies set by the emitter and cell materials. These challenges should not impede progress in the development of high-performance cell and emitters. This review therefore emphasizes the performance of emitter-cell pairs and TPV sub-systems, as defined in the following sections.

This review considers TPV sub-system efficiency $\eta_{TPV} = P_{out}/Q_h$ and TPV pairwise efficiency $\eta_{pairwise} = P_{out}/Q_{abs}$ as the figures of merit for evaluating state-of-the-art TPV technologies, where P_{out} is the generated electrical power, Q_h is the heat flow out of the emitter surface, and Q_{abs} is the heat absorbed by the cell. These metrics are appropriate for analysis of various TPV emitter-cell pairs and devices. If a study reports additional upstream losses,[14,15,19] those were decoupled to allow for direct comparison across TPV literature. Note that $\eta_{pairwise}$ is equivalent to η_{TPV} in the case of an ideal, lossless cavity ($Q_{abs} = Q_h$). $\eta_{pairwise}$ has also been termed

"radiative heat conversion efficiency" elsewhere.[20] This review utilizes $\eta_{pairwise}$ to identify promising emitter and cell materials/pairs for further scale up and development because it decouples loss mechanisms inherent to materials from inefficiencies resulting from component integration.

2.2 Detailed balance limit framework

Here, I evaluate performance metrics with respect to their upper bounds, as described in the radiative limit. The radiative limit is not only a function of bandgap, but also depends on the temperatures of the emitter and cell. Hence, a singular limit that applies to all cells with a given bandgap (as is common in solar PV literature) cannot be provided. Rather, I provide radiative limit metrics, denoted by "rad" subscripts, specific to select emitter-cell pairs, as calculated from reported E_g, T_h, and T_c using the analytic expressions in Table 2.1. The upper bound of η_{TPV} is then the product of each performance metric in the radiative limit. Normalized values are calculated as the ratio of experimentally observed values to corresponding limits.

Table 2.1. Definitions and limits of TPV performance metrics.

	Definition	Radiative limit
$SE \cdot IQE$[a,b]	$\frac{J_{sc}V_g}{Q_{abs}} = \frac{E_g \cdot \int_{E_g}^{\infty} \varepsilon_{eff}(E) \cdot IQE \cdot b(E,T_h)\, dE}{\int_0^{\infty} \varepsilon_{eff}(E) \cdot E \cdot b(E,T_h)\, dE}$	$\frac{E_g \cdot \int_{E_g}^{\infty} b(E,T_h)\, dE}{\int_{E_g}^{\infty} E \cdot b(E,T_h)\, dE}$
VF[c]	$\frac{V_{oc}}{V_g}$	$\left(\frac{k_B T_c}{qV_g}\right) \cdot \ln\left(\frac{J_{sc}}{J_{0,rad}} + 1\right)$
FF	$\frac{J_{mpp} \cdot V_{mpp}}{J_{sc} \cdot V_{oc}}$	$\frac{\left(\frac{V_{mpp}}{V_{th}}\right)^2}{\left[1 + \frac{V_{mpp}}{V_{th}} - \exp\left(\frac{-V_{mpp}}{V_{th}}\right)\right] \cdot \left[\frac{V_{mpp}}{V_{th}} + \ln\left(1 + \frac{V_{mpp}}{V_{th}}\right)\right]}$
CE	$\frac{Q_{abs}}{Q_h}$	1
$\eta_{pairwise}$	$SE \cdot IQE \cdot VF \cdot FF$	$SE_{rad} \cdot IQE_{rad} \cdot VF_{rad} \cdot FF_{rad}$
η_{TPV}	$SE \cdot IQE \cdot VF \cdot FF \cdot CE$	$SE_{rad} \cdot IQE_{rad} \cdot VF_{rad} \cdot FF_{rad} \cdot CE_{rad}$

E is photon energy, q is the charge of an electron, $V_{th} = \frac{k_B T_c}{q}$ is the thermal voltage, and the "mpp" subscript denotes the maximum power point voltage (V) and current density (J).

[a]Effective emissivity of an emitter-cell pair: $\varepsilon_{eff} = \frac{\varepsilon_e \varepsilon_c}{\varepsilon_e + \varepsilon_c - \varepsilon_e \varepsilon_c}$, where ε_e and ε_c are the emissivity of the emitter and cell, respectively.

[b]Spectral photon flux of a black body: $b(E,T) = \frac{2\pi E^2}{c^2 h^3 \left(\exp\left(\frac{E}{k_B T}\right) - 1\right)}$, where c is the speed of light in vacuum, h is Planck's constant, and k_B is Boltzmann's constant.

[c]Dark current density: $J_0 = J_{sc}\left[\exp\left(\frac{qV_{oc}}{k_B T_c}\right) - 1\right]^{-1}$

In the radiative limit: $J_{0,rad} = \frac{2 \cdot q}{h^3 \cdot c^2} \pi (n^2 + 1) k_B T_c \left(2k_B^2 T_c^2 + k_B T_c E_g + E_g^2\right) \exp\left(\frac{-E_g}{k_B T_c}\right)$, where the real part of the refractive index n = 3.6 (0) corresponds to the radiative limit in the absence (presence) of photon recycling.[21]

2.3 Record-efficiency TPV pairs compared to the radiative limit

This section compares leading emitter-cell pairs to each other and to radiative limits in order to identify favorable features and technology gaps. My use of the term "leading" refers to a given emitter-cell pair exhibiting the highest $\eta_{pairwise}$ in a group of like pairs, as defined by their shared cell material. I have grouped pairs by cell material since the cell bandgap also corresponds to the desired emitter cutoff energy (E_{cutoff}).

2.3.1 Comparison of pairwise efficiencies

Figure 2.1 shows the best pairwise efficiencies as reported (Figure 2.1a) and normalized by corresponding radiative limit efficiencies (Figure 2.1b). I further depict a timeline of historical improvements to leading pairwise efficiencies in Figure 2.1c. Normalized, thermodynamic efficiencies are considered for further analysis because test conditions, particularly T_h, vary greatly across the TPV literature. Hence, comparison of absolute efficiencies provides limited insight into the quality of emitter-cell pair design.

The 2019 demonstration of a thin-film lattice-matched, 0.75 eV InGaAs cell (hereafter LM InGaAs) paired with a ~1480 K graphite emitter represents the highest reported absolute pairwise efficiency (29.1%) for any TPV pair in the literature.[22] This pair also achieves the highest fraction of its radiative limit efficiency (~49%). Similar absolute efficiency has been reported by Swanson (1980) for a Si cell paired with a 2300K blackbody emitter (29%).[23] However, when comparing efficiencies to the radiative limit, the Si-based pair falls short of the LM InGaAs-based pair (43.7% vs. 49%) due to the large difference in emitter temperature.

High pairwise conversion efficiencies, exceeding 20%, have also been reported for lattice-mismatched 0.6 eV InGaAs (hereafter 0.6 eV InGaAs) paired with a 1312K graybody SiC emitter[24] and with a 1328K selective emitter (2D Pt puck array on Al_2O_3/Pt stack).[25] Lastly, $\eta_{pairwise}$ above 20% has also been reported for a GaSb cell paired with a 1548K W emitter.[16] These demonstrations also represent some of the highest thermodynamic pairwise efficiencies.

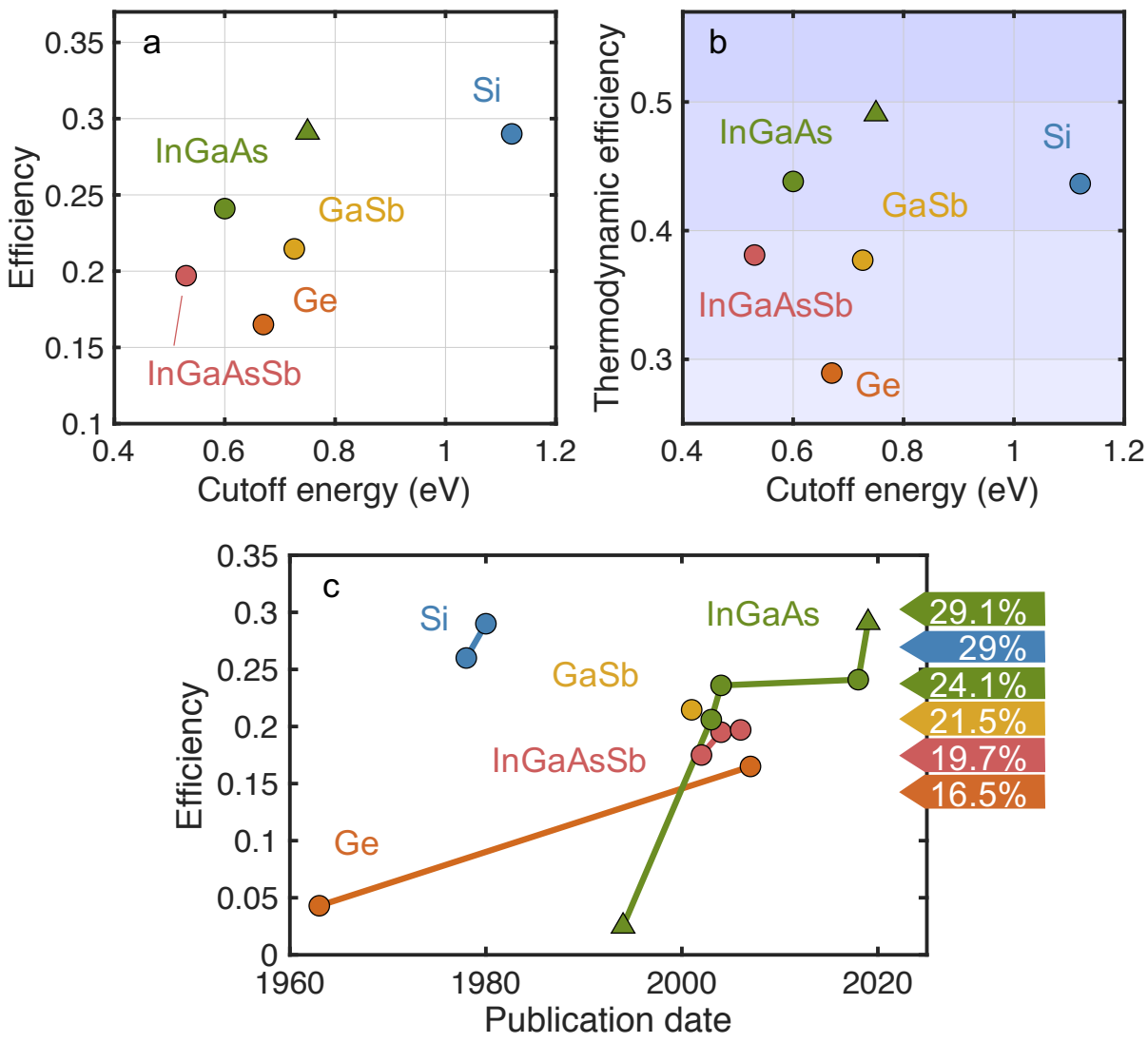

Figure 2.1. Record pairwise efficiencies spanning cell materials. (a) Absolute efficiencies as reported. (b) Thermodynamic efficiencies, normalized against the radiative limit. (c) Historical progression of record pairwise efficiencies. Reporting literature: InGaAsSb[26–28]; 0.6 eV InGaAs[24,25,29]; Ge[30,31]; GaSb[16]; LM InGaAs[22,32] (triangular markers); Si.[23,33]

Overall, leading pairwise efficiencies remain well below their respective radiative limits (< 50%). By contrast, leading solar PV cells have achieved efficiencies exceeding 75% of their corresponding radiative limit.[1,34–38] This analysis reveals that TPV technologies remain immature compared to solar PVs, but does not yet offer insights into the shortcomings of leading designs.

2.3.2 Comparison of constituent performance metrics

To provide a deeper understanding of current limitations, I collected experimental *VF* and *FF* data and calculated *SE*·*IQE* from reported metrics for leading emitter-cell pairs (Figure 2.2, Table 2.2). Figure 2.2a depicts emitter-cell pair performance relative to the radiative limit and compactly decouples contributions according to spectral and charge carrier management. The quality of spectral management is quantified as the ratio of the reported product of *SE* and *IQE* to the corresponding product in the radiative limit, depicted as the vertical axis in Figure 2.2a. Similarly, the horizontal axis depicts the corresponding ratio for *VF* and *FF*, representing the quality of charge carrier management.

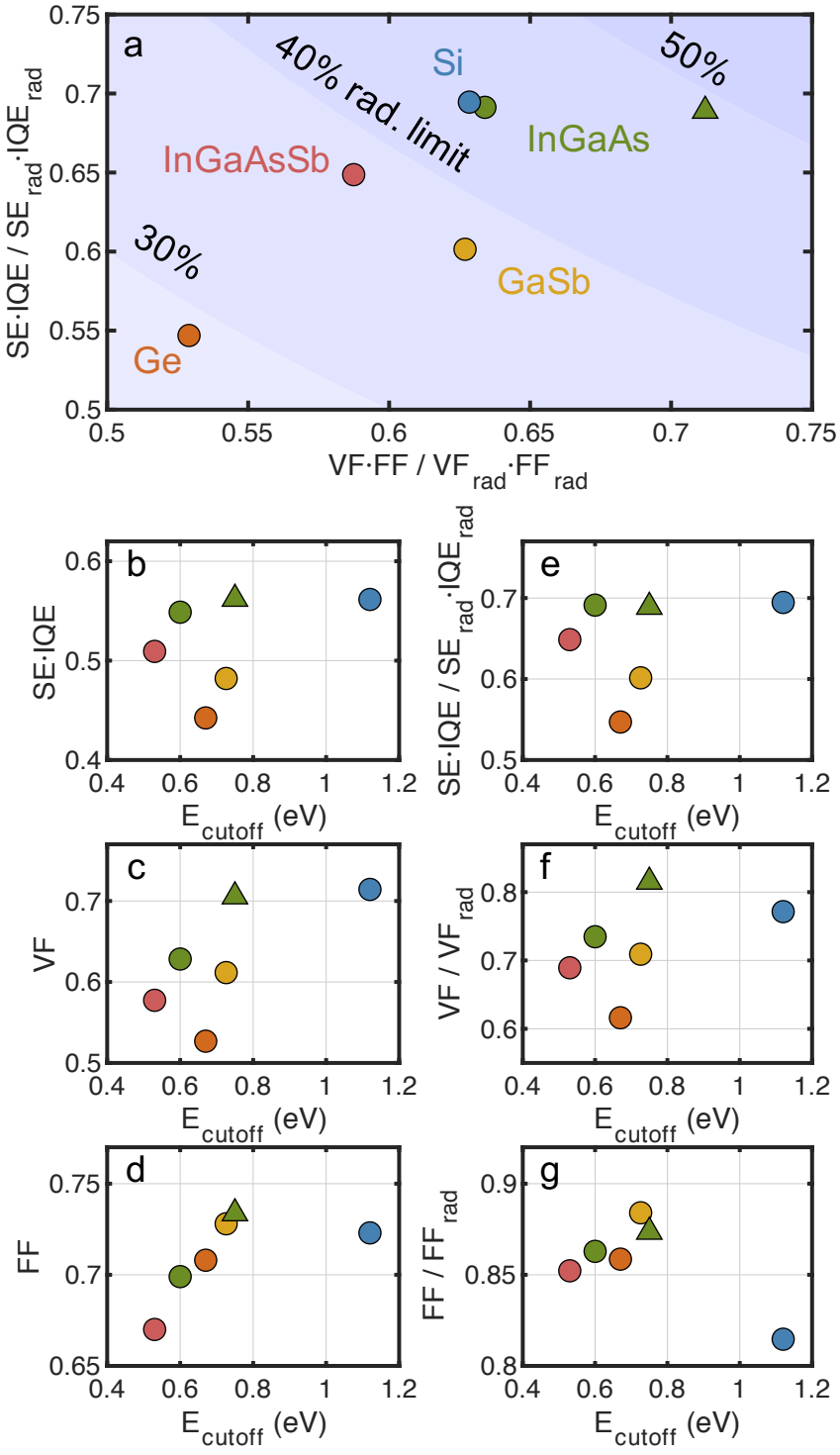

Figure 2.2. Characteristics and limitations of leading TPV pairs. (a) The product of *SE* and *IQE* describes the quality of spectral management. *VF* and *FF* characterize the effectiveness of charge carrier management. Normalization to corresponding values in the radiative limit provides a basis for identifying target metrics for improvement. (b-d) Reported, absolute performance metrics. (e-g) Performance metrics, normalized to corresponding values in the radiative limit. Reporting literature: InGaAsSb[26]; 0.6 eV InGaAs[25]; Ge[31]; GaSb[16]; LM InGaAs[22] (triangular markers); Si.[23]

The three highest efficiency TPV pairs (with LM InGaAs, Si, and 0.6 eV InGaAs cells) exhibit the best spectral management, approaching ~70% of the radiative limit for *SE·IQE*. This result is consistent with the widely recognized notion that management of the broad spectrum of thermal radiation is critical in TPVs. The cell used for the leading Si-based pair utilizes a SiO_2/Ag back surface reflector (BSR) to achieve ~95% out-of-band reflectance and facilitate the photon recuperation process. Similarly, the leading LM InGaAs-based pair utilizes a cell with a Au BSR. The high out-of-band reflectance (~94%) is enabled by the cell's thin-film architecture. Removal of the InP parent substrate eliminates a parasitic absorption mechanism previously observed for LM InGaAs cells.[32] In each case, the cell's high out-of-band reflectance promotes efficient spectral utilization, even under illumination by a broadband emitter. The leading 0.6 eV InGaAs-based pair, on the other hand, relies on a 2D metamaterial selective emitter and a dielectric front surface filter (FSF) to minimize undesired absorption in the cell. The narrower bandgap cell used in this pair is better suited for the emitter temperature, which serves to benefit *SE*. While this strategy appears to offer similar out-of-band suppression to those described above, I cannot make a direct quantitative comparison as cell reflectance properties are not provided. The quality of spectral management among these leading pairs highlights the importance of spectral efficiency (*SE*) in achieving high conversion efficiency. Further, I note the common use of out-of-band reflectance (by a BSR or FSF) as a technique to facilitate spectral management among these leading pairs.

In terms of carrier management, the leading LM InGaAs-based pair exhibits the best *VF·FF*, exceeding 70% of the corresponding radiative limit. This is largely attributed to the cell's high V_{oc}, which translates to the highest normalized *VF* among pairs considered here. While V_{oc} generally

increases with illumination intensity, this particular *VF* is not attributed to differences in illumination, as the leading LM InGaAs-based pair is characterized at J_{sc} = 0.92 A cm^{-2}, which is low relative to other leading pairs. Beyond this consideration, differences in cell growth and resulting material quality may affect the quality of charge carrier management. The leading LM InGaAs and 0.6 eV InGaAs cells were both grown by metal-organic vapor phase epitaxy (MOVPE) on an InP substrate. However, the leading LM InGaAs-based pair exhibits higher normalized *VF* (0.71) than that of the 0.6 eV InGaAs-based pair (0.63). Notably, it is more challenging to achieve low defect densities in a cell utilizing a buffer layer to overcome lattice mismatch, as is necessary for growth of 0.6 eV InGaAs epitaxial layers on InP.[39]

I also note that the bandgap/cutoff energy of leading pairs does not maximize *SE*, given their respective T_h and level of selectivity (see Figure 2.3a,d). In general, the bandgap exceeds the value that optimizes *SE*. For example, Woolf, *et al.* utilize a 0.6 eV InGaAs cell in tandem with an emitter at T_h = 1328K, whereas $E_g \approx$ 0.5eV would maximize *SE* at these operating conditions. While lower E_g is desirable for improving *SE*, detrimental side effects on carrier management were likely considered in the design of leading pairs. In particular, lower E_g increases the portion of in-band radiation, thereby increasing J_{sc}. At high $J_{sc,}$ Ohmic losses can reduce *FF*, which may outweigh the benefit to *SE*. Further, as bandgap narrows, thermal generation produces a larger intrinsic carrier concentration, n_i, increasing proportional loss to recombination and decreasing *VF*. Therefore, optimal *SE* may not correspond to maximized $\eta_{pairwise}$.

Table 2.2. Leading TPV emitter-cell pairs by cell material class.

Cell	E_g [eV]	T_c [K][a]	Emitter	T_h [K]	J_{sc} [A cm^{-2}]	V_{oc} [V]	$SE \cdot IQE$[b]	VF	FF	$\eta_{pairwise}$ [%]	$\eta_{pairwise,rad}$ [%]	Ref
InGaAsSb	0.53	300	SiC plate	1223	2.9	0.31	0.51	0.58	0.67	19.7	51.7	[26]
0.6 eV InGaAs	0.6	-	Pt array on Al_2O_3/Pt	1328	0.72	0.38	0.55	0.63	0.70	24.1	55.0	[25]
Ge	0.67	-	Micro-structured W	1373	1.65	0.35	0.44	0.53	0.71	16.5	57.0	[31]
GaSb[c]	0.73	323	W foil with ARC	1548	3.52	0.45	0.48	0.62	0.73	21.5	56.9	[16]
LM InGaAs	0.75	293	Graphite ($\varepsilon \approx 0.9$)	1480	0.92	0.53	0.56	0.71	0.73	29.1	59.3	[22]
Si	1.12	-	Presumed blackbody	2300	8.76	0.8	0.56	0.71	0.72	29.0	66.4	[23]

[a]In cases where T_c has been omitted in the relevant publication, T_c = 293K has been assumed for relevant calculations.
[b]$SE \cdot IQE$ is calculated from reported $\eta_{pairwise}$, VF, and FF.
[c]In the case of GaSb, only simulated VF and FF are reported.

2.4 Spectral management

This section decouples the effects of emitter and cell properties to survey emerging component-wise approaches for TPV spectral management. Prior reports have sought to describe emitter-specific spectral efficiency as the ratio of in-band power to total emitted power,[40] and therefore defined cell efficiency in terms of the conversion of in-band power. This formulation, however, neglects the cell's role in modifying the spectrum of Q_{abs}, and cannot be easily generalized to pairs with reflective cells. To provide a more complete description of component-wise contributions to spectral management, I investigate the properties of a single component by considering its spectral efficiency when paired with a theoretical blackbody (non-selective) counterpart. This metric is termed "individual *SE*".

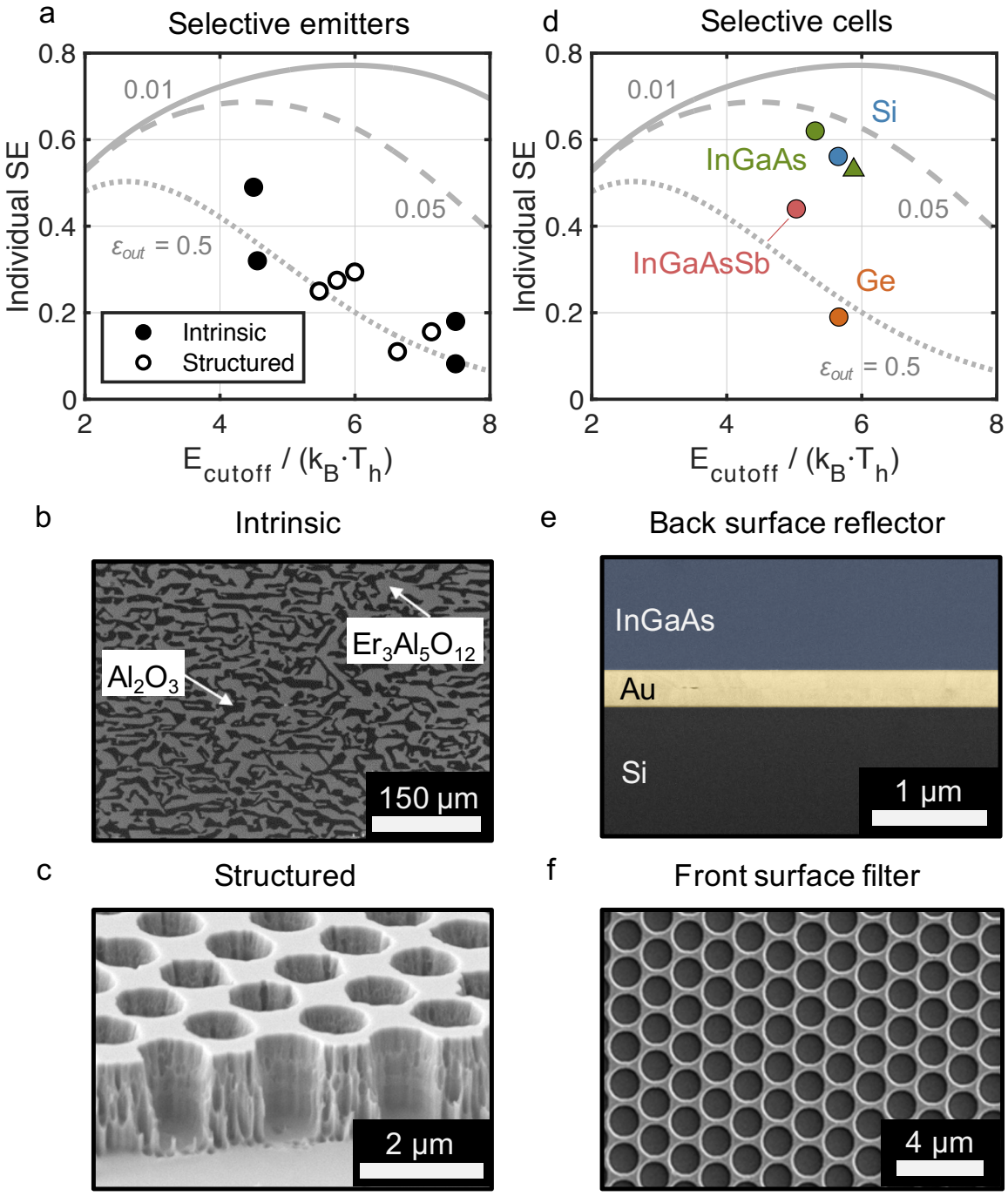

Figure 2.3. Component-wise spectral control strategies. Individual spectral efficiencies of (a) selective emitters and (d) selectively absorptive cells. Experimental values are compared to *SE* curves for various out-of-band emissivities with ideal in-band absorption (ε_{in} = 1). Examples of spectral control structures: (b) $Al_2O_3/Er_3Al_5O_{12}$ eutectic ceramic,[41] (c) 2D W cavity array,[42] (e) thin-film LM InGaAs with Au BSR,[43] (f) 2D photonic crystal front-surface filter on a GaSb cell.[44] Figure 2.3b reproduced with permission from Nakagawa, *et al.*, 2005.[41] Figure 2.3c reproduced with permission from Yeng, *et al.*, 2012.[42] Figure 2.3e reproduced with permission from Burger, *et al.*, 2018.[43] Figure 2.3f reproduced with permission from Shemelya, *et al.*, 2014. [44]

2.4.1 Selective Emitters

Selective thermal emitters are designed to preferentially emit in-band radiation, while simultaneously suppressing out-of-band emission.[10] Here, I narrow the scope of surveyed emitters to (i) those that have been heat treated at or above 1023 K (750°C) for over 1 hour and (ii) whose optical properties were characterized at or above 1023 K (750°C). The first criterion was selected because, beyond degraded spectral performance, if an emitter is unstable, material may evaporate and subsequently deposit onto the cell. Hence, long-term thermal stability is important for the reduction of operation and maintenance costs. While one hour of thermal aging does not sufficiently demonstrate the degree of stability required for practical application, this criterion is appropriate given the current technology readiness level of emerging emitters. In some cases, one hour of aging at temperatures in excess of 1000°C can reveal major instabilities.[45] The second criterion is required because emissivity is temperature dependent. Measurement of thermal emissivity near room temperature has been shown to significantly underestimate the actual thermal emissivity at high temperature.[46] I therefore calculate individual *SE* based on reported spectra measured at high temperatures (T_h in Table 2.2).

Figure 2.3a shows the individual *SE* of various emitters that meet the above criteria, compared to analytical curves for perfect, in-band absorption ($\varepsilon_{in} = 1$) and a range of out-of-band suppression. I show the theoretical curves in this way because decreasing out-of-band emission/absorption has a greater effect on *SE* than increasing in-band emission/absorption due to the relative power in each band. In this analysis, I have categorized the emitters according to two groups: (i) intrinsically selective materials such as transition metal and rare earth oxides (Figure 2.3b) and (ii) structurally

tunable thermal emitters exhibiting geometry-dependent spectral properties (Figure 2.3c). Tunable emitters typically leverage periodic architectures with one-dimensional (i.e., alternating stacks), two-dimensional (i.e., cavity or pillar arrays), or three-dimensional (i.e., inverse opal networks) periodicity at a length-scale on the order of the wavelength of interest.[47] Individual *SE* calculations generally follow theoretical curves for the corresponding ε_{out}; deviation from these curves is the result of non-ideal in-band absorption ($\varepsilon_{in} < 1$).

In terms of the best spectral efficiency exhibited among intrinsically selective materials, a MgO emitter with NiO loading[48] achieves a notable 49% spectral efficiency. Introducing transition-metal dopant ions within a low emissivity MgO host lattice leads to selective emission due intra-atomic electronic transitions. These transitions are determined by the electronic configuration of the dopant ions and interactions with the lattice of the host oxide. Dopant concentrations of 1–2 mol% appear to be optimal because of a tradeoff between nearest neighbor interactions and peak spectral density. This survey also shows that intrinsic emitters generally exhibit better thermal stability. Despite these noteworthy results, relatively few papers have explored the use of transition-metal dopants in TPV emitters. As such, their ability to tailor emission properties to match the bandgap of a cell remains limited.

Alternatively, structured emitters offer improved control over the emission cutoff energy. The leading structured thermal emitter is a W 2D photonic crystal emitter with a cavity array geometry that exhibits 29.4% individual *SE*.[42] Enhanced in-band emission occurs by coupling into resonant electromagnetic cavity modes, while emission is suppressed below the cavity resonant frequency. The resonant frequency, and therefore cutoff energy, of the emitter may be tuned by varying cavity

diameter and depth. Further, the sharpness of the transition is a result of geometrical uniformity. Another high-performance structured emitter with individual *SE* = 27.5% utilizes a similar structure, consisting of a Ta-W alloy with a HfO_2 coating.[49] The considerable difference in individual *SE* between the best intrinsic and leading structured emitters is largely due to the lower demonstrated temperatures of structured emitters.

Other structured emitters, characterized near room temperature, exhibit promising spectral properties. For example, a HfO_2/Mo/HfO_2 emitter leverages its ultrathin Mo absorber layer (much thinner than the wavelength) and a Fabry-Perot cavity created between the top interface and the bottom reflector to achieve coherent perfect absorption at a wavelength near the cell's bandgap.[50] Similar structures, where a refractory metal such as W is sandwiched between dielectrics, have also exhibited comparable spectral efficiencies based on room temperature emissivity measurements.[51,52] However, it is unclear if these promising properties will translate to high performance at operating temperatures. Future studies should thus strive to report data at high temperatures.

The primary failure mechanisms of structured emitters appear to be oxidation of the metal layers and growth of dielectric grains, both of which are activated by high temperatures.[51] However, the kinetics of these mechanisms can be slowed by operating under moderate vacuum and below the grain growth temperature threshold.

One promising way to stabilize emitters appears to be the use of transparent refractory coatings. Nearly all tunable, selective emitters that meet the heat treatment criteria integrate a refractory

metal / metal oxide component. Low-defect refractory coatings enhance thermal stability by impeding surface reactions and inhibiting diffusion.[49,53] Prior studies have identified HfO_2 as a leading candidate among refractory materials for improved stability.[54,55] Integration of refractory materials may help to improve the thermal stability of emitters designed solely for high selectivity at room temperature. While tunable, selective emitters may rely on nano- and micro-patterned designs to achieve selectivity, the resulting void space in 2D and 3D geometries leave materials susceptible to thermal degradation. One proposed strategy for improved stability in 2D and 3D structured emitters is to fill void space with an additional material, thereby achieving bulk planar geometry while maintaining the necessary patterning for selectivity.[56] Decreased structural curvature through modified periodicity and smoother geometrical transitions has also been shown to alleviate thermal degradation of cavities.[57]

A widely proposed plan to protect the cell from material deposition under an unstable emitter is the use of an intermediate glass cover or a gas purge.[58] However, out-of-band absorption in a deposition shield may limit the effectiveness of cell-side spectral control, such that the pair relies on the emitter's optical properties for achieving high *SE*. Furthermore, operation at elevated radiative power densities may be required to decrease the relative effect of convective losses associated with a gas purge/curtain.

Overall, it appears that significant improvements in spectral efficiencies are possible through additional materials development. Furthermore, high-temperature aging data for selective emitters is lacking. Longer thermal aging studies are necessary to identify failure mechanisms and suitable operating conditions.

Table 2.3. Selective thermal emitters, heat treated above 1023K for at least 1 hour and with emissivity measured at temperatures >1023K.

Emitter description		E_{cutoff} [eV]	Measurement Temperature T_h[a] [K]	E_{cutoff} / $k_B T_h$	ε_{out}[b]	ε_{in}[b]	*Ind. SE*[c]	*E* range [eV] / BB fraction[d]	Heat treatment conditions	Ref
Intrinsic	MgO with 2wt% NiO loading	0.65	1677	4.5	0.18	0.71	0.49	0.14-1.14 / 93%	1793K, duration omitted	[48]
	$Al_2O_3/Er_3Al_5O_{12}$ eutectic	0.73	1850	4.58	0.27	0.43	0.32	0.62-1.4 / 40%	In air at 1973K for 1000 hr	[41]
	Yb_2O_3 foam	1.12	1735	7.49	0.29	0.54	0.082	0.075-1.6 / 99%	1750K for 200 cycles, duration omitted	[59]
	Yb_2O_3 mantle	1.12	1735	7.49	0.14	0.62	0.18	0.024-1.6 / 99%	1750K for 200 cycles, duration omitted	[59]
Structured	Pt array on Al_2O_3/Pt	0.6	1273	5.47	0.47	0.93	0.25	0.25-1.4 / 76%	In Ar at 1273K for 2 hr	[25]
	W 2D cavity (D = 1.1μm) array	0.62	1200	6.00	0.25	0.86	0.294	0.16-1.3 / 90%	Under vacuum at 1200K for 10 hrs	[42]
	Ta 2D cavity array with HfO_2 coating	0.62	1255	5.73	0.34	0.89	0.275	0.41-0.89 / 40%	Under vacuum at 1273K for 1 hr / 1173K for 144 hr	[49]
	HfO_2 coated W inverse colloidal 3D PhC	0.67	1173	6.63	0.62	0.91	0.11	0.25-0.98 / 71%	In Ar at 1673K for 1 hr	[45]
	W 2D cavity (D = 900nm) array	0.73	1186	7.14	0.30	0.94	0.156	0.16-1.3 / 90%	Under vacuum at 1200K for 10 hrs	[42]

[a] T_h refers to the measurement temperature at which spectral emissivity was characterized.

[b] Weighted average out-of-band emissivity (ε_{out}) and in-band emissivity (ε_{in}) have been calculated using spectral properties collected from graphical data. Error may have resulted from the data extraction process.

[c] Individual *SE* calculations are based on spectral emissivity data. I extrapolate average emissivity values by band to the limits of integration to account for truncated data. Therefore, calculated values may deviate from those values reported elsewhere. I note the reported spectral range as a measure of certainty for individual *SE* calculations.

[d] The reported spectral range used to calculate *SE* and the fraction of the emissive power at the given T_h captured by this range are provided.

2.4.2 Selective cells

As introduced above, an alternative approach for spectral control is reflection of out-of-band radiation back to the emitter using a selectively absorptive cell. This is typically achieved through use of a back-surface reflector (BSR) (Figure 2.3e) and/or a front-surface filter (FSF) (Figure 2.3f). One practical advantage of this spectral control strategy is that pairs are not constrained by the requirement of material stability at high operating temperature. This may enable the design and use of a richer set of photonic architectures. This approach, however, is more sensitive to cavity non-idealities when compared to selective emitters, since well-insulated cavities are required to return reflected radiation back to the emitter.[60,61]

Figure 2.3d and Table 2.4 show the individual spectral efficiencies of representative TPV cells, given a blackbody emitter at the temperature indicated by the relevant publications. A 0.6 eV InGaAs cell developed by Wernsman, *et al*. has the highest individual spectral efficiency to date (62%).[24] Note, however, that this is not the same cell as that of the leading 0.6 eV InGaAs-based pair. This advance was enabled by utilization of a BSR and FSF to achieve low parasitic, out-of-band absorption and operation at a high emitter temperature, well-suited for the given bandgap.

Notably, other leading designs have performed similarly well out-of-band. Removal of the growth substrate from epitaxial cells has helped to improve *SE* by eliminating parasitic absorption associated with substrate counter-doping or buffer layers.[22,62] For example, Omair, et al. reported 94% out-of-band reflectance, enabled in part by removing the InP parent substrate.[22]

Beyond simple semiconductor-on-metal architectures, use of dielectric spacers at the back of the active layer has been shown to improve out-of-band reflectance for Ge, LM InGaAs, and InGaAsSb cells.[31,43,62,63] Fernandez, *et al.* report a Ge cell with a SiO_2 / Al BSR that exhibits a 5% absolute out-of-band reflectance improvement compared to the same cell with Al alone.[31] Further, Burger, *et al.* report 96% out-of-band reflectance for a LM InGaAs film with a MgF_2 / Au BSR, exceeding that of any cell surveyed here.[43]

Furthermore, this survey finds that there is room for significant improvements to in-band absorption in many TPV cells. Specifically, *SE* remains unoptimized for non-ideal in-band absorption. For example, the cell used in the leading LM InGaAs-based pair does not exhibit the highest *SE* mainly due to unoptimized in-band absorption.[22,23] Deposition of an ARC or surface texturing can improve in-band absorption, *SE*, and output power. For example, the individual *SE* of the LM InGaAs cell in the record-efficiency pair[22] would be improved by 7% absolute in the case of perfect in-band absorption. However, unintentional out-of-band absorption resulting from these treatments must be minimized to observe this benefit in practice.

Spectral utilization may also be improved through integration of additional absorbers. TPVs utilizing tandem cells may theoretically surpass the radiative limit *SE* defined above for a single-junction cell. The equation provided in Table 2.1 for calculating *SE* can be easily extended to multiple absorbers by splitting up the numerator to account for multiple bandgaps. Development of TPV pairs with tandem cells has been limited,[64–68] but theoretical studies are promising.[69]

Table 2.4. Selectively absorptive cells.

Material	E_g [eV]	T_h [K]	$E_g / k_B T_h$	ε_{out}[a]	ε_{in}[a]	*Individual SE*[b]	*E* range [eV] / BB fraction[c]	Ref
InGaAsSb	0.53	1273	4.83	0.24	0.95	0.44	0.31–1.24 / 64%	[62]
0.6 eV InGaAs	0.6	1312	5.31	0.06	0.76	0.62	0.06–1.48 / 99%	[24]
Ge	0.67	1373	5.66	0.56	0.80	0.18	0.50–4.94 / 37%	[31]
LM InGaAs	0.75	1480	5.88	0.06	0.68	0.53	0.08–0.99 / 95%	[22]
Si[d]	1.12	2300	5.65	0.05	0.55	0.56	-	[23]

[a]Weighted average ε_{out} and ε_{in} have been calculated using spectral properties collected from graphical data. Error may have resulted from the data extraction process.
[b]Individual *SE* calculations are based on spectral emissivity data. I extrapolate average emissivity values by band to the limits of integration to account for truncated data. Therefore, calculated values may deviate from those values reported elsewhere. I note the reported spectral range as a measure of certainty for individual *SE* calculations.
[c]The reported spectral range used to calculate *SE* and the fraction of the emissive power at the given T_h captured by this range are provided.
[d]In the case of Si, only ε_{out} is reported. I have supplemented this data with an estimate of ε_{in} based on optical simulation of the reported structures.

2.5 Charge carrier management

Once charges are photogenerated, cells must efficiently collect those charges while maximizing output voltage. Here, I analyze charge carrier management based on effective dark current density, J_0. To this end, I have calculated J_0 for leading TPV pairs given reported V_{oc}, J_{sc}, and T_c, by assuming an ideality factor, n, of 1 and neglecting shunt losses, using the ideal diode equation:

$$V_{oc} = \frac{k_B T_c}{q} \ln\left(\frac{J_{sc}}{J_0} + 1\right) \tag{2.1}$$

Whereas voltage factors are heavily dependent on testing conditions (V_{oc} increases logarithmically with illumination intensity), J_0 offers a more objective metric; it normalizes for the effects of variable illumination and omits the effects of Ohmic loss.

J_0 values for leading TPV cells are compared to the theoretical minimum with and without photon recycling (Figure 2.4). In either case, dark current is expected to decrease with increasing bandgap, as the recombination rates scale with the intrinsic carrier concentration.

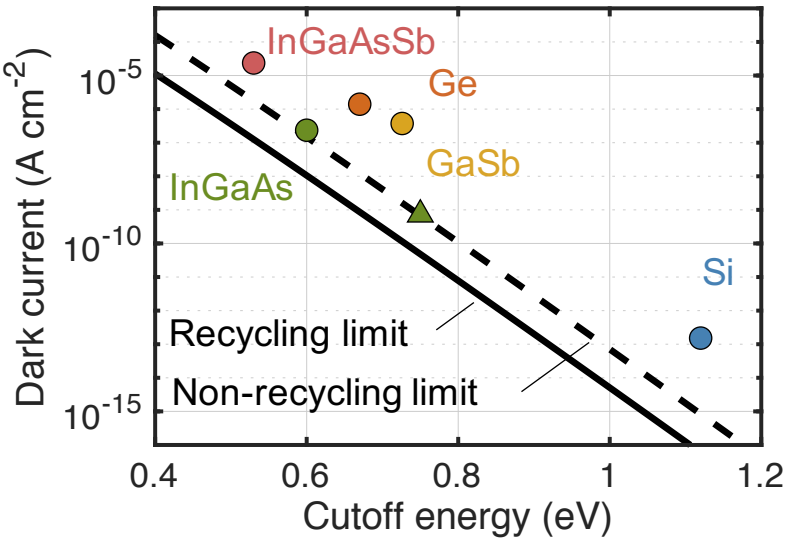

Figure 2.4. Effective dark current density of leading TPV cells. Radiative limit dark current density with (solid curve) and without (dashed curve) internal photon recycling. Reporting literature: InGaAsSb[26]; 0.6 eV InGaAs[25]; Ge[31]; GaSb[16]; LM InGaAs[22] (triangular marker); Si.[23]

I observe that leading pairs with InGaAs cells of both compositions (0.6 eV and LM) exhibit low dark current densities, approaching the non-recycling radiative limit. Thin, crystalline materials, such as these leading InGaAs cells, benefit from high quality growth, limiting defect-mediated carrier recombination. The thin-film geometry can also enhance internal recycling of luminescent photons, further reducing net recombination.[70–74]

In contrast, GaSb cells exhibit dark current densities nearly two orders of magnitude greater than the non-recycling radiative limit. Prior studies have primarily attributed losses in GaSb to defect-mediated recombination.[75] Development of doping techniques in GaSb without introducing recombination centers is an ongoing area of research.[76,77]

Poor dark current among other cell materials considered here may further be the result of technological immaturity. While Si- and Ge-containing cells have witnessed remarkable strides in solar PV applications, development of Si and Ge cells for TPV systems has been limited. Notably, leading Si solar PV cells[35,36] have ten-fold lower dark current densities than the Si cell in the leading TPV pair.[23] Although they face unique challenges, it appears that TPV cells stand to benefit significantly from advances in semiconductor growth and manufacturing to bridge the gap with leading solar cells in terms of charge carrier management. This survey reveals that the following design considerations may generally improve carrier management:

(i) Minimizing series resistance

Whereas Ohmic losses in leading solar PV configurations are effectively negligible,[35–37] TPV pairs are prone to Ohmic losses, which adversely affect fill factor, since they scale quadratically with current density ($P_{Ohmic\ loss} = R_s \cdot J_{MPP}^2$). For example, the LM InGaAs cell in the leading pair exhibits R_s of 0.044 Ω cm^2, resulting in an 8% loss in power output.[22] Given that high power density could be a major advantage for TPV generators, in terms of cost per power ($/W), alleviating Ohmic losses for high power systems is essential for enabling practical implementation. Lowering series resistance to acceptable levels may require further development and optimization

of transparent lateral conduction layers, low interfacial resistance contacts, and metal grids. These considerations are also critical for near-field TPV configurations because of their enhanced power density.[78–84]

(ii) Thermal management at the cell

Elevated cell temperature results in increased dark current, decreased V_{oc}, and degraded $\eta_{pairwise}$. For example, Wernsman, et al. observe a 43 mV drop in V_{oc} when a 0.6 eV InGaAs cell is heated from 24 to 64 °C, resulting in a 3.6% absolute drop in $\eta_{pairwise}$ under constant illumination.[24] While passive techniques for heat dissipation are attractive, Blandre, *et al.* show that active cooling techniques may be necessary to meet cooling demands at high power densities.[85] Though emitter-cell pairs typically require active cooling to maintain cell temperature during characterization at high power densities, $\eta_{pairwise}$ is not penalized by this power consumption. As materials transition to prototypes, power consumed for circulating coolant may reduce overall efficiency, but this effect is expected to be small (<5%) with state-of-the-art thermal management systems.[86–88]

(iii) Enhancing internal photon recycling

High back-surface reflectance near the band-edge has been shown to produce V_{oc} gains in high-quality solar cells.[70,71,73,74] This effect has yet to be demonstrated in TPV pairs, as radiative recombination is not sufficiently dominant.[22] Nevertheless, recent cell-side spectral engineering efforts (discussed in the previous section) are synergistic with this goal.[22,43]

(iv) Multi-junction cells

Beyond the potential for enhanced *SE*, multi-junction cells can enhance V_{oc} and lower J_{sc} compared to single-junction cells. This approach reduces Ohmic losses, which scale quadratically with photocurrent. Ohmic losses are considerably more important for TPV generators compared to their solar counterparts.

2.6. TPV sub-system efficiencies

Major improvements in efficiency measured under idealized conditions are necessary, but not sufficient, for widespread adoption of TPV technology. The performance of emitter-cell pairs needs to translate to prototypes and ultimately generators. This has been an emphasis of many TPV efforts since the early work of Swanson. In particular, significant advancements were made toward practical implementation of TPV materials by improving emitter stability, on one hand, and developing quality narrow-bandgap cells that require lower heat source temperatures, on the other. This section considers the performance of leading TPV sub-systems and discuss the primary losses resulting in the observed performance gap.

Here I consider TPV sub-system efficiency η_{TPV} as an intermediate performance metric for transition from emitter-cell pairs to prototypes, which captures losses related to imperfect component integration, such as absorption by inactive regions of the cell, non-ideal view factors, and convective loss from the emitter.

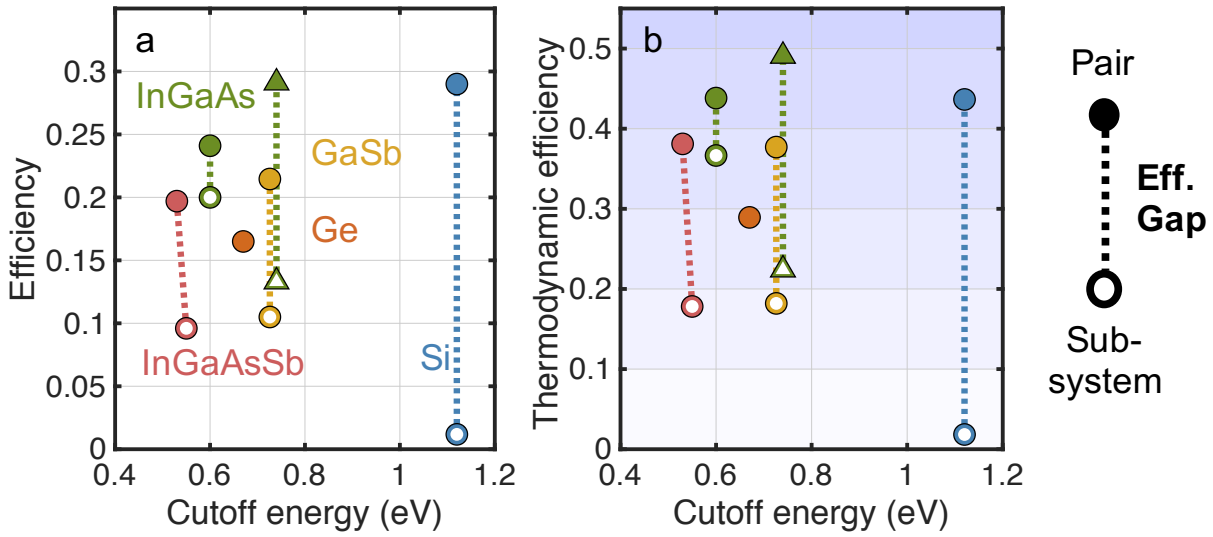

Figure 2.5. Gaps between pairwise and TPV sub-system efficiencies. Leading pairwise cell efficiencies compared to record sub-system efficiencies. Reporting literature: InGaAsSb[14,26]; 0.6 eV InGaAs[25,89]; Ge[31]; GaSb[15,16]; LM InGaAs[19,22] (triangular marker); Si.[23,90]

Like my survey of emitter-cell pairs, I have identified reports of record-high η_{TPV} among groups by cell material. For 0.6 eV InGaAs- and Si-based sub-systems, η_{TPV} has been measured directly. For InGaAsSb-, GaSb-, and LM InGaAs-based sub-systems, it was deduced from simulated loss breakdowns. For all cases, a notable efficiency gap is observed between leading TPV emitter-cell pairs and leading TPV sub-systems as shown in Figure 2.5a. However, leading TPV sub-systems do not necessarily make use of leading emitter-cell materials considered previously. Therefore, gaps between $\eta_{pairwise}$ and η_{TPV} should not be fully attributed to *CE*. Overall, sub-systems with wider bandgap cells (e.g., Si) appear to be more susceptible to these issues. To account for different testing conditions, which could be a confounding variable, I further normalize sub-system η_{TPV} with respect to the radiative limit to account for variable T_h and other factors. However, Figure 2.5b shows that the observed gap persists even when comparing thermodynamic efficiencies. To help rationalize the performance gap, consider the effects of imperfect component integration and scale-up.

Each leading TPV sub-system utilizes a vacuum environment to ensure emitter stability and eliminate convective heat transfer losses. Therefore, the cavity efficiencies of these TPV sub-systems are primarily dependent on their geometrical design, including the view factor between the cell and emitter. Consider, for example, the case of 0.6 eV InGaAs. The highest reported η_{TPV} for a 0.6 eV InGaAs sub-system is 20%,[18] short of the 23.6% pairwise efficiency reported for the same cell under a lamp.[24] In a related report, Crowley, *et al.* attribute this gap to imperfect cavity efficiency, non-uniform cell illumination and inefficiencies related to cell interconnections.[89] This sub-system relies on a selective cell to achieve spectral control, and is therefore more susceptible to cavity losses. These loss pathways are common among other sub-systems as well. In the case of GaSb, Bhatt *et al.* report a view factor of 0.85 and attribute this high cavity loss to the small area of the cell relative to the emitter.[15] Nonetheless, many of the sub-system heat losses that severely restrict efficiency can be minimized as leading emitter-cell pairs reach the kW-scale.[14]

In addition to cavity imperfections, it appears that material supply/scaling issues may also be a factor in some of the observed performance gaps. Both the leading LM InGaAs- and InGaAsSb-based sub-systems have well-designed cavities with view factors of 0.97 and 0.96, respectively.[14,19] Thus, the drop-off in performance is likely because the LM InGaAs and InGaAsSb cells used in the sub-system did not perform as well as the champion cells.

As TPVs transition toward commercialization, it will become increasingly necessary to address cavity inefficiencies and other scaling issues. One prior study has proposed several design strategies for reducing system sensitivity to cavity losses.[60] For example, increasing spectral

overlap by increasing the ratio of the emitter temperature to the bandgap is expected to make TPV sub-systems less susceptible to such losses. Multi-junction designs, especially, offer a practical means of increasing spectral overlap, lowering Ohmic losses, and improving resistance to cavity inefficiencies. Further, utilization of a selective emitter, even in tandem with a selectively absorptive cell, can reduce sensitivity to parasitic optical loss.

2.7. Discussion

This review identifies major opportunities for TPV research by comparing leading emitter-cell pairs and sub-systems, spanning a wide range of cell materials (0.5-1.1 eV), to thermodynamic limits. In the near term, it appears that TPV pairs can benefit from certain designs that have advanced the performance of solar cells. For example, design choices that have enhanced internal recycling of luminescent photons, such as high back-surface reflectance, can also enable recycling of low energy photons – a key factor in TPV efficiency. However, TPV generators are faced with unique challenges such as thermal stability of the emitter, tension between cost per power and Ohmic losses associated with high current densities, and a noticeable gap in performance when translating to sub-systems. The development of substrate reuse methods and multi-junction cells will likely alleviate some of these intrinsic trade-offs. Furthermore, novel approaches such as nano-structuring, spectral splitting, and near-field control may also help circumvent these issues. Several non-technical challenges also need be addressed. Namely, the field has yet to reach a consensus regarding efficiency testing and reporting, which would streamline the process of identifying favorable designs and recognizing new advances. Whether the full potential of TPVs will be reached – providing power on demand, near the point-of-use, and enabling greater integration of intermittent renewables – remains to be determined. Nonetheless, it appears that a substantial gain

in performance is within reach if sufficient resources are devoted to overcoming the challenges outlined in this review.

2.8 References

1. Polman, A., Knight, M., Garnett, E.C., Ehrler, B., and Sinke, W.C. (2016). Photovoltaic materials: Present efficiencies and future challenges. Science (80-.). *352*, aad4424–aad4424.
2. Shockley, W., and Queisser, H.J. (1961). Detailed Balance Limit of Efficiency of p-n Junction Solar Cells. J. Appl. Phys. *32*, 510–519.
3. Harder, N.-P., and W rfel, P. (2003). Theoretical limits of thermophotovoltaic solar energy conversion. Semicond. Sci. Technol. *18*, S151–S157.
4. Green, M.A. (2006). Third generation photovoltaics: advanced solar energy conversion (Springer).
5. Mauk, M.G. (2006). Survey of Thermophotovoltaic (TPV) Devices. In Mid-infrared Semiconductor Optoelectronics (Springer London), pp. 673–738.
6. Zhou, Z., Sakr, E., Sun, Y., and Bermel, P. (2016). Solar thermophotovoltaics: reshaping the solar spectrum. Nanophotonics *5*, 1–21.
7. Datas, A., and Martí, A. (2017). Thermophotovoltaic energy in space applications: Review and future potential. Sol. Energy Mater. Sol. Cells *161*, 285–296.
8. Ferrari, C., and Melino, F. (2014). Overview and Status of Thermophotovoltaic Systems. Energy Procedia *45*, 160–169.
9. Daneshvar, H., Prinja, R., and Kherani, N.P. (2015). Thermophotovoltaics: Fundamentals, challenges and prospects. Appl. Energy *159*, 560–575.
10. Sakakibara, R., Stelmakh, V., Chan, W.R., Ghebrebrhan, M., Joannopoulos, J.D., Soljačić, M., and Čelanović, I. (2019). Practical emitters for thermophotovoltaics: a review. J. Photonics Energy *9*, 032713.
11. Amy, C., Seyf, H.R., Steiner, M.A., Friedman, D.J., and Henry, A. (2019). Thermal energy grid storage using multi-junction photovoltaics. Energy Environ. Sci. *12*, 334–343.
12. Lenert, A., Bierman, D.M., Nam, Y., Chan, W.R., Celanović, I., Soljačić, M., and Wang, E.N. (2014). A nanophotonic solar thermophotovoltaic device. Nat. Nanotechnol. *9*, 126–130.
13. Ungaro, C., Gray, S.K., and Gupta, M.C. (2015). Solar thermophotovoltaic system using nanostructures. Opt. Express *23*, A1149–A1156.
14. Bierman, D.M., Lenert, A., Chan, W.R., Bhatia, B., Celanović, I., Soljačić, M., and Wang, E.N. (2016). Enhanced photovoltaic energy conversion using thermally based spectral shaping. Nat. Energy *1*, 16068.
15. Bhatt, R., Kravchenko, I., and Gupta, M. (2020). High-efficiency solar thermophotovoltaic system using a nanostructure-based selective emitter. Sol. Energy *197*, 538–545.
16. Fraas, L.M., Samaras, J.E., Huang, H.X., Minkin, L.M., Avery, J.E., Daniels, W.E., and Hui, S. (2001). TPV generators using the radiant tube burner configuration. In Proc. 17th European PVSEC.
17. Bitnar, B., Durisch, W., and Holzner, R. (2013). Thermophotovoltaics on the move to applications. Appl. Energy *105*, 430–438.
18. Wilt, D., Chubb, D., Wolford, D., Magari, P., and Crowley, C. (2007). Thermophotovoltaics for Space Power Applications. AIP Conf. Proc. *890*, 335–345.
19. Suemitsu, M., Asano, T., Inoue, T., and Noda, S. (2020). High-Efficiency Thermophotovoltaic System That Employs an Emitter Based on a Silicon Rod-Type Photonic Crystal. ACS Photonics *7*, 80–87.

20. Mahorter, R.G., Wernsman, B., Thomas, R.M., and Siergiej, R.R. (2003). Thermophotovoltaic system testing. Semicond. Sci. Technol. *18*, S232–S238.
21. Henry, C.H. (1980). Limiting efficiencies of ideal single and multiple energy gap terrestrial solar cells. J. Appl. Phys. *51*, 4494–4500.
22. Omair, Z., Scranton, G., Pazos-Outón, L.M., Xiao, T.P., Steiner, M.A., Ganapati, V., Peterson, P.F., Holzrichter, J., Atwater, H., and Yablonovitch, E. (2019). Ultraefficient thermophotovoltaic power conversion by band-edge spectral filtering. Proc. Natl. Acad. Sci. *116*, 15356–15361.
23. Swanson, R.M. (1980). Recent developments in thermophotovoltaic conversion. In 1980 International Electron Devices Meeting (IRE), pp. 186–189.
24. Wernsman, B., Siergiej, R.R., Link, S.D., Mahorter, R.G., Palmisiano, M.N., Wehrer, R.J., Schultz, R.W., Schmuck, G.P., Messham, R.L., Murray, S., et al. (2004). Greater Than 20% Radiant Heat Conversion Efficiency of a Thermophotovoltaic Radiator/Module System Using Reflective Spectral Control. IEEE Trans. Electron Devices *51*, 512–515.
25. Woolf, D.N., Kadlec, E.A., Bethke, D., Grine, A.D., Nogan, J.J., Cederberg, J.G., Bruce Burckel, D., Luk, T.S., Shaner, E.A., and Hensley, J.M. (2018). High-efficiency thermophotovoltaic energy conversion enabled by a metamaterial selective emitter. Optica *5*, 213.
26. Dashiell, M.W., Beausang, J.F., Ehsani, H., Nichols, G.J., Depoy, D.M., Danielson, L.R., Talamo, P., Rahner, K.D., Brown, E.J., Burger, S.R., et al. (2006). Quaternary InGaAsSb Thermophotovoltaic Diodes. IEEE Trans. Electron Devices *53*, 2879–2891.
27. Brown, E., Baldasaro, P., Burger, S., Danielson, L., DePoy, D., Dolatowski, J., Fourspring, P., Nichols, G., Topper, W., and Rahmlow, T. (2004). Status of Thermophotovoltaic Energy Conversion Technology at Lockheed Martin Corp. In 2nd International Energy Conversion Engineering Conference (American Institute of Aeronautics and Astronautics), pp. 1–20.
28. Yu, Y.Z., Martinelli, R.U., Taylor, G.C., Shellenbarger, Z., Smeltzer, R.K., Li, J., Palit, K., Burger, S.R., Cardines, R.P., Danielson, L.R., et al. (2003). High-Efficiency Multi-Cell TPV Module Fabrication and Performance. AIP Conf. Proc. *653*, 335–343.
29. Siergiej, R.R., Wernsman, B., Derry, S.A., Mahorter, R.G., Wehrer, R.J., Link, S.D., Palmisiano, M.N., Messhan, R.L., Murray, S., Murray, C.S., et al. (2003). 20% Efficient InGaAs/InPAs Thermophotovoltaic Cells. AIP Conf. Proc. *653*, 414–423.
30. Wedlock, B.D. (1963). Thermo-photo-voltaic energy conversion. Proc. IEEE *51*, 694–698.
31. Fernández, J., Dimroth, F., Oliva, E., Hermle, M., and Bett, A.W. (2007). Back-surface Optimization of Germanium TPV Cells. AIP Conf. Proc. *890*, 190–197.
32. Wilt, D.M., Fatemi, S., Hoffman, R.W., Jenkins, P.P., Scheiman, D., Lowe, R., and Landis, G.A. (1995). InGaAs PV device development for TPV power systems. AIP Conf. Proc. *321*, 210–220.
33. Swanson, R.M. (1978). Silicon photovoltaic cells in thermophotovoltaic energy conversion. In 1978 International Electron Devices Meeting (IRE), pp. 70–73.
34. Green, M.A., Hishikawa, Y., Dunlop, E.D., Levi, D.H., Hohl-Ebinger, J., Yoshita, M., and Ho-Baillie, A.W.Y. (2019). Solar cell efficiency tables (version 54). Prog. Photovoltaics Res. Appl. *27*, 3–12.
35. Haase, F., Hollemann, C., Schäfer, S., Merkle, A., Rienäcker, M., Krügener, J., Brendel, R., and Peibst, R. (2018). Laser contact openings for local poly-Si-metal contacts enabling 26.1%-efficient POLO-IBC solar cells. Sol. Energy Mater. Sol. Cells *186*, 184–193.
36. Yoshikawa, K., Kawasaki, H., Yoshida, W., Irie, T., Konishi, K., Nakano, K., Uto, T.,

Adachi, D., Kanematsu, M., Uzu, H., et al. (2017). Silicon heterojunction solar cell with interdigitated back contacts for a photoconversion efficiency over 26%. Nat. Energy *2*, 17032.

37. Kayes, B.M., Nie, H., Twist, R., Spruytte, S.G., Reinhardt, F., Kizilyalli, I.C., and Higashi, G.S. (2011). 27.6% Conversion efficiency, a new record for single-junction solar cells under 1 sun illumination. In 2011 37th IEEE Photovoltaic Specialists Conference (IEEE), pp. 000004–000008.
38. Geisz, J.F., Steiner, M.A., García, I., Kurtz, S.R., and Friedman, D.J. (2013). Enhanced external radiative efficiency for 20.8% efficient single-junction GaInP solar cells. Appl. Phys. Lett. *103*, 1–5.
39. Cederberg, J.G., Blaich, J.D., Girard, G.R., Lee, S.R., Nelson, D.P., and Murray, C.S. (2008). The development of (InGa)As thermophotovoltaic cells on InP using strain-relaxed In(PAs) buffers. J. Cryst. Growth *310*, 3453–3458.
40. Rinnerbauer, V., Ndao, S., Yeng, Y.X., Chan, W.R., Senkevich, J.J., Joannopoulos, J.D., Soljačić, M., and Celanovic, I. (2012). Recent developments in high-temperature photonic crystals for energy conversion. Energy Environ. Sci. *5*, 8815.
41. Nakagawa, N., Ohtsubo, H., Waku, Y., and Yugami, H. (2005). Thermal emission properties of Al2O3/Er3Al5O12 eutectic ceramics. J. Eur. Ceram. Soc. *25*, 1285–1291.
42. Yeng, Y.X., Ghebrebrhan, M., Bermel, P., Chan, W.R., Joannopoulos, J.D., Soljacic, M., and Celanovic, I. (2012). Enabling high-temperature nanophotonics for energy applications. Proc. Natl. Acad. Sci. *109*, 2280–2285.
43. Burger, T., Fan, D., Lee, K., Forrest, S.R., and Lenert, A. (2018). Thin-Film Architectures with High Spectral Selectivity for Thermophotovoltaic Cells. ACS Photonics *5*, 2748–2754.
44. Shemelya, C., DeMeo, D.F., and Vandervelde, T.E. (2014). Two dimensional metallic photonic crystals for light trapping and anti-reflective coatings in thermophotovoltaic applications. Appl. Phys. Lett. *104*, 021115.
45. Arpin, K.A., Losego, M.D., Cloud, A.N., Ning, H., Mallek, J., Sergeant, N.P., Zhu, L., Yu, Z., Kalanyan, B., Parsons, G.N., et al. (2013). Three-dimensional self-assembled photonic crystals with high temperature stability for thermal emission modification. Nat. Commun. *4*, 2630.
46. Cao, F., Kraemer, D., Tang, L., Li, Y., Litvinchuk, A.P., Bao, J., Chen, G., and Ren, Z. (2015). A high-performance spectrally-selective solar absorber based on a yttria-stabilized zirconia cermet with high-temperature stability. Energy Environ. Sci. *8*, 3040–3048.
47. Baranov, D.G., Xiao, Y., Nechepurenko, I.A., Krasnok, A., Alù, A., and Kats, M.A. (2019). Nanophotonic engineering of far-field thermal emitters. Nat. Mater. *18*, 920–930.
48. Ferguson, L.G., and Dogan, F. (2001). A highly efficient NiO-Doped MgO matched emitter for thermophotovoltaic energy conversion. Mater. Sci. Eng. B *83*, 35–41.
49. Rinnerbauer, V., Yeng, Y.X., Chan, W.R., Senkevich, J.J., Joannopoulos, J.D., Soljačić, M., and Celanovic, I. (2013). High-temperature stability and selective thermal emission of polycrystalline tantalum photonic crystals. Opt. Express *21*, 11482.
50. Wang, Y., Zhou, L., Zhang, Y., Yu, J., Huang, B., Wang, Y., Lai, Y., Zhu, S., and Zhu, J. (2018). Hybrid Solar Absorber–Emitter by Coherence-Enhanced Absorption for Improved Solar Thermophotovoltaic Conversion. Adv. Opt. Mater. *6*, 1800813.
51. Chirumamilla, M., Krishnamurthy, G.V., Knopp, K., Krekeler, T., Graf, M., Jalas, D., Ritter, M., Störmer, M., Petrov, A.Y., and Eich, M. (2019). Metamaterial emitter for thermophotovoltaics stable up to 1400 °C. Sci. Rep. *9*, 7241.

52. Chirumamilla, M., Krishnamurthy, G.V., Rout, S.S., Ritter, M., Störmer, M., Petrov, A.Y., and Eich, M. (2020). Thermal stability of tungsten based metamaterial emitter under medium vacuum and inert gas conditions. Sci. Rep. *10*, 3605.
53. Nagpal, P., Josephson, D.P., Denny, N.R., DeWilde, J., Norris, D.J., and Stein, A. (2011). Fabrication of carbon/refractory metal nanocomposites as thermally stable metallic photonic crystals. J. Mater. Chem. *21*, 10836.
54. Arpin, K.A., Losego, M.D., and Braun, P. V. (2011). Electrodeposited 3D Tungsten Photonic Crystals with Enhanced Thermal Stability. Chem. Mater. *23*, 4783–4788.
55. Schlemmer, C., Aschaber, J., Boerner, V., and Luther, J. (2003). Thermal stability of micro-structured selective tungsten emitters. AIP Conf. Proc. *653*, 164–173.
56. Lee, H.J., Smyth, K., Bathurst, S., Chou, J., Ghebrebrhan, M., Joannopoulos, J., Saka, N., and Kim, S.G. (2013). Hafnia-plugged microcavities for thermal stability of selective emitters. Appl. Phys. Lett. *102*, 1–5.
57. Peykov, D., Yeng, Y.X., Celanovic, I., Joannopoulos, J.D., and Schuh, C.A. (2015). Effects of surface diffusion on high temperature selective emitters. Opt. Express *23*, 9979.
58. Abbas, R., Muñoz, J., and Martínez-Val, J.M. (2012). Steady-state thermal analysis of an innovative receiver for linear Fresnel reflectors. Appl. Energy *92*, 503–515.
59. Bitnar, S., Durisch, W., Palfinger, G., von Roth, F., Vogt, U., Brönstrup, A., and Seiler, D. (2004). Practical thermophotovoltaic generators. Semiconductors *38*, 941–945.
60. Raman, V.K., Burger, T., and Lenert, A. (2019). Design of thermophotovoltaics for tolerance of parasitic absorption. Opt. Express *27*, 31757.
61. Baldasaro, P.F., Raynolds, J.E., Charache, G.W., DePoy, D.M., Ballinger, C.T., Donovan, T., and Borrego, J.M. (2001). Thermodynamic analysis of thermophotovoltaic efficiency and power density tradeoffs. J. Appl. Phys. *89*, 3319–3327.
62. Wang, C. a, Shiau, D. a, Murphy, P.G., O'Brien, P.W., Huang, R.K., Connors, M.K., Anderson, a C., Donetsky, D., Anikeev, S., Belenky, G., et al. (2004). Wafer bonding and epitaxial transfer of GaSb-based epitaxy to GaAs for monolithic interconnection of thermophotovoltaic devices. J. Electron. Mater. *33*, 213–217.
63. Wu, X., Duda, A., Carapella, J.J., Ward, J.S., Webb, J.D., and Wanlass, M.W. (1999). A Study of Contacts and Back-Surface Reflectors Interconnected Modules. *517*.
64. Shvarts, M.Z.Z., Andreev, V.M.M., Khvostikov, V.P.P., Rumyantsev, V.D.D., Sorokina, S.V., Vasil'ev, V.I., Vlasov, A.S., Chosta, O.I., Larinov, V.R., and Rumyantsev, V.D.D. (1998). GaSb/InGaAsSb tandem thermophotovoltaic cells for space applications. Proc. Fifth Eur. Sp. Power Conf., 527.
65. Siergiej, R.R., Sinharoy, S., Valko, T., Wehrer, R.J., Wernsman, B., Link, S.D., Schultz, R.W., and Messham, R.L. (2004). InGaAsP/InGaAs Tandem TPV Device. In AIP Conference Proceedings (AIP), pp. 480–488.
66. Andreev, V.M., Khvostikov, V.P., Rumyantsev, V.D., Sorokina, S. V., and Shvarts, M.Z. (2000). Single-junction GaSb and tandem GaSb/InGaAsSb & AlGaAsSb/GaSb thermophotovoltaic cells. Conf. Rec. IEEE Photovolt. Spec. Conf. *2000-Janua*, 1265–1268.
67. Wehrer, R., Wanlass, M., Wilt, D., Wernsman, B., Siergiej, R., and Carapella, J. (2003). InGaAs series-connected, tandem, MIM TPV converters. Proc. 3rd World Conf. Photovolt. Energy Convers. *A*, 892–895.
68. Siergiej, R.R., Wernsman, B., Derry, S.A., Wehrer, R.J., Link, S.D., Palmisiano, M.N., Riley, D.R., Murray, C.S., Newman, F., and Hills, J. (2000). High efficiency, large area, InGaAs/InPAs thermophotovoltaic cells. In Device Research Conference. Conference

Digest (Cat. No.01TH8561) (IEEE), pp. 159–160.
69. Datas, A. (2015). Optimum semiconductor bandgaps in single junction and multijunction thermophotovoltaic converters. Sol. Energy Mater. Sol. Cells *134*, 275–290.
70. Steiner, M.A., Geisz, J.F., García, I., Friedman, D.J., Duda, A., and Kurtz, S.R. (2013). Optical enhancement of the open-circuit voltage in high quality GaAs solar cells. J. Appl. Phys. *113*, 123109.
71. Schilling, C.L., Hohn, O., Micha, D.N., Heckelmann, S., Klinger, V., Oliva, E., Glunz, S.W., and Dimroth, F. (2018). Combining Photon Recycling and Concentrated Illumination in a GaAs Heterojunction Solar Cell. IEEE J. Photovoltaics *8*, 348–354.
72. Miller, O.D., Yablonovitch, E., and Kurtz, S.R. (2012). Strong Internal and External Luminescence as Solar Cells Approach the Shockley–Queisser Limit. IEEE J. Photovoltaics *2*, 303–311.
73. Kosten, E.D., Atwater, J.H., Parsons, J., Polman, A., and Atwater, H.A. (2013). Highly efficient GaAs solar cells by limiting light emission angle. Light Sci. Appl. *2*, 1–6.
74. Boriskina, S. V, Green, M.A., Catchpole, K., Yablonovitch, E., Beard, M.C., Okada, Y., Lany, S., Gershon, T., Zakutayev, A., Tahersima, M.H., et al. (2016). Roadmap on optical energy conversion. J. Opt. *18*, 073004.
75. Algora, C. (2003). Modelling And Manufacturing GaSb TPV Converters. 452–461.
76. Tang, L., Fraas, L.M., Liu, Z., Xu, C., and Chen, X. (2015). Performance Improvement of the GaSb Thermophotovoltaic Cells With n-Type Emitters. IEEE Trans. Electron Devices *62*, 2809–2815.
77. Tang, L., Fraas, L.M., Liu, Z., Zhang, Y., Duan, H., and Xu, C. (2019). N-type vapor diffusion for the fabrication of GaSb thermophotovoltaic cells to increase the quantum efficiency in the long wavelength range. Sol. Energy Mater. Sol. Cells *194*, 137–141.
78. Molesky, S., and Jacob, Z. (2015). Ideal near-field thermophotovoltaic cells. Phys. Rev. B - Condens. Matter Mater. Phys. *91*, 1–7.
79. Chen, K., Santhanam, P., and Fan, S. (2015). Suppressing sub-bandgap phonon-polariton heat transfer in near-field thermophotovoltaic devices for waste heat recovery. Appl. Phys. Lett. *107*, 091106.
80. Fiorino, A., Zhu, L., Thompson, D., Mittapally, R., Reddy, P., and Meyhofer, E. (2018). Nanogap near-field thermophotovoltaics. Nat. Nanotechnol. *13*, 806–811.
81. Tervo, E., Bagherisereshki, E., and Zhang, Z. (2018). Near-field radiative thermoelectric energy converters: a review. Front. Energy *12*, 5–21.
82. DeSutter, J., Tang, L., and Francoeur, M. (2019). A near-field radiative heat transfer device. Nat. Nanotechnol. *14*, 751–755.
83. McSherry, S., Burger, T., and Lenert, A. (2019). Effects of narrowband transport on near-field and far-field thermophotonic conversion. J. Photonics Energy *9*, 1.
84. Papadakis, G.T., Buddhiraju, S., Zhao, Z., Zhao, B., and Fan, S. (2020). Broadening near-field emission performance enhancement in thermophotovoltaics. Nano Lett.
85. Blandre, E., Vaillon, R., and Drévillon, J. (2019). New insights into the thermal behavior and management of thermophotovoltaic systems. Opt. Express *27*, 36340.
86. Stark, A.K., and Klausner, J.F. (2017). An R&D Strategy to Decouple Energy from Water. Joule *1*, 416–420.
87. Wen, R., Ma, X., Lee, Y.C., and Yang, R. (2018). Liquid-Vapor Phase-Change Heat Transfer on Functionalized Nanowired Surfaces and Beyond. Joule *2*, 2307–2347.
88. Weinstein, L.A., McEnaney, K., Strobach, E., Yang, S., Bhatia, B., Zhao, L., Huang, Y.,

Loomis, J., Cao, F., Boriskina, S. V., et al. (2018). A Hybrid Electric and Thermal Solar Receiver. Joule *2*, 962–975.

89. Crowley, C.J. (2005). Thermophotovoltaic Converter Performance for Radioisotope Power Systems. AIP Conf. Proc. *746*, 601–614.
90. Yeng, Y.X., Chan, W.R., Rinnerbauer, V., Stelmakh, V., Senkevich, J.J., Joannopoulos, J.D., Soljacic, M., and Čelanović, I. (2015). Photonic crystal enhanced silicon cell based thermophotovoltaic systems. Opt. Express *23*, A157.

Chapter 3: Thin-Film Architectures with High Spectral Selectivity for Thermophotovoltaic Cells

3.1 Motivation

The transport of out-of-band radiation between the thermal emitter and PV cell should be suppressed in thermophotovoltaic (TPV) systems to achieve high conversion efficiency. [1–8] This can be achieved by recycling out-of-band radiation back to the emitter using a spectrally selective cell. However, conventional TPV cells, in which the growth substrate is used in the device, reflect less than 95% of out-of-band radiation.[4–6,9]

This chapter describes the design and characterization of thin-film optical structures fabricated using epitaxial lift-off to improve selective radiative transfer. A significant enhancement in spectral selectivity, relative to conventional TPVs, was measured in thin-film $In_{0.53}Ga_{0.47}As$ (hereafter InGaAs) structures because of the reduced optical path and optimized interference. Record-high average out-of-band reflectance of 96% is reported for one structure, which includes a dielectric rear spacer layer. Further, a parallel-plate TPV model predicts the impact of specific structural features on performance and is leveraged to optimize cell architectures. A dielectric spacer between the InGaAs absorber layer and the Au back contact is shown to be an important structural feature that enables a predicted TPV efficiency above 50% (with a power output of

2.1 W/cm^2), significantly higher than current TPV devices. Beyond their optical advantages over conventional cells, thin-film cells fabricated using epitaxial lift-off have the potential to increase external luminescent efficiency[8] and to reduce the cost of TPV generators by reusing expensive III-V substrates.[1,6,10–13]

This work would not have been possible without the contributions of my co-author, Dejiu Fan. Dejiu developed and implemented the fabrication protocol for realizing the described thin-film InGaAs optical structures.

3.2 State-of-the-art spectral control techniques

This work builds on past techniques for enhanced spectral selectivity that can be broadly categorized as either emission control or absorption control.[3–5,9,14–18] Several studies have utilized nanophotonic emitters to selectively emit radiation above the PV cell bandgap.[15–19] However, reduced selectivity at high operating temperatures limits the effectiveness of this emission control strategy.[20–26] Furthermore, the long-term thermal stability of nanostructured emitters has yet to be addressed.

Alternatively, PV cells exhibiting selective absorption have facilitated recycling of low-energy photons, and consequently, improved efficiency.[3–5,9] This approach makes use of a cell with a back surface reflector (BSR) or a front surface filter (FSF) to reflect radiation with energy lower than the semiconductor bandgap, while absorbing radiation with higher energies.[3–5,9] Low-energy photons reflected by the cell are re-absorbed by the thermal emitter, decreasing net heat transfer between the emitter and cell (Q_h) without decreasing output power (P_{out}) (Figure 3.1a). An early

demonstration of selective absorption in a Si cell with a Ag BSR reached a thermal-to-electrical conversion efficiency of 29% for an emitter temperature of 2300 K.[27] Utilization of lower bandgap cells has enabled similar efficiencies at moderate temperatures. Siergiej, *et al*. utilized a 0.6 eV InGaAs cell with a Si_3N_4/Au BSR to achieve an efficiency of 20.6% for a 1330 K emitter.[4] Deposition of a dielectric spacer layer on the BSR helps to mitigate out-of-band absorption by decreasing the intensity of radiation at the absorbing metallic surface.[28–30] This cell was later modified to include a FSF, increasing its efficiency to 23.6%.[5] The measured spectral selectivity of these approaches, however, has been limited by absorption of out-of-band radiation due to a variety of possible mechanisms including parasitic absorption in the growth substrate.[4–6,9] There has been only one demonstration of a thin-film TPV device, an InGaAsSb cell with a SiO_x spacer and a Au BSR.[29] However, the destructive substrate removal process used to fabricate this device makes it incompatible with wafer reuse. Further, the device exhibits limited spectral selectivity, speculated to be the result of out-of-band absorption by macro-scale defects resulting from substrate removal. The structures presented here exhibit higher reflectance below the semiconductor bandgap than previous TPV cells, coupled with high absorption of radiation above the bandgap.

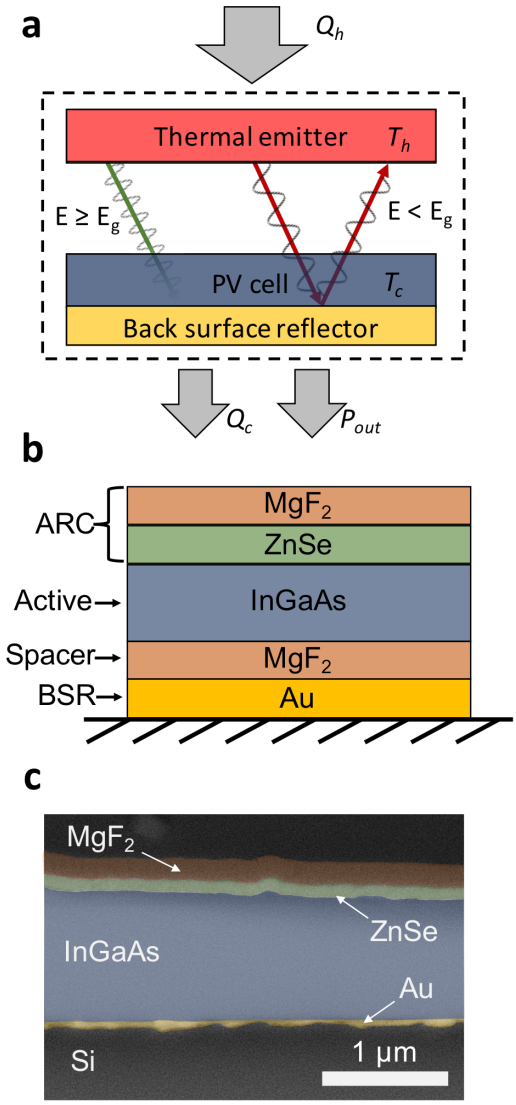

Figure 3.1. Dielectric claddings for improved photon recuperation. (a) Energy flows in a parallel plate TPV system with out-of-band photon recycle. Spectrally selective absorption is achieved in a thin-film cell, decreasing waste heat (Q_c) and net heat transfer between the emitter and cell (Q_h), without decreasing output power (P_{out}). (b) General schematic of the thin-film structures considered here, which include an InGaAs active layer and combinations of the following layers: back surface reflector (BSR), anti-reflection coating (ARC), and dielectric back spacer. (c) Cross-sectional SEM image of an example structure (false-colored). From top to bottom: 190 nm MgF_2 (orange), 110 nm ZnSe (green), 1.3 μm InGaAs (blue), 400 nm Au BSR (yellow), Si handle (gray).

3.3 Fabrication and characterization of thin InGaAs-based structures

In this section, I identify techniques for enhancing the spectral selectivity of fabricated thin films. I also compare the measured reflectance to optical modeling based on the transfer matrix method.[31,32]

3.3.1 InGaAs film growth

InGaAs structures were grown by gas-source molecular beam epitaxy. A 200 nm thick, unintentionally doped InP buffer layer was grown on a 2 inch diameter, Zn doped (100) InP wafer, followed by a 4 nm thick AlAs sacrificial layer, and an unintentionally doped i-InGaAs absorption layer. The wafer was then diced into 6 mm x 6 mm squares using an ADT7100 dicing saw. Samples were rinsed with DI water for 30 seconds to remove dicing residue and stored in acetone to prevent surface contamination. Immediately before further processing, samples are soaked in buffered HF for 1 minute and rinsed in DI water for 10 seconds to remove surface native oxides.

3.3.2 Establishing a baseline using InGaAs on Au BSR

(i) Fabrication

A 1.38 μm thick epitaxial layer of InGaAs on a Au BSR serves as a baseline structure, and is hereafter called *BSR*. To realize this structure, a 200 nm thick Au layer was deposited by electron beam evaporation on the epitaxial InGaAs surface. A 500 μm thick (100) B doped Si wafer was immersed in buffered HF for 1 minute and rinsed in DI water for 10 seconds to remove native oxides. A 5 nm thick Ir adhesion layer and a 200 nm thick Au layer were deposited on the Si wafer. The metalized surfaces of the sample and wafer were cold-weld bonded by applying heat (200°C)

and pressure (5 MPa) for 5 minutes under vacuum (10^{-4} mTorr) using an EVG 520 wafer bonder. The epitaxial layers were lifted off from the parent InP wafer by removing the AlAs layer through immersion in 17% HF at 45°C with 400 rpm agitation by magnetic stir bar for 1.5 hours. Following lift-off, samples were stored at 60°C in Remover PG (MicroChem) to prevent oxide formation on the epitaxial surface prior to further processing.

(ii) Roughness of the back surface

The roughness of the back-surface was qualitatively examined by SEM cross-sectional imaging (Figure 3.2). Examination of the InGaAs-Au interface reveals no discernable surface roughness, suggesting that structural features are smaller than the resolution of the SEM (FEI Nova 200 Nanolab). It is assumed that rough features at this interface are much smaller than the wavelength of maximum radiance for a 1500 K blackbody emitter (1.93 μm) and that back-surface scattering does not contribute significantly to out-of-band attenuation.

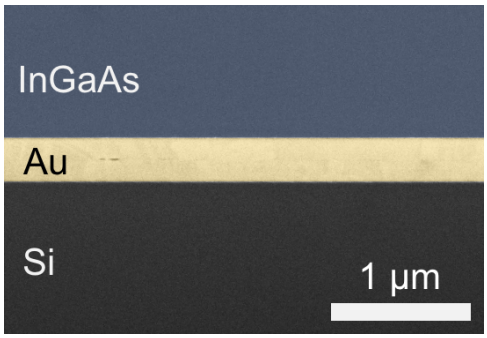

Figure 3.2. Cross-sectional SEM image of the *BSR* structure (false-colored). From top to bottom: 1.38 μm InGaAs (blue), 400 nm Au BSR (yellow), Si handle (gray).

(iii) Spectral characterization

Figure 3.3a depicts the experimental absorptance (a) of the *BSR* structure, as a function of photon energy (E) and incidence angle (θ), as measured by a Fourier transform infrared (FTIR) microscope, alongside the spectral characteristics predicted through optical modeling. The response is characterized by selective absorptance above the bandgap energy and reflectance below. Average weighted optical properties were calculated with respect to the incident power from a 1500 K blackbody emitter. The *BSR* structure exhibits an average absorptance of 61% above the bandgap and 5.5% below the bandgap (94.5% average out-of-band reflectance).

3.3.3 Enhancing absorptance using a bilayer anti-reflection coating

(i) Fabrication

To enhance in-band absorptance, a double layer anti-reflection coating (ARC) (190 nm MgF_2, 110 nm ZnSe) is deposited by electron beam evaporation on a 1.3 μm InGaAs layer with a Au BSR. This structure is hereafter called *ARC*. Following.

(ii) Spectral characterization

Figure 3.3b shows that the spectral properties of the *ARC* structure are characterized by increased absorptance above the bandgap compared to the *BSR* structure and a reduction of peak-to-peak absorptance variations. The *ARC* structure exhibits average absorptance of 81% above the bandgap and 5.3% average absorptance below the bandgap (94.7% average out-of-band reflectance). A parasitic absorptance peak is observed at 0.44 eV, which is attributed to absorption in the double-layer ARC, as confirmed by measurement of the ARC directly on Au (Section 3.3.5).

3.3.4 Enhancing reflectance using a dielectric back spacer

(i) Fabrication

A third structure, hereafter called Spacer, is designed to further enhance out-of-band reflectance. In this structure, a 430 nm thick MgF_2 spacer is deposited between a 2.1 μm thick InGaAs layer and a Au BSR. Following InGaAs film growth, a 200 nm thick Au layer was deposited by electron beam evaporation on the epitaxial InGaAs surface. Similarly, a 5 nm thick Ir adhesion layer and a 200 nm thick Au layer were deposited on a 25 μm thick E-type Kapton foil substrate. The metalized surfaces of the sample and foil were cold-weld bonded by applying heat (200°C) and pressure (5 MPa) for 5 minutes under vacuum (10^{-4} mTorr) using an EVG 520 wafer bonder. The epitaxial layers were lifted off from the parent InP wafer by removing the AlAs layer through immersion in 17% HF at 45°C with 400 rpm agitation by magnetic stir bar for 1.5 hours. Following lift-off by HF etch, MgF_2 was deposited onto the epitaxial InGaAs surface by electron beam evaporation, followed by a 200 nm thick Au layer. A 500 μm thick (100) B doped Si wafer was immersed in buffered HF for 1 minute and rinsed in DI water for 10 seconds to remove native oxides. A 5 nm thick Ir adhesion layer and a 200 nm thick Au layer were deposited on the Si wafer. The metalized surfaces of the sample and Si wafer were cold-weld bonded by applying heat (200°C) and pressure (5 MPa) for 5 minutes under vacuum (10^{-4} mTorr) using an EVG 520 wafer bonder. The Kapton host foil was removed by inductively coupled plasma (ICP) reactive-ion etching (RIE) (Oxford Plasmalab System 100) with 20 sccm of O_2 at a chamber pressure of 6 mTorr, stage temperature of 0°C, ICP power of 500 W, and forward power of 100 W for 25 minutes. The remaining Ir and Au layers were removed using ICP RIE with 12:9:5 sccm of H_2:Cl_2:Ar at a chamber pressure of 10 mTorr, stage temperature of 0°C, ICP power of 500 W, and forward power of 100 W for 2.5 minutes.

(ii) Spectral characterization

The *Spacer* structure exhibits an average out-of-band reflectance of 95.7% (Figure 3.3c), better than either of the previous structures. A parasitic absorptance peak at 0.44 eV, similar to the one observed in the *ARC* structure, partly limits the reflectance. The *Spacer* structure exhibits in-band absorptance of 62.5%, comparable to that of *BSR* structure. Outside of the parasitic peak, the simulated optical response of each of the architectures agrees with its measured response within 9% above the bandgap and 5% below the bandgap.

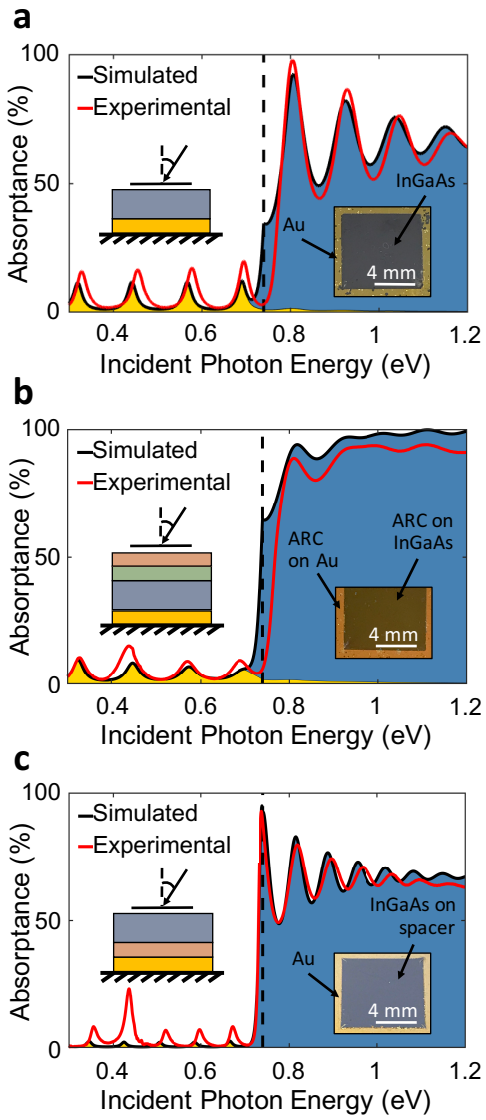

Figure 3.3. Spectral characterization of candidate structures. Simulated (red) and measured (black) optical responses of the (a) *BSR* structure, (b) *ARC* structure, (c) *Spacer* structure. Blue (yellow) shading indicates predicted absorption by the InGaAs (Au) layer. Left inset: Angle of incidence (15°). Right inset: Photograph of sample.

3.3.5 Out-of-band absorption in MgF_2

Out-of-band absorption is observed at ~0.43 eV in the experimentally measured spectral characteristics only for structures containing MgF_2. To confirm that the absorption occurs in the

dielectric layer, specifically, I measured the optical response of the MgF_2/ZnSe bilayer on a Au layer (Figure 3.4) and observed a similar absorptance peak.

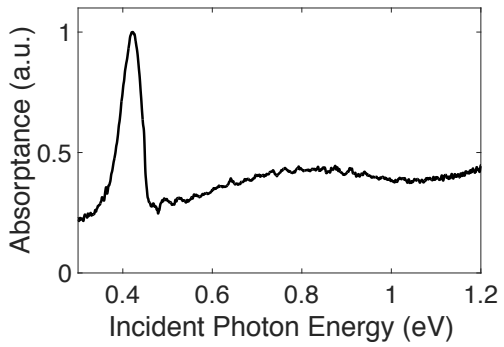

Figure 3.4. Absorptance of MgF_2/ZnSe bilayer ARC on Au BSR.

3.4 Energy conversion simulation

Here I present a prediction of TPV performance based on the spectral properties and geometry of a TPV cell, operating at 20°C, in perfect view of a high-temperature black emitter.

During TPV operation (Figure 3.1a), input heat (Q_h) increases the temperature of the emitter (T_h) and drives thermal emission (Q_{emit}). The photon flux of an emitting blackbody, Φ, as a function of emitted photon energy, E, is calculated via Planck's Law:

$$\Phi(E) = \frac{2\pi E^2}{c^2 h^3 \left(\exp\left(\frac{E}{k_B T}\right) - 1\right)} \tag{3.1}$$

where c is the speed of light, h is Planck's constant, and k_B is the Boltzmann constant. Radiation emitted by the thermal emitter, $\Phi_h(E)$, is described by Planck's Law evaluated at T_h. A portion of incident radiation is absorbed by the PV cell and the rest is reflected (Q_{ref}). Hemispherically-averaged absorptance ($a(E)$) is calculated by integration of the angle-dependent absorption spectrum ($a(E,\theta)$) over angles (θ,ϕ):

$$a(E) = \frac{\int_0^{2\pi} \int_0^{\pi/2} a(E,\theta) \cos(\theta) \sin(\theta) d\theta d\phi}{\int_0^{2\pi} \int_0^{\pi/2} \cos(\theta) \sin(\theta) d\theta d\phi} \tag{3.2}$$

Upon absorption in the InGaAs layer, in-band photons generate excited electron-hole pairs, enabling the generation of electrical power (P_{out}). The maximum short circuit current, is calculated from the angle-averaged optical response, *a(E)*, and the emitted photon flux, $\Phi_h(E)$:

$$J_{SC} = q \int_{E_g}^{\infty} a(E) \Phi_h(E) dE \tag{3.3}$$

where q is the elementary charge of an electron and E_g is the bandgap. The photocurrent, J, as a function of voltage across the cell, V, is the difference between the short circuit current and recombination loss, given by:

$$J(V) = J_{sc} - q\left(R_{rad} + R_{SRH} + R_{Aug}\right) \tag{3.4}$$

where R_{rad}, R_{SRH}, and R_{Aug}, are the radiative, Shockley-Reed-Hall (SRH), and Auger recombination rates, respectively. The radiative recombination rate is:

$$R_{rad} = exp\left(\frac{qV}{k_B T_c}\right) \int_{E_g}^{\infty} a(E) \Phi_c(E) dE \tag{3.5}$$

In the case of low semiconductor doping concentration (N_D), such that the injected carrier concentration (n_o) is greater than N_D, the non-radiative recombination rates are independent of dopant concentration.[33] In this high-injection regime, the non-radiative SRH recombination rate is:

$$R_{SRH} = \frac{L n_i^2}{\tau_{SRH}} exp\left(\frac{qV}{2k_B T_c}\right) \tag{3.6}$$

where L is the thickness of the active region, τ_{SRH} is the SRH recombination lifetime, and n_i is the intrinsic carrier concentration. Literature values of intrinsic carrier concentration and SRH lifetime for InGaAs at 300 K are 6.3x10^{11} cm^{-3} and 47.4 µs, respectively.[34,35] The non-radiative, Auger recombination rate, R_{Aug}, is:

$$R_{Aug} = L\left(C_n + C_p\right) n_i^3 exp\left(\frac{3qV}{2k_B T_c}\right) \tag{3.7}$$

where C_n and C_p are the Auger recombination coefficients for recombination involving two electrons and two holes, respectively. The Auger recombination coefficients are $C_n = C_p = 8.1\text{x}10^{-29}$ cm^{-3}.[35]

The output power of the cell is the product of the photocurrent and the voltage:

$$P_{out} = J(V) \cdot V \tag{3.8}$$

Efficiency is calculated from the maximum power point voltage, V_{MPP}, and current response, J_{MPP} via:

$$\eta_{TPV} = \frac{P_{out}}{Q_h} = \frac{P_{out}}{Q_{emit} - Q_{ref}} = \frac{J_{MPP} \cdot V_{MPP}}{\int_0^\infty E \cdot \Phi_h(E) dE - \int_0^\infty (1 - a(E)) \cdot E \cdot \Phi_h(E) dE} \tag{3.9}$$

3.5 Evaluating strategies for enhanced selectivity

In this section, I use the TPV performance model described in section 3.4 to evaluate the spectral selectivity of the three cases (*BSR*, *ARC*, and *Spacer*). Optimized structures were rigorously determined for each of the InGaAs cases by allowing layer thicknesses to vary in order to maximize predicted conversion efficiency (Table 3.1). The hemispherically averaged optical response of the optimized *BSR*, *ARC*, and *Spacer* structures are depicted in Figure 3.5. The performance of the optimized structures (Table 3.1) is compared with an InGaAs cell without a BSR (hereafter called *Blackbody*), characterized by no spectral selectivity (i.e., $\bar{a}(E \geq E_g) = \bar{a}(E < E_g) = 100\%$). I set the thickness of the InGaAs layer in the *Blackbody* case to twice that of the *BSR* case, such that the optical path lengths through InGaAs are approximately equal in each case (assuming wavevectors within the active layer are near-normal because of the high refractive index of InGaAs relative to vacuum).[6,11]

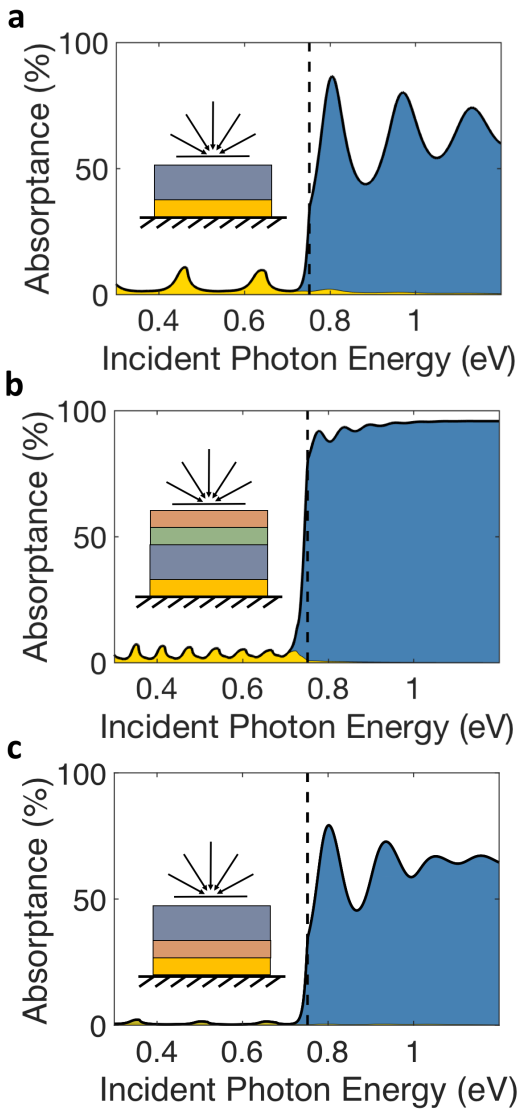

Figure 3.5. Predicted, hemispherically averaged absorptance of optimized structures. (a) *BSR* structure. (b) *ARC* structure. (c) *Spacer* structure. Blue (yellow) shading indicates predicted absorption by the InGaAs (Au) layer. Inset: diffuse incidence on structure.

3.5.1 Enhanced out-of-band reflectance

A significant enhancement in efficiency, relative to the blackbody case, is predicted for cells with a reflective back surface, suggesting it is an essential feature for achieving high efficiency. For example, the *BSR* case is predicted to achieve 43% efficiency when paired with a 1500 K emitter, whereas the *Blackbody* case achieves only 8% efficiency under these conditions (Table 3.1). Use

of a MgF_2 back spacer increases this efficiency gain further. The *Spacer* case is predicted to exhibit 8% greater absolute efficiency than the *BSR* case because of its higher out-of-band reflectance (98.9% vs. 96.8%).

3.5.2 Enhanced in-band absorptance

An anti-reflection coating, on the other hand, is less important for improving efficiency. However, an ARC considerably improves the in-band absorptance and, consequently, the power density. For example, the *ARC* case exhibits ~0.8 W/cm^2 higher power density than either the *BSR* or the *Spacer* case.

3.5.3 Optimized structure for enhanced out-of-band reflectance and in-band absorptance

To optimize the overall cell architecture, I modeled a third design, which includes an ARC and a spacer (Figure 3.6a inset), hereafter called the *Combined* case. The optimized *Combined* case exhibits the best spectral selectivity (Figure 3.6a), achieving higher in-band absorptance than the *Spacer* case without significantly compromising out-of-band reflectance (Table 3.1). Because of its superior optical properties, the *Combined* case is predicted to operate with higher efficiency than either the *BSR* or *Spacer* case (Figure 3.6b) and with a power output approaching that of the *ARC* case (Figure 3.6c). Specifically, for an optimized *Combined* cell, I predict an efficiency of 52% and a power output of 2.1 W/cm^2 when paired with a 1500 K black emitter.

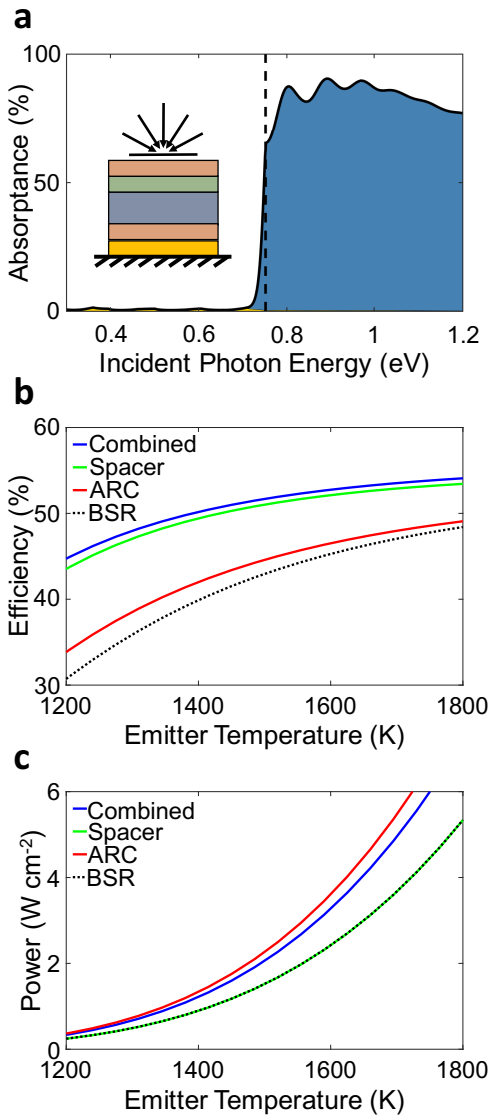

Figure 3.6 Optimization results and predicted performance (a) Calculated, hemispherically-averaged optical response of the *Combined* structure. Blue and yellow shading indicates specific absorption by the InGaAs and Au layer, respectively. Inset: Structure schematic. Comparison of predicted (b) efficiency, (c) power output for each case, optimized given its discrete set of layers.

Table 3.1. Optimized architecture and performance for candidate structures (T_h = 1500 K).

	MgF_2 [μm]	ZnSe [μm]	InGaAs [μm]	MgF_2 [μm]	Back surface	$\bar{a}(E \geq E_g)$ [%]	$\bar{a}(E < E_g)$ [%]	η [%]	P_{out} [W cm^{-2}]
BSR	-	-	0.97	-	Au	60.8	3.2	42.9	1.52
ARC	0.20	0.10	2.78	-	Au	92.2	3.7	44.6	2.27
Spacer	-	-	1.1	0.44	Au	61.1	1.1	51.0	1.52
Combined	0.46	0.15	1.46	0.42	Au	82.3	1.4	51.7	2.07
Blackbody	*	*	1.93	-	Black	100	100	8.1	2.32

*The hypothetical *Blackbody* case is assumed to have perfect broadband absorptance.

3.6 Discussion

The presented simulation results suggest that dielectric spacers are an important feature of high-efficiency thin-film InGaAs cells. Spacers limit parasitic absorption at the metal contact by reducing the intensity of radiation that reaches the back interface. Provided that parasitic absorption is mitigated in the active layers, average out-of-band reflectance approaching 99% may be achieved with the use of a back spacer. Development of a TPV device with a back spacer will require the design of electrical contacts capable of collecting charge carriers laterally or across this dielectric region. Prior demonstration of a TPV device with dielectric claddings (ARC and spacer) utilized monolithic series interconnections to electrically contact the active region.[29] Similar design elements may be appropriate for developing TPV modules with the proposed MgF_2 spacer.

This study identified that the optimal InGaAs thickness depends on the cell architecture. Thinner active layers (1-1.5 μm) are optimal when using back spacers, which is further desirable for

reducing materials and processing costs. The optimum thickness is observed in this range because ultra-thin cells (<300 nm) suffer from low photo-generation while thicker devices exhibit increased rates of non-radiative recombination and higher parasitic out-of-band absorption.

3.7 Conclusions

In summary, this work demonstrates high spectral selectivity in thin-film structures by using back surface reflectors and by optimizing interference. Specifically, thin-film structures are experimentally observed to exhibit record high average out-of-band reflectance (96%). Reflective back surfaces are shown through simulation to be the most important feature for high efficiency cells. TPV performance modeling shows how enhanced reflectance due to a dielectric spacer layer, between the InGaAs and the Au back contact, may enable TPV efficiencies above 50% for a 1500 K black emitter. When combined with a double-layer anti-reflection coating, high power densities (~2 W/cm^2) are also achievable. The potential for a dramatic increase of conversion efficiency through improved spectral selectivity, combined with the potential for reduced module costs through wafer reuse, supports the prospect of thin-film TPVs for applications in distributed power generation. Beyond the high spectral selectivity demonstrated here, development of high-performance thin-film TPV systems will require precise doping of active materials and design of selective electrical contacts with low parasitic absorption.

3.8 References

1. Durisch, W., and Bitnar, B. (2010). Novel thin film thermophotovoltaic system. Sol. Energy Mater. Sol. Cells *94*, 960–965.
2. Seyf, H.R., and Henry, A. (2016). Thermophotovoltaics: a potential pathway to high efficiency concentrated solar power. Energy Environ. Sci. Energy Environ. Sci *9*, 2654–2665.
3. Bitnar, B. (2003). Silicon, germanium and silicon/germanium photocells for thermophotovoltaics applications. Semicond. Sci. Technol. *18*, S221.
4. Siergiej, R.R., Wernsman, B., Derry, S.A., Mahorter, R.G., Wehrer, R.J., Link, S.D., Palmisiano, M.N., Messhan, R.L., Murray, S., Murray, C.S., et al. (2003). 20% Efficient InGaAs/InPAs Thermophotovoltaic Cells. AIP Conf. Proc. *653*, 414–423.
5. Wernsman, B., Siergiej, R.R., Link, S.D., Mahorter, R.G., Palmisiano, M.N., Wehrer, R.J., Schultz, R.W., Schmuck, G.P., Messham, R.L., Murray, S., et al. (2004). Greater Than 20% Radiant Heat Conversion Efficiency of a Thermophotovoltaic Radiator/Module System Using Reflective Spectral Control. IEEE Trans. Electron Devices *51*, 512–515.
6. Ganapati, V., Xiao, T.P., and Yablonovitch, E. (2018). Ultra-Efficient Thermophotovoltaics Exploiting Spectral Filtering by the Photovoltaic Band-Edge arXiv : 1611 . 03544v2 [physics . optics] 7 Feb 2018. 1–14.
7. Lenert, A., Nam, Y., Bierman, D.M., and Wang, E.N. (2014). Role of spectral non-idealities in the design of solar thermophotovoltaics. Opt. Express *22*, A1604.
8. Miller, O.D., Yablonovitch, E., and Kurtz, S.R. (2012). Strong Internal and External Luminescence as Solar Cells Approach the Shockley–Queisser Limit. IEEE J. Photovoltaics *2*, 303–311.
9. Swanson, R.M. (1978). Silicon photovoltaic cells in thermophotovoltaic energy conversion. In 1978 International Electron Devices Meeting (IRE), pp. 70–73.
10. Coutts, T.J. (2001). Overview of thermophotovoltaic generation of electricity. Sol. Energy Mater. Sol. Cells *66*, 443–452.
11. Jurczak, P., Onno, A., Sablon, K., and Liu, H. (2015). Efficiency of GaInAs thermophotovoltaic cells: the effects of incident radiation, light trapping and recombinations. Opt. Express *23*, A1208.
12. Lee, K., Zimmerman, J.D., Hughes, T.W., and Forrest, S.R. (2014). Non-Destructive Wafer Recycling for Low-Cost Thin-Film Flexible Optoelectronics. Adv. Funct. Mater. *24*, 4284–4291.
13. Lee, K., Lee, J., Mazor, B.A., and Forrest, S.R. (2015). Transforming the cost of solar-to-electrical energy conversion: Integrating thin-film GaAs solar cells with non-tracking mini-concentrators. Light Sci. Appl. *4*, e288–e288.
14. Fourspring, P.M., DePoy, D.M., Rahmlow Jr., T.D., Lazo-Wasem, J.E., and Gratrix, E.J. (2006). Optical coatings for thermophotovoltaic spectral control. Appl. Opt. *45*, 1356.
15. Lenert, A., Bierman, D.M., Nam, Y., Chan, W.R., Celanović, I., Soljačić, M., and Wang, E.N. (2014). A nanophotonic solar thermophotovoltaic device. Nat. Nanotechnol. *9*, 126–130.
16. Shimizu, M., Kohiyama, A., and Yugami, H. (2015). High-efficiency solar-thermophotovoltaic system equipped with a monolithic planar selective absorber/emitter. J. Photonics Energy *5*, 053099.
17. Arpin, K.A., Losego, M.D., and Braun, P. V. (2011). Electrodeposited 3D Tungsten

Photonic Crystals with Enhanced Thermal Stability. Chem. Mater. *23*, 4783–4788.
18. Bierman, D.M., Lenert, A., Chan, W.R., Bhatia, B., Celanović, I., Soljačić, M., and Wang, E.N. (2016). Enhanced photovoltaic energy conversion using thermally based spectral shaping. Nat. Energy *1*, 16068.
19. Chan, W.R., Bermel, P., Pilawa-Podgurski, R.C.N., Marton, C.H., Jensen, K.F., Senkevich, J.J., Joannopoulos, J.D., Soljacic, M., and Celanovic, I. (2013). Toward high-energy-density, high-efficiency, and moderate-temperature chip-scale thermophotovoltaics. Proc. Natl. Acad. Sci. U. S. A. *110*, 5309–14.
20. Nam, Y., Yeng, Y.X., Lenert, A., Bermel, P., Celanovic, I., Soljačić, M., and Wang, E.N. (2014). Solar thermophotovoltaic energy conversion systems with two-dimensional tantalum photonic crystal absorbers and emitters. Sol. Energy Mater. Sol. Cells *122*, 287–296.
21. Chou, J.B., Yeng, Y.X., Lee, Y.E., Lenert, A., Rinnerbauer, V., Celanovic, I., Soljačić, M., Fang, N.X., Wang, E.N., and Kim, S.-G. (2014). Enabling Ideal Selective Solar Absorption with 2D Metallic Dielectric Photonic Crystals. Adv. Mater. *26*, 8041–8045.
22. Chou, J.B., Yeng, Y.X., Lenert, A., Rinnerbauer, V., Celanovic, I., Soljačić, M., Wang, E.N., and Kim, S.-G. (2014). Design of wide-angle selective absorbers/emitters with dielectric filled metallic photonic crystals for energy applications. Opt. Express *22*, A144.
23. Rinnerbauer, V., Lenert, A., Bierman, D.M., Yeng, Y.X., Chan, W.R., Geil, R.D., Senkevich, J.J., Joannopoulos, J.D., Wang, E.N., Soljačič, M., et al. (2014). Metallic photonic crystal absorber-emitter for efficient spectral control in high-temperature solar thermophotovoltaics. Adv. Energy Mater. *4*, 1400334.
24. Shimizu, M., Kohiyama, A., and Yugami, H. (2018). Evaluation of thermal stability in spectrally selective few-layer metallo-dielectric structures for solar thermophotovoltaics. J. Quant. Spectrosc. Radiat. Transf. *212*, 45–49.
25. Yeng, Y.X., Ghebrebrhan, M., Bermel, P., Chan, W.R., Joannopoulos, J.D., Soljacic, M., and Celanovic, I. (2012). Enabling high-temperature nanophotonics for energy applications. Proc. Natl. Acad. Sci. *109*, 2280–2285.
26. Rinnerbauer, V., Yeng, Y.X., Chan, W.R., Senkevich, J.J., Joannopoulos, J.D., Soljačić, M., and Celanovic, I. (2013). High-temperature stability and selective thermal emission of polycrystalline tantalum photonic crystals. Opt. Express *21*, 11482.
27. Swanson, R.M. (1980). Recent developments in thermophotovoltaic conversion. In 1980 International Electron Devices Meeting (IRE), pp. 186–189.
28. Clevenger, M.B., Murray, C.S., Ringel, S.A., Sacks, R.N., Qin, L., Charache, G.W., and Depoy, D.M. (1999). Optical properties of thin semiconductor device structures with reflective back-surface layers. Fourth NREL Conf. thermophotovoltaic Gener. Electr., 327–334.
29. Wang, C. a, Shiau, D. a, Murphy, P.G., O'Brien, P.W., Huang, R.K., Connors, M.K., Anderson, a C., Donetsky, D., Anikeev, S., Belenky, G., et al. (2004). Wafer bonding and epitaxial transfer of GaSb-based epitaxy to GaAs for monolithic interconnection of thermophotovoltaic devices. J. Electron. Mater. *33*, 213–217.
30. Wu, X., Duda, A., Carapella, J.J., Ward, J.S., Webb, J.D., and Wanlass, M.W. (1999). A Study of Contacts and Back-Surface Reflectors Interconnected Modules. *517*.
31. Born, M., and Wolf, E. (1970). Principles of Optics 4th ed. (Perfamon Press Ltd.).
32. Deng, X.-H., Liu, J.-T., Yuan, J.-R., Liao, Q.-H., and Liu, N.-H. (2015). A new transfer matrix method to calculate the optical absorption of graphene at any position in stratified

media. Europhys. Lett. *109*, 27002.
33. Krier, A. (2006). Mid-infrared Semiconductor Optoelectronics (Springer).
34. Electrical Properties of Gallium Indium Arsenide (GaInAs) http://www.ioffe.ru/SVA/NSM/Semicond/GaInAs/ebasic.html.
35. Ahrenkiel, R.K., Ellingson, R., Johnston, S., and Wanlass, M. (1998). Recombination lifetime of In0.53Ga0.47As as a function of doping density. Appl. Phys. Lett. *72*, 3470–3472.

Chapter 4: Nearly Perfect Photon Utilization in an Air-Bridge Thermophotovoltaic Cell

4.1 Motivation

Current methods for photon recuperation in TPVs are limited by insufficient bandwidth or parasitic absorption, resulting in large efficiency losses relative to theoretical limits. For example, Swanson reported[1] the development of a Si TPV cell with a SiO_2/Ag BSR that enabled 95% out-of-band reflectance and a power conversion efficiency of 29% using a 2300 K broadband emitter. More recently, Omair, *et al*. reported[2] a thin-film $In_{0.53}Ga_{0.47}As$ cell with a Au BSR exhibiting 29.1% efficiency and 94.6% out-of-band reflectance, paired with a 1480 K graphite emitter. This work represents the highest reported efficiency for any TPV to date. Nevertheless, these demonstrations have yet to exceed 95% out-of-band suppression. At this level, the largest losses relative to theoretical limits are due to spectral inefficiencies.[3] 5% out-of-band reflectance loss, although seemingly small, lowers TPV efficiency by ~10% absolute due to the high fraction of low-energy photons.

As discussed in Chapter 3, my co-authors and I recently developed an InGaAs-on-dielectric thin-film structure that exhibited a record-high out-of-band reflectance approaching 96%[4]. The

reflectance of this structure, however, fell short of simulation by ~3% due to absorption losses from residual H_2O in the dielectric spacer adjacent to the Au BSR.

This chapter presents an alternative approach in which the dielectric spacer within the thin-film cell is replaced with air. This approach eliminates parasitic absorption in the dielectric, maximizes the refractive index mismatch at each interface, and simplifies the fabrication process relative to prior work using conventional dielectric spacers.[4] The so-called air-bridge $In_{0.53}Ga_{0.47}As$ (InGaAs) TPV cell absorbs most of the in-band radiation to generate electricity while serving as a nearly perfect mirror with nearly 99% out-of-band reflectance. This result represents a four-fold reduction in parasitic absorption relative to existing TPV cells. The resulting gain in absolute efficiency exceeds 6%, leading to a record-high power conversion efficiency exceeding 30%, as measured with a ~1455K SiC emitter.

Beyond improvements to the absolute efficiency, the air-bridge architecture serves to ease the dependence of power conversion efficiency on cell bandgap E_g and emitter temperature T_h. While a trade-off between bandgap and photocurrent exists for conventional devices with <95% out-of-band reflectance,[5] the spectral efficiency becomes much less sensitive to increased bandgap or decreased heat source temperature as out-of-band reflectance increases. This characteristic may potentially allow for the exploitation of low-cost semiconductors (i.e., Si) or translation to low-temperature applications, such as concentrated solar power and waste heat scavenging, that have heretofore been impractical for TPV systems.

The present work is the result of a highly collaborative effort between members of my own research group, led by Andrej Lenert, and that of Prof. Stephen R. Forrest. I would specifically like to highlight the contributions of my co-first author, Dejiu Fan. Dejiu developed the novel fabrication protocol that enabled experimental realization of the air-bridge cell concept. Further, he performed molecular beam epitaxial growth of the heterostructure absorber and aided in efficiency characterization. This work would not have been possible without his efforts.

4.2 Advantages of the air-bridge architecture

The benefits of an air-bridge architecture are apparent from a theoretical comparison of energy flows and losses in a TPV utilizing a conventional thin-film Au BSR and an air-bridge cell. In Figure 4.1a, a hot thermal source radiates photons with a broad, blackbody spectrum. Photons with energy (E) greater than the TPV semiconductor bandgap (E_g) are absorbed and generate current, while photons with $E < E_g$ travel through the cell, are reflected by the BSR, and re-absorbed by the emitter. Conventional reflectors such as Au introduce a loss of ~5% at the semiconductor/Au interface for every reflection/re-absorption cycle. In contrast, when an air cavity is integrated within the cell, Figure 4.1b, photons with $E < E_g$ experience lossless Fresnel reflection at the TPV/air interface. Photons that transmit through this interface are then reflected by the Au with very low loss at the air/Au interface. When integrated over the emitter spectrum and angles of incidence up to 30°, out-of-band absorption by the conventional Au BSR cell is 4.7%, representing the primary source of loss, see Figure 4.1c. Other loss pathways include imperfect carrier collection (~2.5%). The absorption oscillations are Fabry-Perot modes formed in the cavity between the reflector and the front surface of the cell. In comparison, the air-bridge cell loses only 1.1% of power to out-of-band absorption, see Figure 4.1d. From these calculations, both cells have

a similar energy transfer efficiency in the in-band ($E>E_g$) region (61.1% for Au BSR vs. 61.8% for air-bridge), whereas the air-bridge structure effectively reduces the out-of-band losses by more than 4 times compared to the conventional cell.

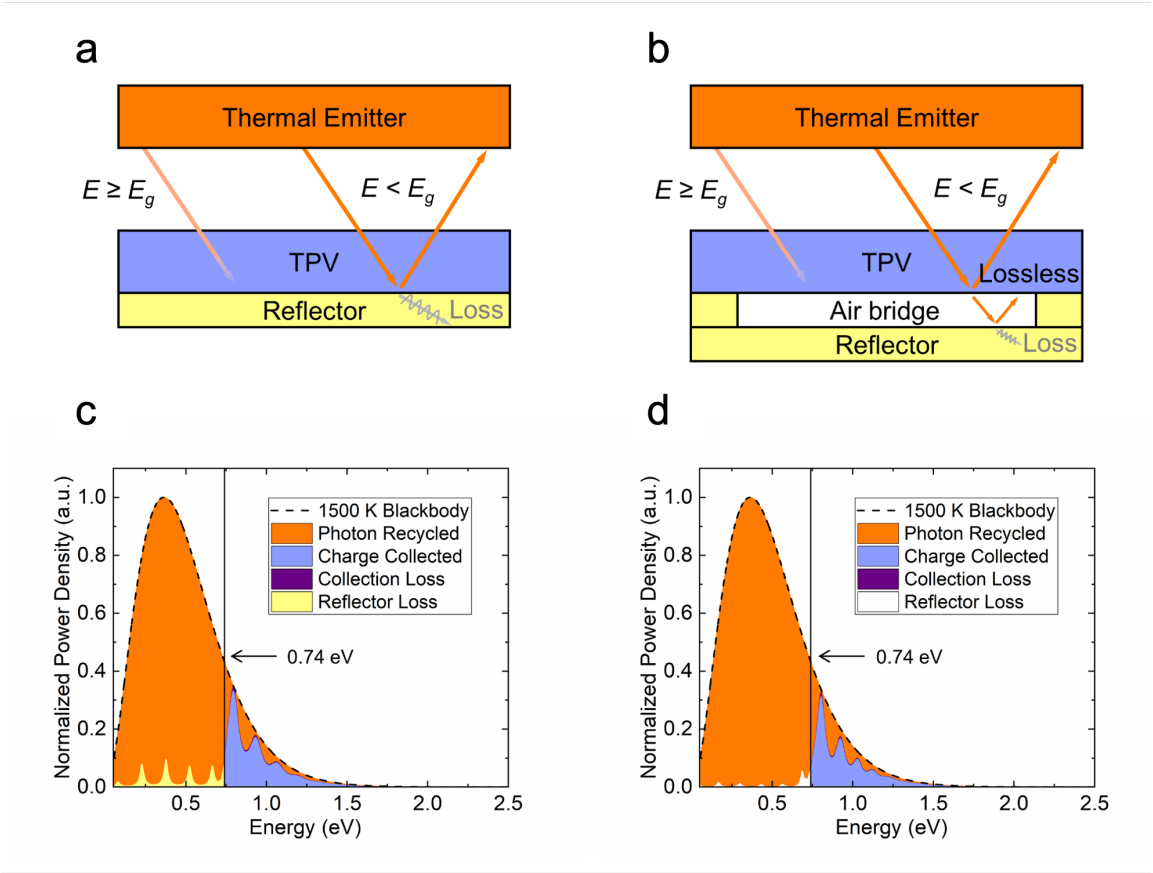

Figure 4.1. Photon utilization in air-bridge thermophotovoltaics. Conceptual schematics of energy flow in (a) a conventional thin-film TPV with Au back surface reflector (BSR) versus (b) a thin-film TPV with air-bridge reflector. (c) Power distribution of a conventional thin-film InGaAs cell (E_g = 0.74 eV) with a Au BSR operated with a 1500 K blackbody source. The dashed line shows the normalized power density of the blackbody, and the cell absorption spectrum is calculated using transfer matrix methods[6]. (d) Power distribution of the air-bridge TPV shown in Figure 4.1b operated using a 1500 K blackbody emitter.

4.3 Device fabrication

Figures 4.2a to 4.2d illustrate key steps in fabricating the air-bridge cell, as described in detail in section 4.3.2. The fabrication procedure provides two significant advantages. First, the air cavity

thickness can be accurately controlled within nanometers by the thickness of buried Au grid lines. Second, all the air cavities are encapsulated through Au-Au cold-weld bonding. This protects the TPV bottom surface from damage by the HCl substrate etchant. Lastly, as the bottom and top grid lines are aligned, normally incident photons encounter only the TPV/air interface when they penetrate the device active layers.

4.3.1 Material growth

A lattice-matched, inverted *P-n-N* heterostructure TPV cell is epitaxially grown on a 350 μm thick (100) InP substrate using GENxplore Molecular Beam Epitaxy (Veeco Corp., MN, 55127). The heterostructure comprises a 200 nm undoped InP buffer layer, 200 nm Be-doped (1×10^{18} cm^{-3}) $In_{0.53}Ga_{0.47}As$ (InGaAs) contact layer, 200 nm Be-doped (1×10^{18} cm^{-3}) InP front window layer, 1 μm nm Si-doped (1×10^{17} cm-3) InGaAs absorption layer, 100 nm Si-doped (1×10^{18} cm^{-3}) InP back window layer, and 100 nm Si-doped (1×10^{18} cm^{-3}) InGaAs contact layer.

4.3.2 Fabrication protocol

The native oxide on the epitaxial surface is removed in buffered HF for 90 s and rinsed in de-ionized (DI) water for 10 s. All layers are photolithographically patterned using LOR 3A (MicroChem Corp., MA, 01581) and SPR 220 3.0 (MicroChem Corp., MA, 01581) bilayer photoresist. Cathode contacts (10 nm Ti/ 590 nm Au, E-beam evaporated) are patterned first with 2.95/2.85 mm outer/inner diameter ring contact filled with 8 μm wide metal grids. The grid-to-grid spacing is 80 μm, giving an ~10 % grid coverage (i.e. a 90 % geometric fill factor). The sample is then soaked in H_3PO_4: H_2O_2:H_2O = 1:1:8 solution for 20 s to remove the 100 nm n-type InGaAs contact layer, while the contact layer underneath the cathode contact metal is protected to

minimize the contact resistance. The sample is bonded to a Si substrate coated with 5 nm Ti/ 300 nm Au (E-beam evaporated) by applying heat (150 °C) and pressure (10 MPa) for 5 min using an EVG 510 wafer bonder (EV Group Inc., NY, 12203). Next, the InP substrate is removed by immersion in dilute HCl ($HCl:H_2O$ = 1:1) for 16 hr, leaving only the active TPV epitaxial layers suspended over air bridges, and supported by the buried grid lines. This destructive substrate removal step can be substituted by non-destructive epitaxial lift-off (ND-ELO)[7,8] to recycle the costly InP growth substrate. The TPV mesa (3 mm diameter) is subsequently patterned by alternatively soaking the sample in InGaAs etchant (citric acid: H_2O_2 = 4:1) and InP etchant ($HCl:H_2O$ = 1:1). Finally, the top anode contact (10 nm Ti/ 30 nm Pt/ 500 nm Au, E-beam evaporated) that is coincident with the buried cathode contact is patterned, and the 200 nm p-type InGaAs contact layer is removed using citric acid: H_2O_2 = 4:1 for 2 min.

4.3.3 Imaging the air-bridge cell

Figure 4.2e is an image of the air-bridge TPV cell. The 3 mm diameter device is covered with multiple 8-μm grid lines to achieve a 90% aperture ratio. The air-bridge cell has been cleaved perpendicular to the grid lines to reveal its cross-section, see Figure 4.2f and 4.2g. The 0.6 μm high × 72 μm wide air cavity in Figure 4.2f is uniform along the entire span between two supporting grid lines with no apparent bowing (< 0.1%).

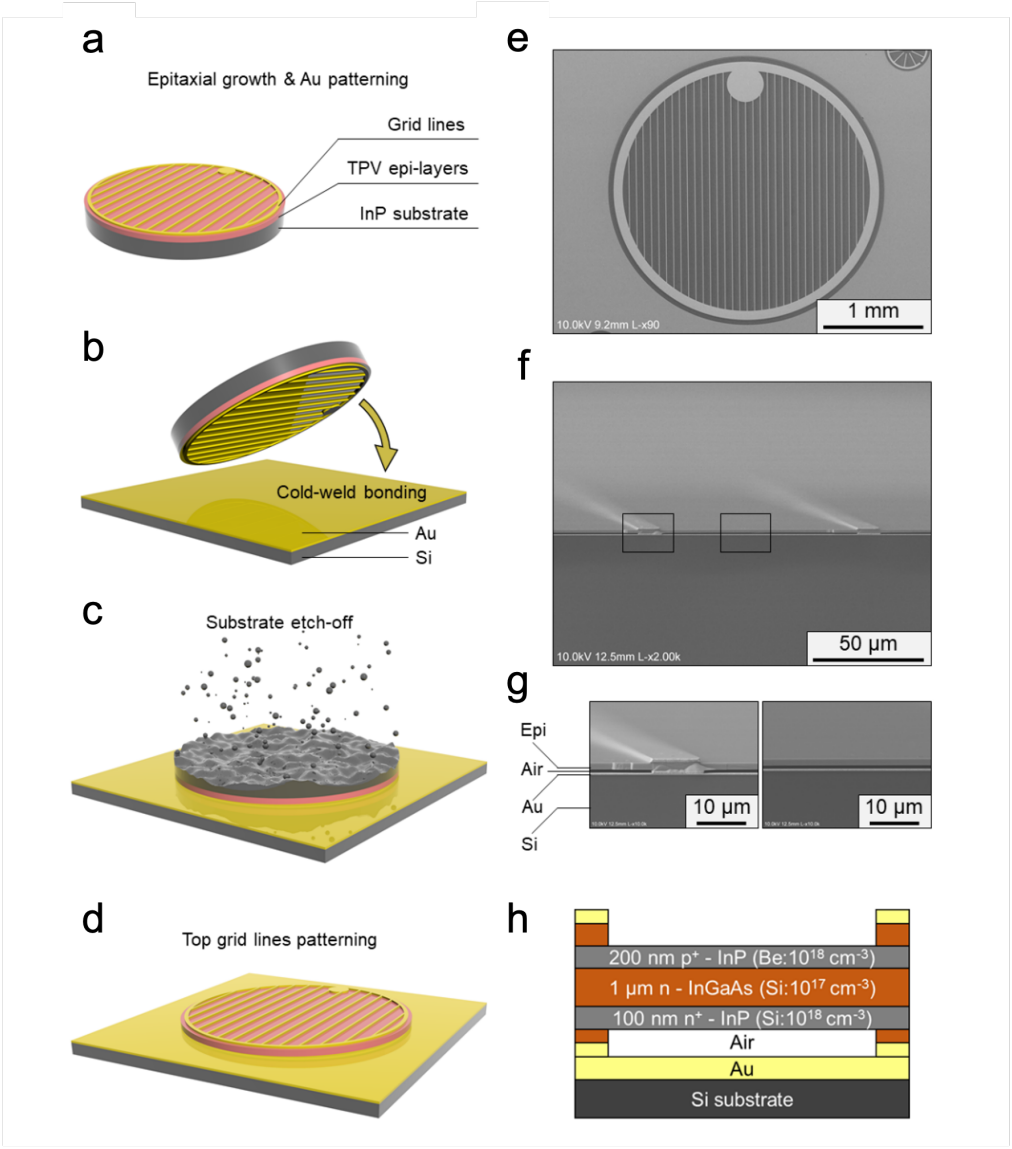

Figure 4.2. Air-bridge TPV cell fabrication. (a) TPV active layers growth and cathode grid line patterning. (b) Cold-weld bonding to a Si substrate coated with Au, (c) substrate removal via etching in HCl, and (d) top anode grid line patterning. (e) Top view scanning electron microscope (SEM) image of the air-bridge cell. (f) Cross section SEM image of the air-bridge cell taken after InP substrate removal and top anode grid patterning, and (g) high magnification images of black boxes in Figure 4.2f. (h) Schematic of the air-bridge cell active layers.

4.4 Spectral characterization

4.4.1 Cell emissivity characterization

The absorption spectra of the air-bridge cell and the Au BSR cell are measured using Spectrum GX Fourier transform infrared (FT-IR) microscope that captures angles of incidence up to 30° (as specified by Perkin-Elmer, MA, 02451). The measurements were done in the near-IR spectral region (12000 cm^{-1} to 1800 cm^{-1}) with a 0.3 mm × 0.3 mm aperture using a CaF_2 beam splitter and a liquid nitrogen cooled InSb detector. Average values are based on measurements taken from 7 different positions on the samples. Out of the measurement range, simulated absorption spectra averaged over incidence angles from 0 to 30° were obtained via transfer matrix methods[6].

As weighted by a 1455 K blackbody emission spectrum, the average out-of-band power reflectance is 95.3% for the Au BSR cell, and 98.5% for the air-bridge cell, see Figure 4.3a. The average in-band power absorption is 63.6% and 61.2% for the Au BSR and the air-bridge cells, respectively, see Figure 4.3b. This is consistent with the simulated absorption in Figure 4.1.

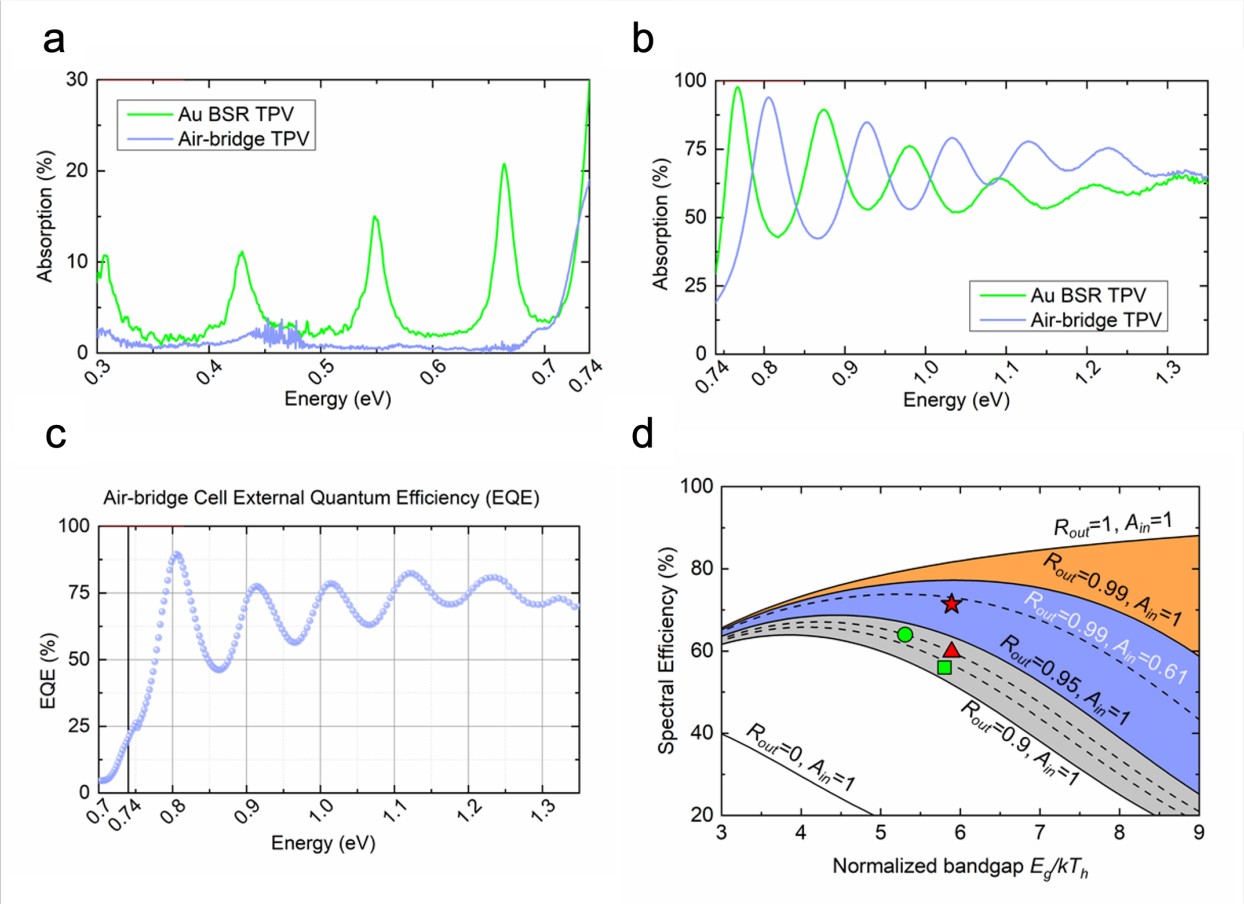

Figure 4.3. Spectral properties of the Au BSR and the air-bridge cell. (a) Out-of-band ($E < E_g$ = 0.74 eV) and (b) In-band (IB, $E \geq E_g$) absorption spectra of Au BSR (green) and air-bridge TPVs (blue). (c) Measured external quantum efficiency (*EQE*) of the air-bridge TPV at 15° light incidence. The interference patterns match those in the measured absorption spectrum in Figure 4.3b. (d) Measured spectral efficiency of the Au BSR (triangle) and air-bridge cells (star). Also shown are prior results from literatures (circle[9] and square[2]). The simulated spectral efficiencies are calculated for various out-of-band reflectance (R_{out}) and in-band absorptions (A_{in}) shown by the solid and dashed curves.

4.4.2 Emitter emissivity characterization

Figure 4.4a shows the experimental setup used to measure the spectral properties of the emitter. The emission spectra of the SiC globar (Part Number: SLS203L, Thorlabs, NJ, 07860) is calibrated by referencing to a true blackbody source. Emission from the true blackbody source is measured by collimating and redirecting emitted light using an off-axis parabolic mirror (OAP) to the external source port of a Nicolet iS50 FT-IR spectrometer. This measurement serves as a baseline

that captures the system response, including environmental absorption and non-idealities in the detector. Next, the off-axis parabolic mirror is rotated 180° to measure emission from the SiC globar. The spectrum is compared with that of the blackbody spectrum to yield the globar emissivity, as shown in Figure 4.4b. Manufacturer specifications of the true blackbody source (Part Number: IR-564, Infrared Systems Development Corp., FL 32792) give the emissivity of the calibrated blackbody of > 0.99. CO_2 and H_2O absorption in spectral ranges 1300-2000 cm^{-1} and 3600-4000 cm^{-1} is removed by linear interpolation between unaffected data beyond these wavelength ranges. The average measured emitter emissivity $\varepsilon_e = 0.96$ is consistent with previous reports for SiC emitters[10].

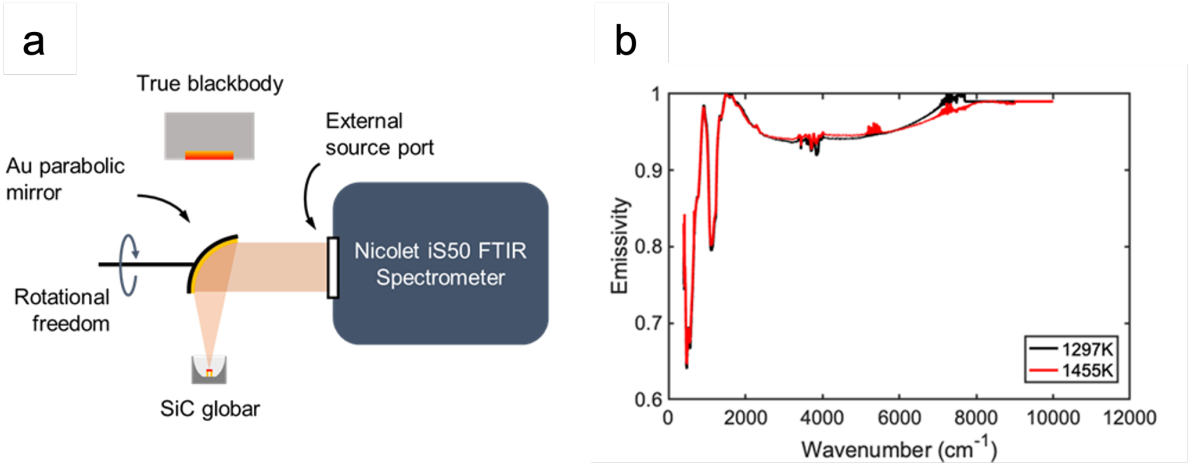

Figure 4.4. Emissivity characterization (a) Schematic of the emitter emissivity calibration setup. (b) Calibrated SiC globar emissivity at 1455 K and 1297 K, indicating that the emissivity is stable within the measured temperature range.

4.4.3 EQE characterization

External quantum efficiency in Figure 4.3c is measured using monochromatic illumination chopped at 200Hz and coupled into a multimode SMA to bare fiber optic patch cable (Part Number: M118L02, Thorlabs, NJ, 07860) oriented 15° to the TPV cell. The output signal is

collected by a SR830 lock-in amplifier. The light illumination power is calibrated using a reference 818-UV/DB Si detector (Newport, CA, 92606) from 400 to 900 nm, a reference 818-IG InGaAs detector (Newport, CA, 92606) from 900 to 1650 nm, and a reference FDG03 Ge detector (Thorlabs, NJ, 07860) from 1650 to 1800 nm.

Figure 4.3c presents the measured in-band external quantum efficiency spectrum (*EQE*) for the air-bridge TPV cell. An average *IQE* = 98.4% is calculated for the air-bridge cell from the measured absorption and *EQE*.

4.4.4 Spectral efficiency improvements

The spectral enhancements of the air-bridge architecture are accurately described by the spectral efficiency, *SE*, which is a key factor of overall TPV efficiency that describes the combined effects of the enhancement of in-band and suppression of out-of-band radiative transport.[5] The Au BSR and the air-bridge TPV cells exhibit *SE* = 59.8% and 71.4%, respectively, as denoted by triangular and star shaped makers in Figure 4.3d. The dashed curve through the top red star represents theoretical *SE* with an average in-band absorption of A_{in}= 0.61 and out-of-band reflectance of R_{out} = 0.99**.** Previous results of Wernsman, *et al*.[9] (circle) and Omair, *et al*.[2] (square) are shown for comparison, along with the theoretical *SE* for A_{in}= 1 and various R_{out}**.** Within the common range of source temperatures, out-of-band loss dominates with increasing bandgap. However, when R_{out} approaches unity (orange region), this dependence vanishes. Thus, the nearly perfect reflectance of the air-bridge design may allow low-cost, wider bandgap materials like Si to be considered as TPV cells while maintaining a high *SE* at relatively low emitter temperatures (< 2000 K). I note, however, that achieving such high spectral performance may be challenging with complicating

factors such as the use of an indirect bandgap semiconductor, and thin film material quality. Electrical properties also need to be carefully engineered to achieve high power conversion efficiencies.

4.5 Efficiency characterization

The figure of merit used to evaluate cells here is power conversion efficiency (*PCE*), defined by:

$$PCE = \frac{P_{electrical}}{P_{incident} - P_{reflected}} \tag{4.1}$$

where $P_{electrical}$ is the electrical power generated, $P_{incident}$ is the incident power, and $P_{reflected}$ is the power reflected by the cell.[2,9,10] Here, $P_{electrical} = V_{oc} \cdot I_{sc} \cdot FF$, where V_{oc} is the open-circuit voltage, I_{sc} is short-circuit current, and FF is the fill factor. Note that the *PCE* represents the heat-input-to-power-output efficiency in an idealized TPV enclosure assuming the cavity has no inactive areas, the cell reflectance is specular, and the medium separating the emitter and cell is non-dissipating. The electrical power generated under illumination can be obtained directly from the cell current-voltage (*I-V*) characteristics while the incident and reflected power can be calculated from the spectral emissivity of the cell and emitter.[10]

The difference between the incident and reflected power on the cell (i.e., absorbed power) can be expressed as:[10]

$$P_{incident} - P_{reflected} = q \cdot A \cdot VF \cdot \int_0^\infty \varepsilon_{eff}(E) \cdot E \cdot b(E, T_h)\, dE \tag{4.2}$$

where A is the cell area, and VF is the apparent view factor accounting for both the fractional solid angle subtended by the emitter as viewed from the cell and the "cavity effect."[10] VF is calculated from the measured short-circuit current via:

$$I_{sc} = q \cdot A \cdot VF \cdot \int_{E_g}^\infty \varepsilon_{eff}(E)/\varepsilon_c(E) \cdot EQE(E) \cdot b(E, T_h)\, dE \tag{4.3}$$

where q is the unit charge, A is the device area, EQE is the measured external quantum efficiency of the cell.

4.5.1 Experimental characterization setup

As shown in Figure 4.5, a custom setup is used to measure *PCE* of each cell under various illumination conditions. A closed-loop chiller (Part Number: Isotemp 4100 R20, Fisher Scientific PA, 15275) maintains the temperature at 20 ℃. The thermal emitter (SiC globar or true blackbody source) is mounted on a 3-axis translational stage and centered to the cell. Voltage sweep measurements are performed at various illumination conditions using a Keithley 2401 Source Measuring Unit (SMU) in the 4-wire sensing mode to minimize the contact resistance. Figure 4.6 depicts current density-voltage (*J-V*) characteristics measured with no illumination (dark) and under various illumination conditions. I_{sc} is varied by changing the distance *d* between the cell and the emitter. With a known emitter spectrum, see Figure 4.4b, the integral is a fixed value. Then, for each measurement, the apparent view factor is directly calculated from the measured I_{sc} without the necessity of knowing the exact geometry of the emitter and cavity. The I_{sc} and the absorbed power are integrated from 0.05 eV to 3.1 eV. The amount of power outside of this range is negligible (< 0.3 %) for a ~1455 K emitter.

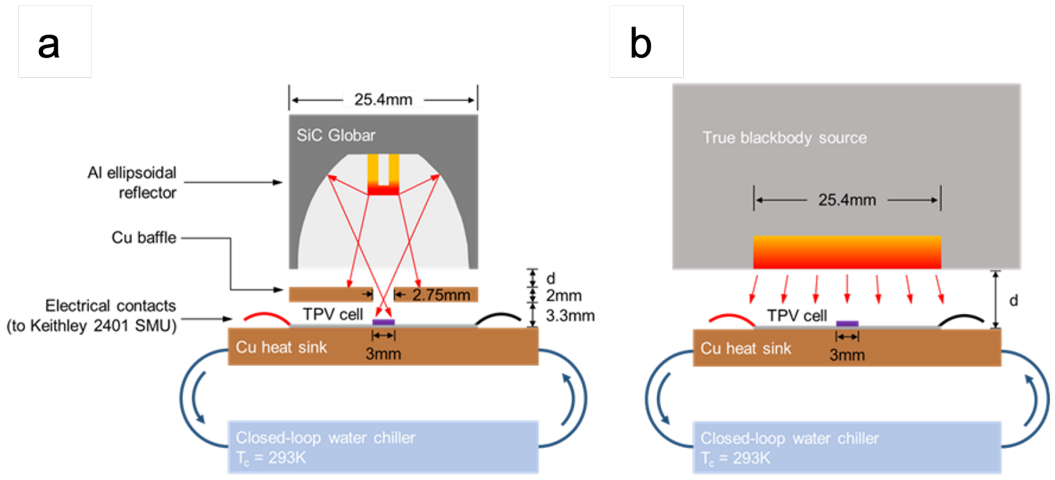

Figure 4.5. Illuminated measurement setup. Schematic of the TPV efficiency measurement setup using (a) a SiC globar emitter, and (b) a true blackbody emitter.

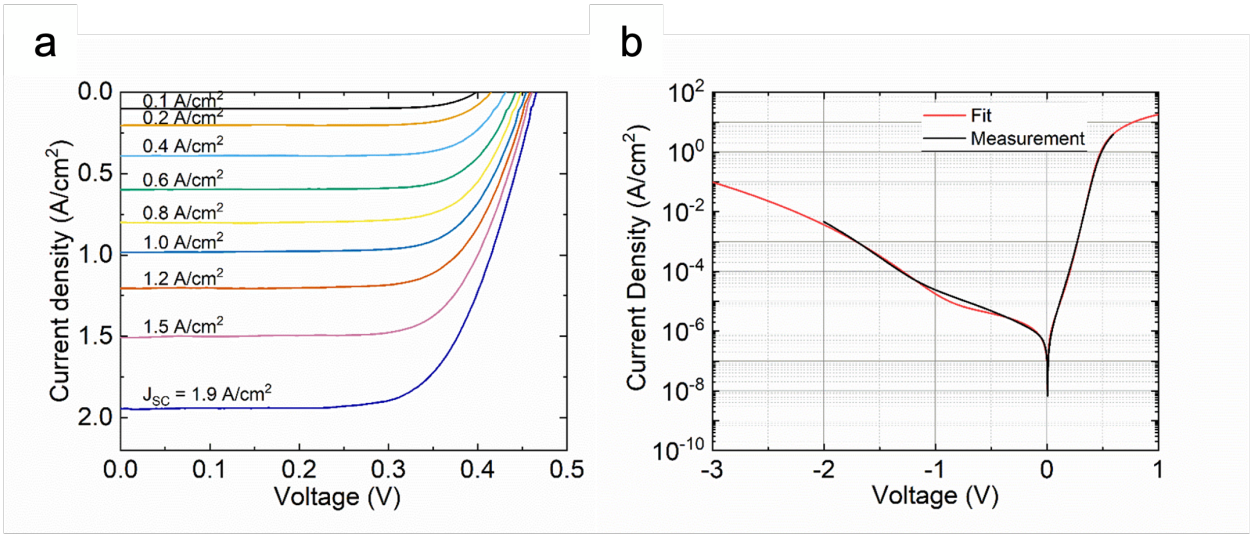

Figure 4.6. Device current-voltage characteristics. (a) Current density (J)-voltage (V) characteristics of the air-bridge TPV measured under 1455 K SiC globar illumination with varying view factors. (b) J-V characteristics of the air-bridge TPV in the dark. The reverse bias current is dominated by tunneling from -3 to -1 V, and by shunt resistance, and generation and recombination of electron-hole pairs from -1 to 0 V. The forward bias current is dominated by generation and recombination from 0 to 0.2 V, by diffusion current from 0.2 to 0.5 V, and by series resistance above 0.5 V.

4.5.2 *PCE* results

The *PCE* of each cell under various illumination conditions is shown in Figure 4.7a. The maximum *PCE* of the Au BSR cell is 23.4% at J_{sc} = 323 mA/cm^2 (apparent view factor VF = 0.129) under illumination by a SiC globar emitter at 1455 K, whereas the air-bridge cell exhibits *PCE* = 32.0 ± 0.7% at J_{sc} = 1006 ± 20 mA/cm^2 (VF = 0.402). The peak *PCE* of the air-bridge cell is 8% greater than a comparable cell fabricated on the Au BSR at a similar photocurrent under globar illumination. Given that these two cells have similar in-band absorption (~60%), this improvement is primarily (~6.5%) attributed to the reduction of out-of-band absorptance loss resulting from the inclusion of the air layer. The remaining ~1.5% difference is due the differences in electronic properties. A complete parametric set of measured J_{sc}, VF, V_{oc}, FF, and *PCE* is provided in Table 4.1. The air-bridge cell is then illuminated by a true blackbody source with emissivity >0.99, at 1473 K, achieving a maximum *PCE* = 31.3 ± 0.1%, at J_{sc} = 337 ± 1 mA/cm^2 (VF = 0.134). The diode equation is fit to the measured, dark *I-V* characteristics to model the performance of the air-bridge cell at higher blackbody illumination levels. To within error, measurements agree with simulations that predict a peak *PCE* ranging from 31.2 to 32.9%, depending on the diffuseness of the incident light. Simulation details are provided in section 4.6.

Table 4.1. Full parametric dataset from illuminated *J-V* measurements.

Au BSR TPV: SiC globar (1455 K)				
VF	J_{sc} *(mA/cm²)*	V_{oc} *(mV)*	*FF (%)*	*PCE (%)*
0.046	116.12	394.0	73.26	22.91
0.129	323.06	419.5	70.27	23.40
Air-bridge TPV: SiC globar (1455 K)				
VF	J_{sc} *(mA/cm²)*	V_{oc} *(mV)*	*FF (%)*	*PCE (%)*
0.041	101.40 ± 0.54	397.9 ± 1.4	74.84 ± 0.88	29.38 ± 0.41
0.080	201.63 ± 2.49	416.3 ± 1.8	75.20 ± 0.82	30.83 ± 0.52
0.160	398.96 ± 4.80	432.4 ± 0.8	74.28 ± 0.66	31.69 ± 0.50
0.241	603.52 ± 2.30	442.8 ± 0.6	73.30 ± 0.49	32.02 ± 0.29
0.323	806.78 ± 4.49	449.6 ± 0.2	71.96 ± 0.32	31.92 ± 0.27
0.402	1005.97 ± 20.39	454.5 ± 1.5	71.44 ± 0.38	32.03 ± 0.69
0.481	1203.60 ± 1.34	457.8 ± 1.4	70.39 ± 0.21	31.79 ± 0.19
0.606	1515.05 ± 14.93	460.5 ± 0.9	69.17 ± 0.25	31.43 ± 0.36
0.723	1806.30 ± 79.11	464.1 ± 1.1	67.23 ± 0.25	30.78 ± 1.36
Air-bridge TPV: True blackbody (1473 K)				
VF	J_{sc} *(mA/cm²)*	V_{oc} *(mV)*	*FF (%)*	*PCE (%)*
0.040	100.00 ± 0.12	400.5 ± 1.0	74.80 ± 0.13	29.66 ± 0.16
0.080	201.08 ± 0.61	415.4 ± 1.5	75.12 ± 0.15	30.90 ± 0.21
0.134	336.76 ± 1.29	424.5 ± 1.4	74.47 ± 0.10	31.30 ± 0.21

4.5.3 Electronic characterization trends

The measured, voltage-dependent current density and power density at the highest measured efficiency using the 1455 K globar are provided in Figure 4.7b. The cell has J_{sc} = 1006 ± 20 mA/cm^2, V_{oc} = 0.455 ± 0.002 V, FF = 71.4 ± 0.4%, and maximum power output P_{max} = 326.6 ± 7.0 mW/cm^2. Results for the air-bridge cell using the 1455 K globar and 1473 K true blackbody source in Figure 4.7c indicate that V_{oc} logarithmically increases with J_{sc}. FF increases at relatively

low J_{sc} (<200 mA/cm^2) and drops with increasing J_{sc} due to series resistance, R_s, as shown in Figure 4.7d. The Ohmic losses lead to a ~10% relative drop in *PCE* when *VF* approaches 1. Nevertheless, by simply lowering the temperature of the emitter to ~1325 K, *PCE* remains above 30% while satisfying *VF* = 1. This prediction highlights the favorable reduction in temperature sensitivity resulting from the inclusion of the air layer.

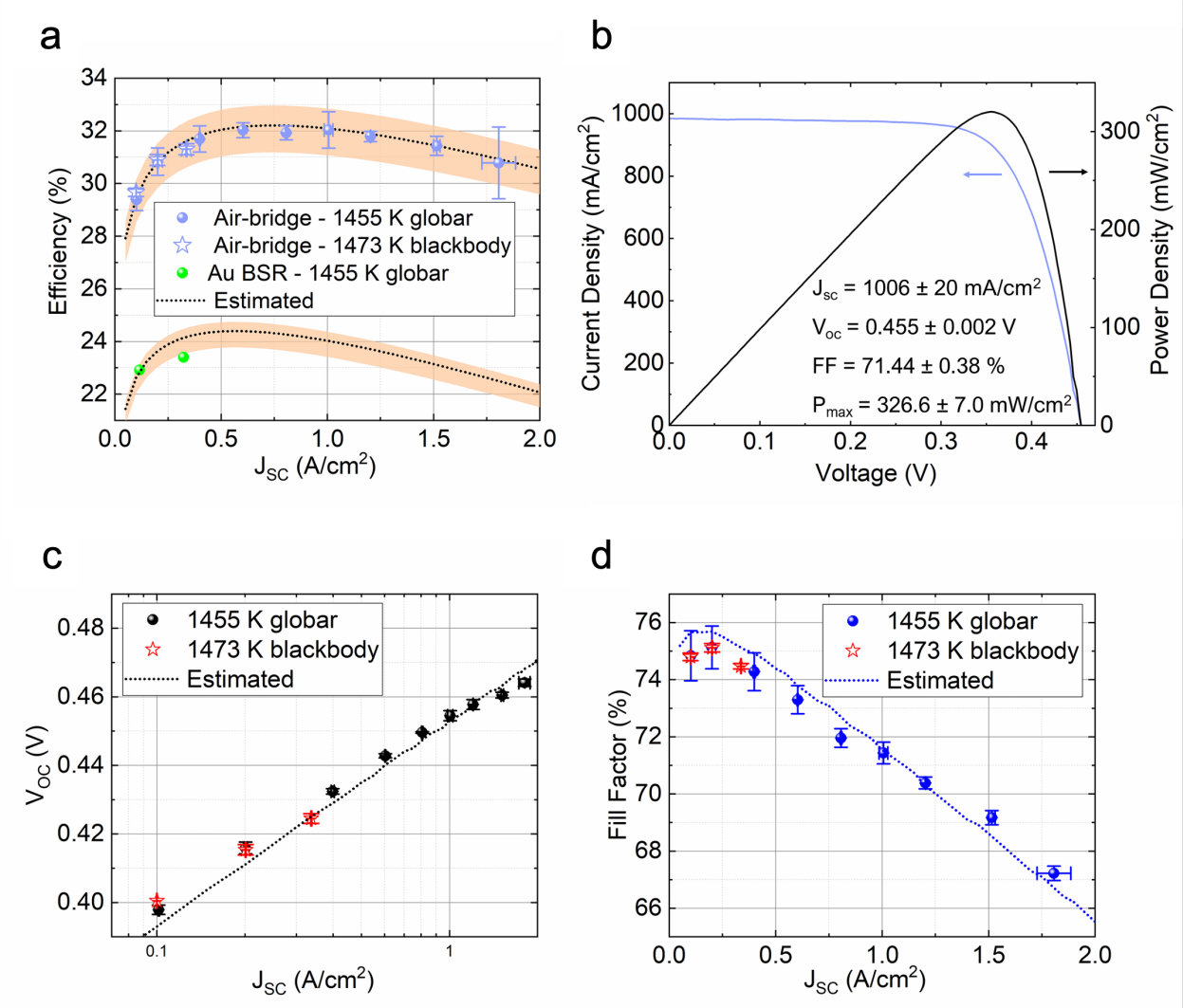

Figure 4.7 Power conversion efficiency (*PCE*). (a) *PCE* vs. short-circuit current density (J_{sc}) of the Au BSR and the air-bridge cell under 1455 K SiC globar illumination, and *PCE* of air-bridge TPV under 1473 K true blackbody illumination. Also shown are the simulated *PCE*-J_{sc} curves based on diode equation (dotted lines) and estimates (solid bands) that treat the emitter as collimated or diffused source, setting the upper and lower bounds, respectively. (b) Current

density-voltage and power density-voltage curves of the air-bridge cell at maximum measured *PCE*. (c) Measured open-circuit voltage (V_{oc}) and (d) fill factor (*FF*) of the of the air-bridge cell under 1455 K globar (black circles in 4.4c, blue circles in 4.4d) and 1473 K true blackbody (stars) illumination. Also shown are the simulated V_{oc}-J_{sc} (dashed line in 4.4c) and *FF*-J_{sc} (dashed line in 4.4d) characteristics of the air-bridge cell.

4.5.4 Limitations of lab-scale *PCE* characterization

I note here the inherent limitations of laboratory-scale characterization of *PCE*. TPV efficiency typically drops when it is translated to realistic devices at larger scales; a phenomenon that is common to all photovoltaic device types.[11] This decrease is a result of compromises made in component integration, variations in cavity design, and reduced peak performance of modules compared to optimized, small laboratory test devices. For example, Wernsman, *et al.*[9] report *PCE* = 23.6% for a 0.6 eV InGaAs cell under illumination by a 1312 K SiC emitter, but this drops to 19.1% when integrated into an 82 cm^2 array employed in a prototypical radioisotope TPV system.[12] This reduction was attributed to parasitic absorption by cell edges, and non-uniform array illumination. To mitigate these losses, it may be beneficial to pair air-bridge cells with selective emitters.[13,14]

4.6 Current-voltage characterization and diode equation fitting for PCE modeling

Here the dark *J-V* properties of the air-bridge cell are fit to the double diode model described in Chapter 1. This model is then used to project how the air-bridge cell may perform outside of current experimental capabilities.

By fitting the measured dark *J-V* curve, Figure 4.6b, of the air-bridge TPV cell, the following parameters are extracted: J_0 = 22.6 nA/cm^2, J_{GR} = 707.4 nA/cm^2, $R_{sh} > 2\times10^6$ Ω, $\tau_{SRH} > 4$ μs, and

R_s = 26 mΩ·cm^2. Illuminated *J-V* curves are simulated at various J_{ph} to calculate the simulated performance metric curves in Figure 4.7a, c, and d.

Further, I use the described model to breakdown the primary loss pathways that separate the experimentally measured efficiency from the radiative limit efficiency for this system. Figure 4.8 depicts the efficiency drop associated with each of these loss pathways. With the decreased out-of-band reflectance of the air-bridge cell, non-radiative recombination in the junction is observed to be the largest single loss pathway.

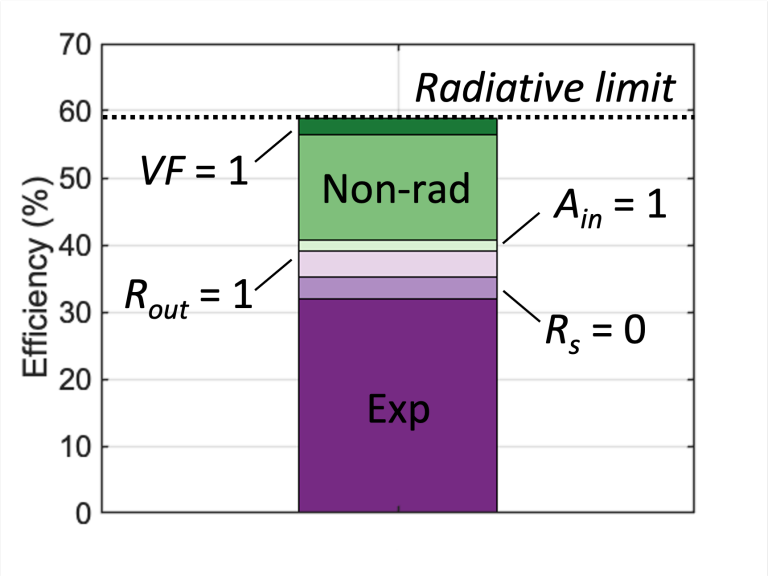

Figure 4.8. Loss breakdown for the air-bridge cell. Losses associated with imperfect series resistance R_s, out-of-band reflectance R_{out}, in-band absorptance A_{in}, non-radiative recombination, and view factor *VF* are shown to separate the experimental *PCE* (purple) from the radiative limit efficiency (dashed black line).

4.7 Conclusions

In summary, this work demonstrates a TPV cell with nearly perfect spectral utilization, where loss of photogenerated carriers and parasitic absorption account for less than 3% of the power radiated by a ~1455 K blackbody. This was achieved by introducing an air layer within the thin-film TPV

cell and represents a four-fold reduction in absorption of low-energy photons relative to the prior best TPV cells. By recuperating nearly 99 % of out-of-band radiated power, the efficiency of the air-bridge cell exhibits significant improvement compared to a reference cell fabricated on the Au back surface reflector, and >30% peak *PCE* for a 1455 K thermal emitter. Nearly perfect photon utilization enabled by the air-bridge design provides a potential pathway to use low-cost cells and heat sources for TPV power conversion.

4.8 References

1. Swanson, R.M. (1980). Recent developments in thermophotovoltaic conversion. In 1980 International Electron Devices Meeting (IRE), pp. 186–189.
2. Omair, Z., Scranton, G., Pazos-Outón, L.M., Xiao, T.P., Steiner, M.A., Ganapati, V., Peterson, P.F., Holzrichter, J., Atwater, H., and Yablonovitch, E. (2019). Ultraefficient thermophotovoltaic power conversion by band-edge spectral filtering. Proc. Natl. Acad. Sci. *116*, 15356–15361.
3. Burger, T., Sempere, C., and Lenert, A. Thermophotovoltaic energy conversion: materials and device engineering.
4. Burger, T., Fan, D., Lee, K., Forrest, S.R., and Lenert, A. (2018). Thin-Film Architectures with High Spectral Selectivity for Thermophotovoltaic Cells. ACS Photonics *5*, 2748–2754.
5. Bauer, T. (2011). Thermophotovoltaics (Springer Berlin Heidelberg).
6. Peumans, P., Yakimov, A., and Forrest, S.R. (2003). Small molecular weight organic thin-film photodetectors and solar cells. J. Appl. Phys. *93*.
7. Lee, K., Shiu, K.-T., Zimmerman, J.D., Renshaw, C.K., and Forrest, S.R. (2010). Multiple growths of epitaxial lift-off solar cells from a single InP substrate. Appl. Phys. Lett. *97*, 101107.
8. Chancerel, F., Regreny, P., Leclercq, J.L., Brottet, S., Volatier, M., Jaouad, A., Darnon, M., Fafard, S., Blanchard, N.P., Gendry, M., et al. (2019). Epitaxial lift-off of InGaAs solar cells from InP substrate using a strained AlAs/InAlAs superlattice as a novel sacrificial layer. Sol. Energy Mater. Sol. Cells *195*, 204–212.
9. Wernsman, B., Siergiej, R.R., Link, S.D., Mahorter, R.G., Palmisiano, M.N., Wehrer, R.J., Schultz, R.W., Schmuck, G.P., Messham, R.L., Murray, S., et al. (2004). Greater Than 20% Radiant Heat Conversion Efficiency of a Thermophotovoltaic Radiator/Module System Using Reflective Spectral Control. IEEE Trans. Electron Devices *51*, 512–515.
10. Mahorter, R.G., Wernsman, B., Thomas, R.M., and Siergiej, R.R. (2003). Thermophotovoltaic system testing. Semicond. Sci. Technol.
11. Green, M.A., Dunlop, E.D., Hohl-Ebinger, J., Yoshita, M., Kopidakis, N., and Ho-Baillie, A.W.Y. (2020). Solar cell efficiency tables (Version 55). Prog. Photovoltaics Res. Appl. *28*, 3–15.
12. Crowley, C.J. (2005). Thermophotovoltaic Converter Performance for Radioisotope Power Systems. AIP Conf. Proc. *746*, 601–614.
13. Sakakibara, R., Stelmakh, V., Chan, W.R., Ghebrebrhan, M., Joannopoulos, J.D., Soljačić, M., and Čelanović, I. (2019). Practical emitters for thermophotovoltaics: a review. J. Photonics Energy *9*, 032713.
14. Raman, V.K., Burger, T., and Lenert, A. (2019). Design of thermophotovoltaics for tolerance of parasitic absorption. Opt. Express *27*, 31757.

Chapter 5: Transmissive Spectral Control for Eliminating Out-of-Band Loss in Thermophotovoltaic Cells

5. 1 Motivation

Because of the largely diminished out-of-band loss, the spectral efficiency[1] of the air-bridge cell[2] exhibits reduced sensitivity to changes in cell bandgap and emitter temperature in comparison to cells utilizing a conventional metallic back surface reflector. However, several envisioned applications of thermophotovoltaics, such as concentrated solar power,[3–10] waste heat scavenging,[11,12] and use of Si cells in moderate temperature applications, require further insensitivity to variable bandgap and temperature to preserve these performance metrics. Figure 5.1 depicts how spectral efficiency changes when translating to these envisioned applications. To achieve full bandgap-temperature insensitivity in the desired range, it is necessary to suppress >99% of out-of-band radiation. The performance of the air-bridge architecture is constrained by absorptance in the rear reflector, which increases with the angle of incidence; optical simulation predicts 98.9% reflectance for normal incidence and 98.2% reflectance for a Lambertian source with incidence from 0° to 90°.[2] The air-bridge architecture, therefore, is unable to access the described regime.

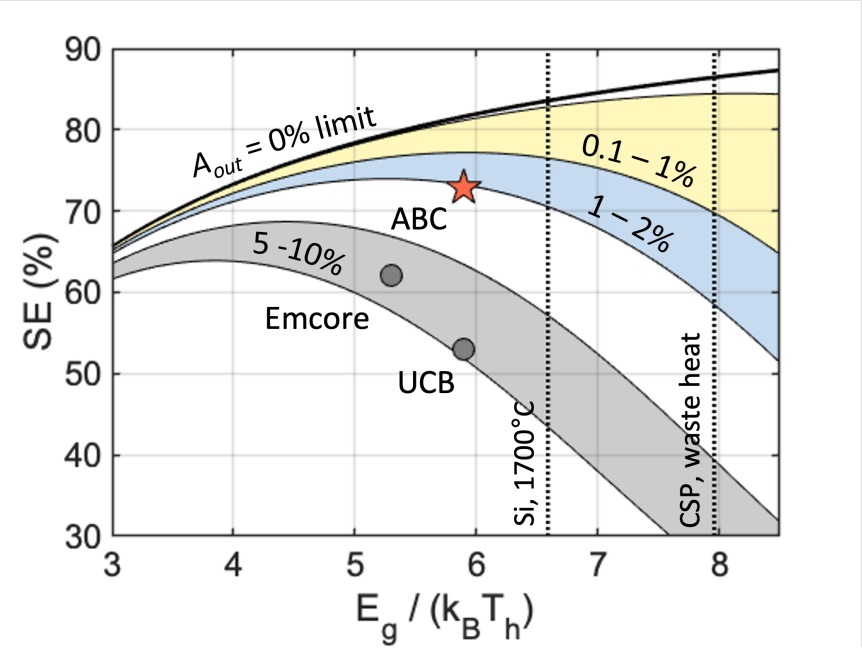

Figure 5.1. Spectral efficiency as a function of cell bandgap *a*nd emitter temperature. The black curve indicates *SE* in the radiative limit (A_{out} = 0). Prior Au BSR works (UCB[13] and Emcore[14]) have 5% < A_{out} < 10% and typically operate in the shaded gray regime, in which *SE* exhibits a strong dependence on variable bandgap E_g and emitter temperature T_h. The air-bridge architecture[2] reduces this dependence by decreasing out-of-band loss such that 1% < A_{out} < 2%, as indicated by the shaded blue region. The proposed transparent cell concept may enable further decrease to out-of-band loss, such that 0.1% < A_{out} < 1%. In this regime, shaded yellow, *SE* becomes nearly independent of E_g and T_h, thereby enabling potential TPV applications in concentrated solar power, waste heat scavenging, and moderate T_h, Si absorber systems.

This chapter presents a new approach for achieving wavelength-selective radiative transport: use of partially transparent cells paired with rear surface view of a secondary emitter. Figure 5.2a illustrates this concept. This architecture relies on the bonding of the absorber film to a transparent substrate. While not inherently necessary for realization of this concept, the air-bridge fabrication protocol is a convenient method for achieving this structure. In this iteration, the Au rear reflector is removed to make the cell partially transparent. Figure 5.2b depicts a modular design in which emitters and cells are interfaced using a finned geometry to enable the envisioned transmissive photon recuperation process.

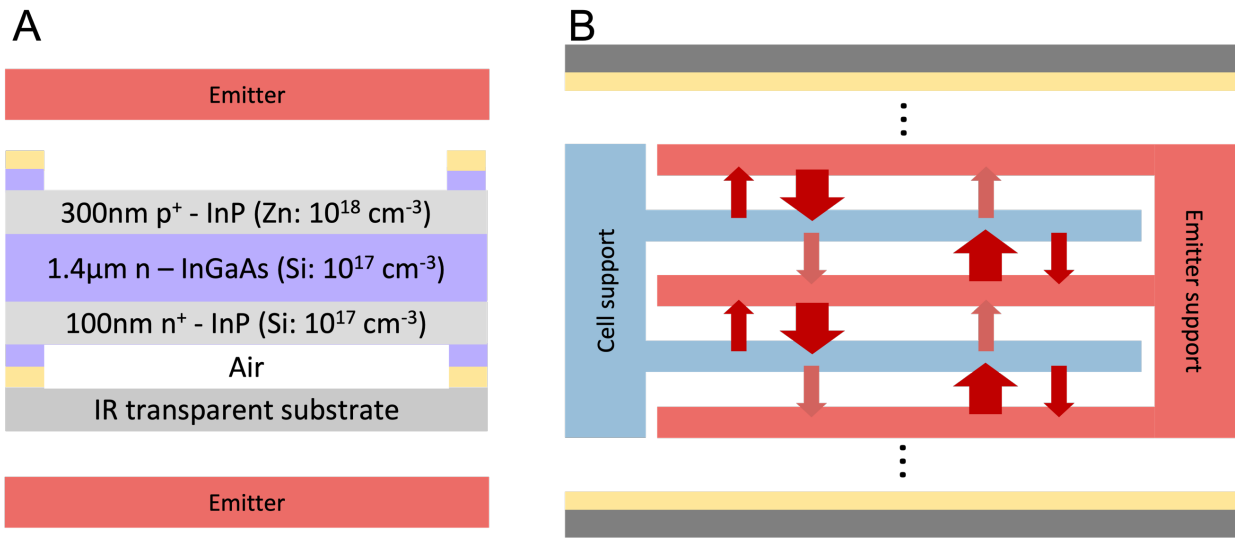

Figure 5.2. Concept for the partially transparent TPV cell. (a) Transparent cell architecture. (b) Proposed modular design for interfacing cells and emitters. Arrows indicate incident, reflected, and transmitted power.

This chapter present a proof-of-principle demonstration of the transparent cell concept. I first describe the role of the transparent substrate and its implications on the optical and thermal properties of the proposed transparent cell architecture. A two-dimensional cathode support grid is developed that enables experimental fabrication of the transparent architecture. I then fabricate and characterize the optical properties of the transparent cell and a reflective air-bridge control. Lastly, I show that the transparent architecture enables a pathway to eliminating the bandgap-temperature tradeoff by decoupling the absorptive properties of the heterostructure and the Si substrate using an optical model informed by spectral characterization of the substrate.

5.2 Transparent cell design considerations

One of the most important design considerations for the transparent cell pertains to selection of the substrate. The substrate must exhibit near-complete IR transparency and simultaneously support lateral heat conduction for sufficient thermal management of the cell. In the present work,

I have selected double-side polished Si as a candidate material. Si is chemically compatible with existing device fabrication processes, exhibits low optical absorption in the IR, and has an acceptable heat transfer coefficient of 1.3 W/cm/K. Specifically, I have opted to work with intrinsic, float zone Si to minimize absorption by free carriers and lattice impurities.

Figure 5.3a depicts an FTIR transmission measurement of the 280μm Si wafer used for fabrication of the proof-of-principle transparent cell. Experimental transmittance is observed to deviate from simulated transmittance at low energies, amounting to 1.4% of out-of-band power as defined for the target InGaAs absorber / 1500K blackbody emitter system. This spectral characteristic is consistent with free carrier absorption, which is assumed here to be well described with a Drude model given by:

$$\epsilon = \epsilon_\infty - \frac{\omega_p^2}{\omega^2 - \omega\gamma i} \tag{5.1}$$

where ϵ is the permittivity, ϵ_∞ is the core dielectric constant, ω is the frequency, ω_p is the plasma frequency, and γ is the damping coefficient. This model is fit to the free carrier absorption profile of the Si wafer to extract the permittivity ϵ (Figure 5.3b). The damping coefficient γ is the only free parameter in this model as the core dielectric constant ϵ_∞ and plasma frequency ω_p are fixed according to the properties of intrinsic Si (Table 5.1). Optical parameters n and k are calculated from the permittivity as the real and imaginary parts of $\sqrt{\epsilon}$, respectively, and used as inputs in the transfer matrix simulation. This model shows that the substrate alone will absorb 1.1% of out-of-band radiation when integrated into the proposed structure (Figure 5.3c).

Table 5.1. Drude model parameters for polished Si Wafer.

ϵ_∞	n_i	m_{eff}	ω_p	γ
11.7	9.7 x 10^9 cm^{-3} [15]	0.31m_e [a 16]	9.9 x 10^{13} s^{-1} [b]	1.1 x 10^{12} s^{-1}

[a]Effective carrier mass of intrinsic is calculated as the average of the conductivity effective mass of electrons (0.26m_e) and holes (0.36m_e).

[b]Plasma frequency is calculated as $\omega_p = \frac{n_i q^2}{\epsilon_0 m_{eff}}$ where q is the elementary charge of an electron and ϵ_0 is the permittivity of free space. m_e is the electron rest mass.

I acknowledge, given this preliminary analysis, that the identified 280μm FZ Si wafer is an imperfect optical substrate for the target application. Out-of-band absorptance in the substrate alone is expected to exceed the threshold of A_{out} = 1% for entering the described *SE* regime. The present work will therefore serve as a proof-of-concept.

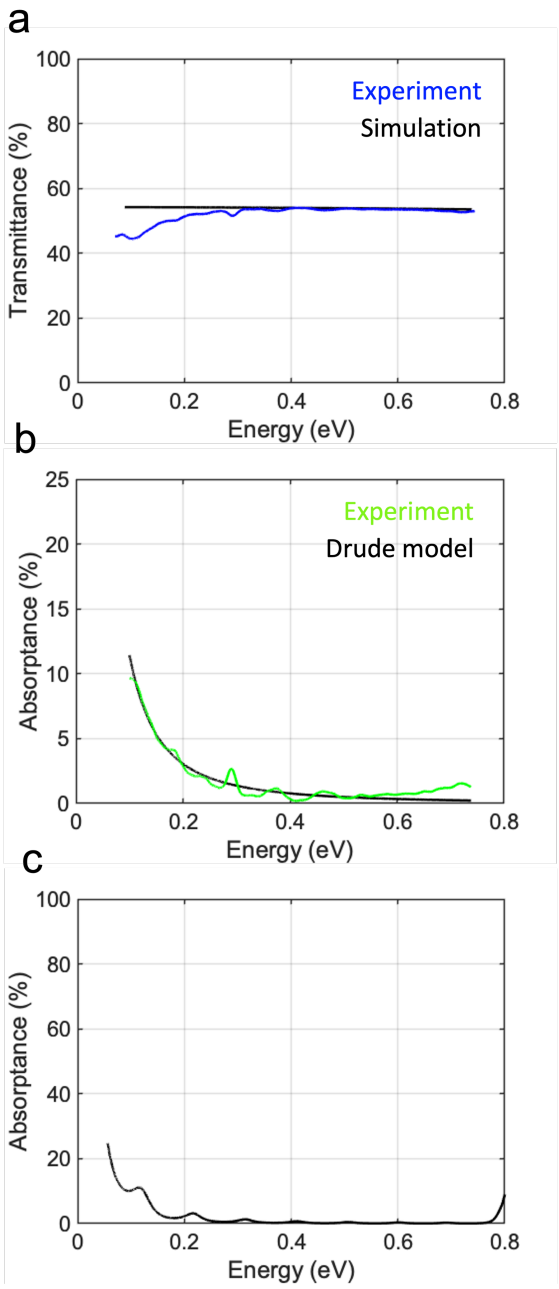

Figure 5.3. Spectral characterization of the polished Si wafer. (a) Experimental (blue) and simulated (black) transmittance of the DSP Si wafer used as the handle for the transparent cell. Experimental transmittance is observed to diverge from simulation at low energies, consistent with the free carrier absorption mechanism. (b) Experimental (green) and simulated (black) absorptance of the DSP Si wafer as described by the Drude free carrier absorption model. (c) Simulated absorptance of the proposed transparent structure, as modeled based on the extracted optical properties of the DSP Si substrate.

5.3 Device fabrication

Whereas formation of the air-bridge architecture requires bonding of a single patterned contact to a planar Au-coated substrate,[2] fabrication of the described transparent cell necessitates aligned bonding of two complimentary patterned surfaces. Flip chip bonding techniques may theoretically enable sample positioning with 500nm placement accuracy, but Figure 5.4a shows that technique may not place repeatably with <10μm accuracy. Given the width of the grid lines (10μm), transparent cell fabrication cannot tolerate this degree of misalignment. I therefore make use of a two-dimensional rear grid to establish tolerance to the anticipated misalignment during flip chip bonding (Figures 5.4b-d). This design choice slightly reduces the geometric fill factor for the transparent region, as a portion of the film is suspended above the rear grid lines deposited on the Si substrate. The described structure yields a geometric fill factor of 71.2% for the transparent region, 15.6% for the top contact grid, and 13.2% for a reflective air-bridge region. Following formation of the two-dimensional support grid, fabrication of the transparent cell closely follows that of the reflective air-bridge, as described in section 5.3.2.[2]

5.3.1 Material growth

The heterostructure was epitaxially grown on a 300μm thick (100) InP substrate using metalorganic chemical vapor deposition (University Wafer). The epitaxial film consists of a 200nm thick Mg-doped (1×10^{18} cm^{-3}) $In_{0.53}Ga_{0.47}As$ (InGaAs) front contact layer, 300nm Mg-doped (1×10^{18} cm^{-3}) InP front window layer, 1.4μm thick Si-doped (1×10^{17} cm^{-3}) InGaAs absorber layer, 100 nm Si-doped (1×10^{18} cm^{-3}) InP rear window layer, and 100nm thick Si-doped (1×10^{18} cm^{-3}) InGaAs rear contact layer.

5.3.2 Fabrication protocol

All layers are patterned photolithographically using SPR 220 3.0 photoresist (MicroChem Corp). Metal deposition layers are patterned using LOR 10B (MicroChem Corp) and SPR 220 3.0 bilayer photoresist. The epitaxial sample and a Si wafer are soaked in buffered HF for 90s to remove the native surface oxide. The cathode contact grid (10nm Ti / 225nm Au) is deposited by electron-beam evaporation. Grid lines are 10μm wide with 54μm spacing. The epitaxial sample is then soaked in 1:1:8 H_3PO_4:H_2O_2:H_2O for 20s to remove the 100nm thick InGaAs rear contact layer in the area between grid lines, while the contact layer beneath the grid lines is protected from etching. Orthogonal Au patterns on the epitaxial sample and Si wafer are spatially aligned and bonded using a flip chip bonder (Finetech) by applying heat (150°C) and pressure (2MPa) for 5 minutes. Bond strength is reinforced at the same temp and higher pressure (8MPa) for 10 minutes using an EVG 510 wafer bonder (EV Group Inc.). The bonded sample is soaked in HCl for 90 minutes to remove the InP substrate. This processing is compatible with non-destructive epitaxial lift-off techniques, which may preserve the expensive InP growth substrate for additional growths. The device mesa is etched by alternating soaks in InGaAs etchant (1:1:8 H_3PO_4:H_2O_2:H_2O) and InP etchant (1:1 HCl:H_2O). The anode contact grid (10nm Ti / 30nm Pt / 560nm Au) is deposited by electron-beam evaporation. The anode contact grid is spatially aligned to the epilayer's buried cathode contact grid to shade the absorptive InGaAs rear contact later. Lastly, the sample is soaked in 1:1:8 H_3PO_4:H_2O_2:H_2O 60s to remove the the 300nm thick InGaAs front contact between the grid lines.

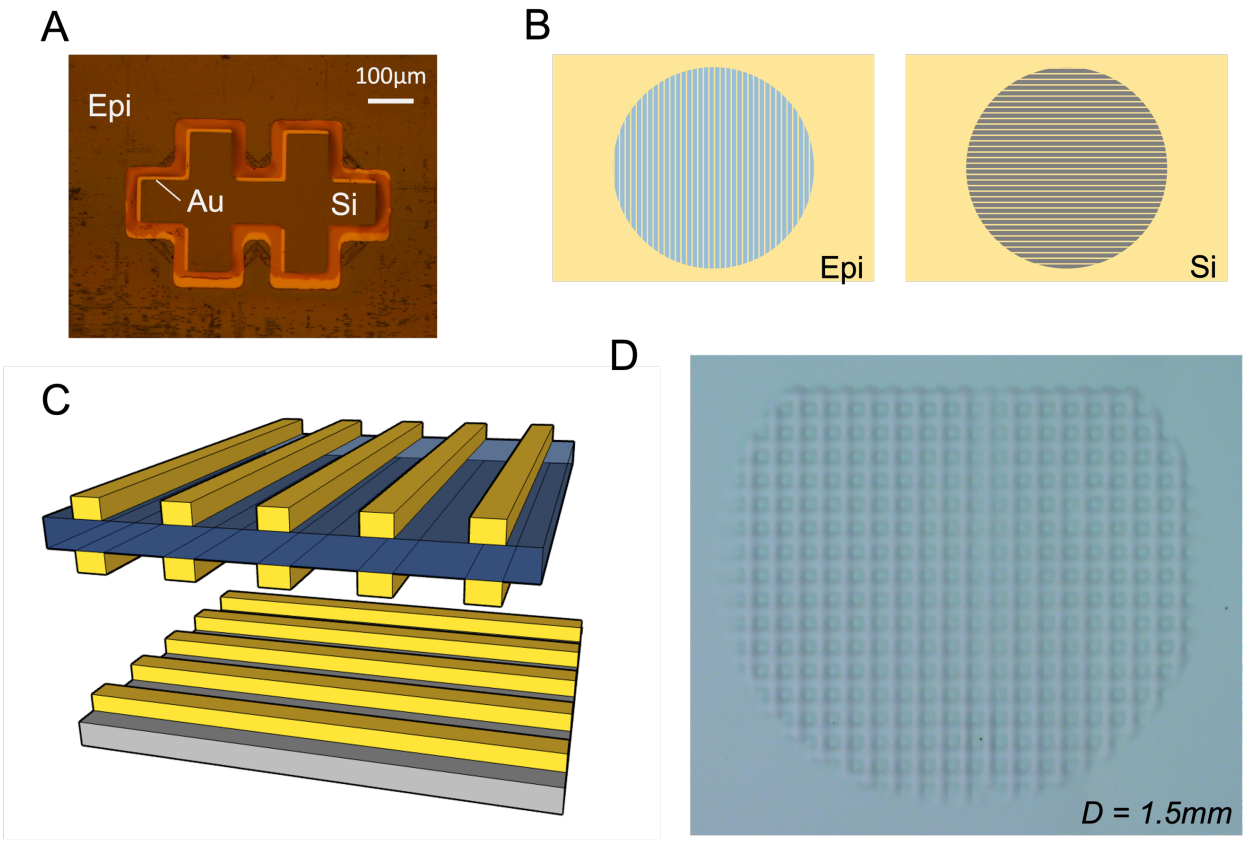

Figure 5.4. Two-dimensional support grid for misalignment tolerance. (a) Top-view optical image of fiducial marks on the surface of the transparent cell after flip chip bonding. Misalignment on the order of 10μm along both the x- and y-axis is observed. (b) Schematic of grid lines patterned on the epitaxial sample (vertical) and Si handle (horizontal). Joining these complimentary patterns forms the described two-dimensional grid. (c) Schematic of the two-dimensional support grid between the heterostructure and the Si substrate. (d) Top-view optical image of a 1.5mm diameter heterostructure film supported by the described two-dimensional grid.

5.4 Results

5.4.1 Spectral characterization of the reflective control cell

Figure 5.5 shows the reflective properties of the control air-bridge cell alongside expected spectral reflectance based on optical simulation. Weighted R_{out} is observed to be 97.6%, deviating slightly from the simulated value of 98.3%. 1.7% absorptance is attributed to the Au reflector based on simulation. The remaining 0.7% absorptance is therefore attributed to the heterostructure. This film is more absorptive than the heterostructure from the reflective air-bridge work, which

exhibited ~0.1% out-of-band absorptance.[2] This gap may be attributed to differences in the growth process (MOCVD, rather than MBE) and/or structural differences; this film is 40% thicker and utilizes a different p-type dopant species.

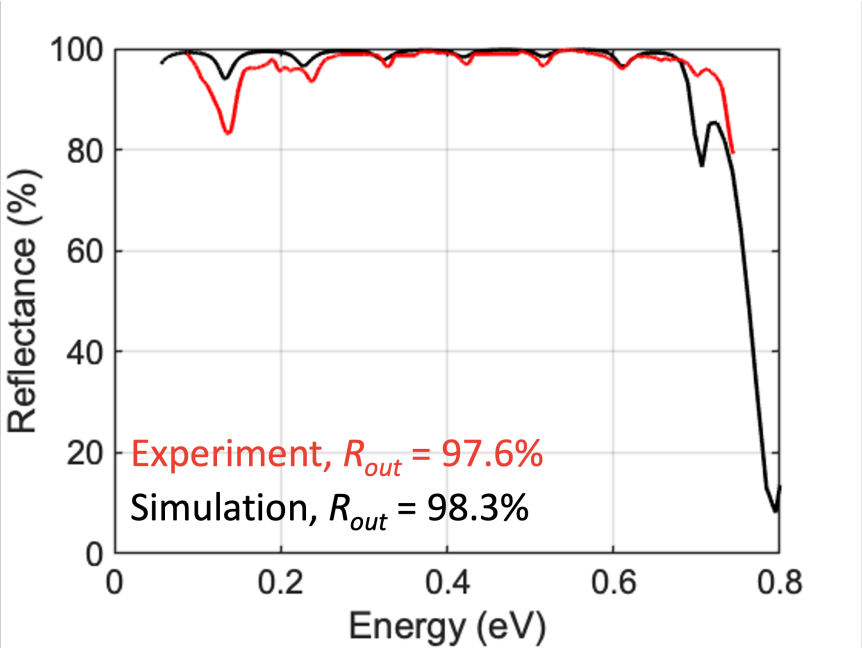

Figure 5.5. Spectral characterization of the reflective air-bridge control. Experimental (red) and simulated (black) reflectance of the reflective air-bridge control cell. Experimental R_{out} (97.6%) is observed to deviate slightly from the simulated value (98.3%), indicating parasitic absorptance in the heterostructure film.

5.4.2 Spectral characterization of the transparent cell

Figure 5.6 depicts experimental reflective and transmissive properties of the transparent cell alongside the spectral properties predicted by simulation. Experimental R_{out} is observed to be 69.5%, slightly below the simulated value of 70%. Experimental out-of-band transmittance T_{out} is measured to be 28.7%, deviating slight from the simulated value of 30%. Out-of-band absorptance of the full transparent cell is then calculated as $A_{out} = 1 - (R_{out} + T_{out})$ to be 1.8%. 1.1% absorptance is attributed to the Si handle based on the spectral analysis in section 5.2. The

remaining 0.7% is therefore attributed to the heterostructure, in good agreement with the reflective control.

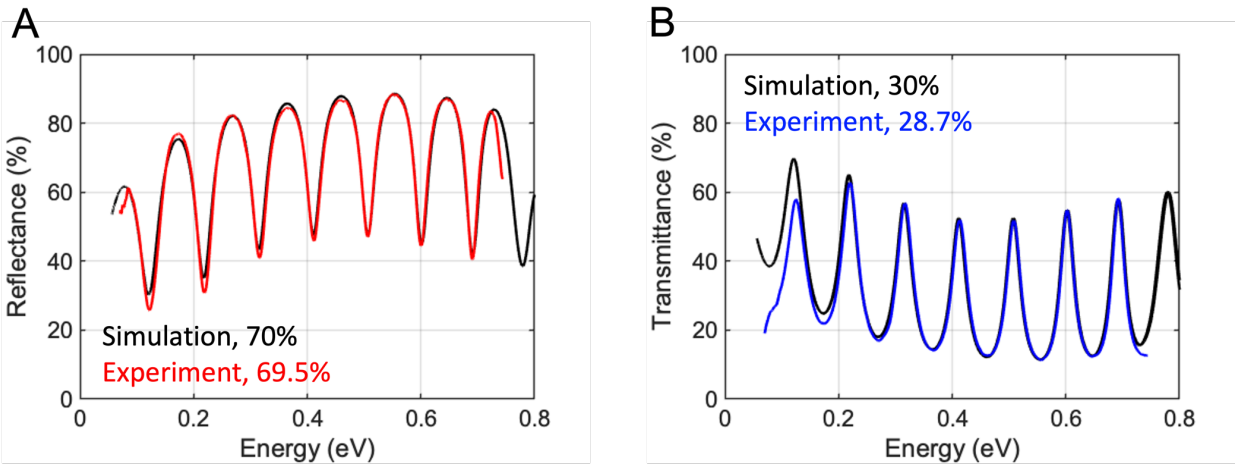

Figure 5.6. Spectral characterization of the transparent cell. (a) Experimental (red) and simulated (black) reflectance of the transparent cell. (b) Experimental (blue) and simulated (black) transmittance of the transparent cell. Experimental deviation of the experimental values from simulation are attributed to parasitic absorptance in the heterostructure and Si substrate.

5.4.3 Electronic characterization

Figure 5.7 shows the illuminated current-voltage characteristics of the transparent cell. The diode is observed to exhibit a Schottky barrier that results in poor fill factor at all illumination conditions. Similar properties are observed for the reflective control. This issue may be related to contact layer doping levels or the metal grid deposition process. Given this complication, I do not further characterize the electronic properties of the cells or describe conversion efficiency.

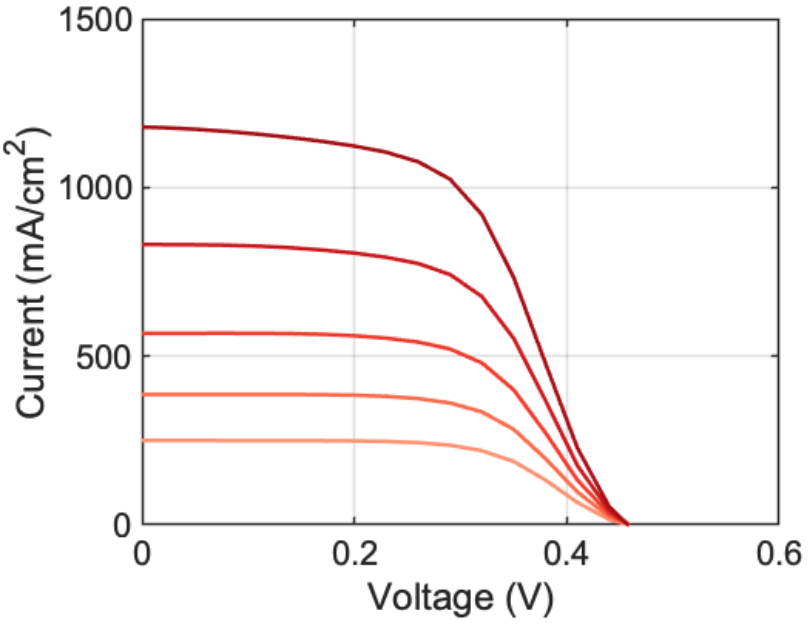

Figure 5.7. Illuminated current-voltage *J-V* properties of the transparent cell. Measurements are taken at a fixed emitter temperature T_h = 1600K.

5.5 Discussion

By decoupling the transparent cell's absorptance into contributions from the Si substrate (1.1%) and the heterostructure absorber (0.7%), I show that realization of this concept using a more transparent substrate may enable a cell to go below the sub-1% A_{out} threshold. The choice of substrate material and geometry is not trivial. The substrate must simultaneously support sufficient heat conduction and absorb less out-of-band power than a Au rear reflector. These characteristics are often exclusive in candidate materials; optical materials with low absorption frequently act as thermal insulators. For example, sapphire (Al_2O_3) is a leading candidate for replacing Si as the substrate material given its optical properties and chemical compatibility with processing techniques, however its heat transfer coefficient is three times less than that of Si. Use of thinner Si also presents a tradeoff since the temperature drop along the length of the cell will scale inversely with the cross section available for heat conduction. The unique geometry of the

proposed modular design (Figure 5.2b) is further expected to induce a temperature gradient along the length of the emitter, with the coolest temperatures existing at the ends of the fins. Spatial non-uniformities in illumination of the corresponding transparent cells may reduce modular efficiencies by introducing mismatched currents across series-interconnected cells. Sub-system and prototype design will therefore necessitate consideration of emitter geometries that minimize temperature gradients. Such modular design choices could involve supporting emitter fins at both ends in order to cut the heat conduction length in half. Materials selection and geometrical design for the proposed transparent TPV module will require an optimization study that captures how the heat conduction and optical properties of proposed materials vary as a function of geometry.

5.6 Conclusions

In summary, this chapter describes a proof-of-principle for the transparent cell concept. This work represents a new approach for achieving wavelength-selective radiative transport in thermophotovoltaic systems that has the potential to overcome the limitations of air-bridge reflectance. The transparent cell is experimentally realized through use of a two-dimensional rear support grid, which establishes a wider tolerance to misalignment during the thermocompression bonding step and can thus be more readily implemented at scale. Experimental spectral analysis using FTIR is paired with transfer matrix optical simulation techniques to decouple contributions to out-of-band absorptance in the transparent cell and an air-bridge reflective control. The polished Si substrate used as the transparent cell handle accounts for the majority (1.1%) of the 1.8% out-of-band absorptance in the cell. The remaining 0.7% absorptance is attributed to the heterostructure film, in good agreement with the reflective control. Use of a higher transparency substrate is thus needed to enable operation in the target regime, in which the dependence of spectral efficiency *SE*

on cell bandgap and emitter temperature is nearly eliminated (i.e., $A_{out} < 1\%$). Future work should seek to surpass the described threshold experimentally through use of a different substrate.

5.7 References

1. Burger, T., Sempere, C., Roy-Layinde, B., and Lenert, A. (2020). Present Efficiencies and Future Opportunities in Thermophotovoltaics. Joule *4*, 1660–1680.
2. Fan, D., Burger, T., McSherry, S., Lee, B., Lenert, A., and Forrest, S.R. (2020). Near-perfect photon utilization in an air-bridge thermophotovoltaic cell. Nature.
3. Lenert, A., Bierman, D.M., Nam, Y., Chan, W.R., Celanović, I., Soljačić, M., and Wang, E.N. (2014). A nanophotonic solar thermophotovoltaic device. Nat. Nanotechnol. *9*, 126–130.
4. Harder, N.-P., and W rfel, P. (2003). Theoretical limits of thermophotovoltaic solar energy conversion. Semicond. Sci. Technol. *18*, S151–S157.
5. Ungaro, C., Gray, S.K., and Gupta, M.C. (2015). Solar thermophotovoltaic system using nanostructures. Opt. Express *23*, A1149–A1156.
6. Rephaeli, E., and Fan, S. (2009). Absorber and emitter for solar thermo-photovoltaic systems to achieve efficiency exceeding the Shockley-Queisser limit. Opt. Express *17*, 15145–15159.
7. Zhou, Z., Sakr, E., Sun, Y., and Bermel, P. (2016). Solar thermophotovoltaics: reshaping the solar spectrum. Nanophotonics *5*, 1–21.
8. Wang, Y., Liu, H., and Zhu, J. (2019). Solar thermophotovoltaics: Progress, challenges, and opportunities. APL Mater. *7*, 080906.
9. Bierman, D.M., Lenert, A., Chan, W.R., Bhatia, B., Celanović, I., Soljačić, M., and Wang, E.N. (2016). Enhanced photovoltaic energy conversion using thermally based spectral shaping. Nat. Energy *1*, 16068.
10. Bhatt, R., Kravchenko, I., and Gupta, M. (2020). High-efficiency solar thermophotovoltaic system using a nanostructure-based selective emitter. Sol. Energy *197*, 538–545.
11. Licht, A., Pfiester, N., DeMeo, D., Chivers, J., and Vandervelde, T.E. (2019). A Review of Advances in Thermophotovoltaics for Power Generation and Waste Heat Harvesting. MRS Adv. *4*, 2271–2282.
12. Chen, K., Santhanam, P., and Fan, S. (2015). Suppressing sub-bandgap phonon-polariton heat transfer in near-field thermophotovoltaic devices for waste heat recovery. Appl. Phys. Lett. *107*, 091106.
13. Omair, Z., Scranton, G., Pazos-Outón, L.M., Xiao, T.P., Steiner, M.A., Ganapati, V., Peterson, P.F., Holzrichter, J., Atwater, H., and Yablonovitch, E. (2019). Ultraefficient thermophotovoltaic power conversion by band-edge spectral filtering. Proc. Natl. Acad. Sci. *116*, 15356–15361.
14. Wernsman, B., Siergiej, R.R., Link, S.D., Mahorter, R.G., Palmisiano, M.N., Wehrer, R.J., Schultz, R.W., Schmuck, G.P., Messham, R.L., Murray, S., et al. (2004). Greater Than 20% Radiant Heat Conversion Efficiency of a Thermophotovoltaic Radiator/Module System Using Reflective Spectral Control. IEEE Trans. Electron Devices *51*, 512–515.
15. Altermatt, P.P., Schenk, A., Geelhaar, F., and Heiser, G. (2003). Reassessment of the intrinsic carrier density in crystalline silicon in view of band-gap narrowing. J. Appl. Phys. *93*, 1598–1604.
16. Willis, K.J., Hagness, S.C., and Knezevic, I. (2013). A generalized Drude model for doped silicon at terahertz frequencies derived from microscopic transport simulation. Appl. Phys. Lett. *102*, 1–4.

Chapter 6: Conclusions and Outlook

6.1 Conclusions

Thermophotovoltaic energy conversion offers a more flexible approach for electricity generation than conventional mechanical energy conversion processes. Widespread implementation of TPVs in next-generation energy generation and storage applications may enable primary energy savings and greater penetration of intermittent renewables. This thesis explores methods for nearly eliminating one of the largest loss pathways in TPV energy conversion systems, radiative transfer of unusable, out-of-band power between the emitter and cell. An exhaustive review of the experimental literature revealed the shortcomings of existing methods for eliminating this loss pathway and identified opportunities for continued improvements that motivated subsequent experimental works. The first of these experimental works showed how candidate thin-film InGaAs optical structures may be optimized to improve out-of-band spectral properties. The fabrication protocol was shown to be compatible with non-destructive epitaxial liftoff, an approach that may enable substantial cost savings through reuse of the expensive crystalline growth substrate. Secondly, this thesis reported on record-high conversion efficiency enabled by the air-bridge TPV cell architecture. This novel architecture leverages the high refractive index contrast between the InGaAs/InP heterojunction and a buried air cavity to achieve near-perfect out-of-band reflectance. Lastly, this thesis introduces an entirely new approach to photon management in TPV

systems, the use of partially transparent cells with rear view of a secondary emitter. This proof-of-principle study showed a path to operation in a new regime in which high efficiencies may be more easily translated to component materials and application spaces that were previously considered impractical.

In this chapter, I describe some of the immediate challenges facing continued development of thermophotovoltaic systems and highlight several promising directions for the field.

6.2 Standardization of TPV characterization protocol

In contrast to solar PV, the field of thermophotovoltaics has yet to reach consensus on device characterization protocol and test conditions. The wide range of testing conditions in the field can make it challenging to make straightforward comparisons across experimental works, hence the thermodynamic efficiency framework presented in Chapter 2. Potential consensus on this topic is complicated by the diversity of cell bandgap and emitter temperatures; cells are often characterized at or near their optimal emitter temperature. While it is unlikely that emitter temperature and spectrum will become standardized, there are several aspects of TPV characterization protocol that could be improved throughout the field.

6.2.1 Calorimetric efficiency measurement

TPV researchers should strive to implement calorimetric techniques (i.e., direct measurement of heat rejection from the cell) for efficiency characterization. Calorimetric techniques have been used to characterize Si,[1] InGaAs,[2] and GaAs[3] TPV cells, but reports of TPV efficiency, including those presented in this thesis, generally rely on separate characterization of the cell's spectral and

electronic properties. Non-calorimetric approaches for efficiency characterization are less robust to cell and emitter non-idealities (for example, spatial variation in emitter temperature or cell reflectance) and are prone to introduce error by incorporating multiple experimental measurements. By contrast, calorimetric techniques can quantify the absorbed heat term in a single measurement.

Despite their appeal, calorimetric techniques appear to be more challenging to implement for small-area cells, as parasitic heat flow from the emitter through the heat sensor may exceed power generation in the cell at very small scales. This makes the approach less accessible during the early phases of device development before scale-up. As lab-scale demonstrations grow into sub-systems and prototypes, however, calorimetric efficiency characterization can provide a more accurate measurement of conversion efficiencies.

6.2.2 View factor

Standardization of the view factor between the emitter and cell during efficiency characterization will be crucial for continued development of thermophotovoltaic components and generators. Given the high current densities characteristic of TPV cells, these systems are highly susceptible to Ohmic losses associated with series resistance. Ohmic losses commonly become the limiting loss pathway as the view factor approaches unity, such that gains associated with high photocurrent (i.e., increased open-circuit voltage and fill factor) are entirely erased. Decreased cell performance at high view factors may also be indicative of cell heating in the absence of sufficient heat management. Therefore, optimal conversion efficiencies frequently occur for non-unity view

factors, as observed for the air-bridge cell in Chapter 4 of this thesis. Direct comparison of experimental works characterized at different view factors can therefore be misleading.

Researchers should strive to characterize performance metrics at high view factors approaching unity. If this is impractical because of limitations in experimental capabilities, simulated performance metrics for testing conditions outside the experimental range can provide appropriate context. Implementation of this practice throughout the field will help to close the performance gap between lab-scale TPV pairs and sub-systems identified in Chapter 2, section 2.6.

6.3 Opportunities in manufacturing and modular costs

Given current efficiencies and module costs, TPVs remain prohibitively expensive for widespread use. Here, I describe several opportunities for reduced cell costs, including operation at higher power densities, non-destructive epitaxial liftoff for reuse of the growth substrate, and larger scale cell production.

6.3.1 High power densities

One promising pathway to reduced cost ($/W) is leveraging high power densities, characteristic of local thermal emission. In theory, high power densities represent one of the TPV generator's greatest assets. In practice, however, Ohmic losses at high current densities can inhibit efficient conversion under high-intensity illumination. Utilization of a monolithically interconnected module (MIM) architecture reduces individual cell area and therefore enables low current operation that can alleviate the stringent series resistance requirements of TPV cells.[4] However,

small cells may reduce cavity efficiency and complicate scale-up. Accordingly, efficient operation at high power densities (>3 W cm^{-2}) remains a challenging problem that needs to be addressed.

6.3.2 Wafer reuse through non-destructive epitaxial lift off

A complimentary approach to lower costs is to grow multiple cells from a single growth substrate. Crystalline III-V substrates remain as the largest cost of TPV modules.[5] Recovery and subsequent reuse of the substrate after growth can therefore reduce cell costs considerably. This approach requires non-destructive liftoff (ND-ELO) techniques.[6,7] While Chapter 3 describes a fabrication technique compatible with ND-ELO, wafer reuse has not been demonstrated for cells in TPV systems. This manufacturing development will be crucial for enabling commercialization and improving process sustainability.

6.3.3 Production at larger scale

TPV module costs stand to benefit from production at a higher volume than current lab-scale manufacturing. Notably, this may require utilization of TPVs in high-volume applications, such as grid-scale thermal energy storage or residential co-generation. Alternatively, it may be necessary for cell fabrication techniques to make use of more mature technologies already in use for production of solar PV or telecommunication components. As development of high-quality Si cells for solar PV application benefitted from advances in integrated circuit technology, concurrent development of other materials for separate applications may expedite their deployment in TPV systems. For example, LM InGaAs and Ge photodiodes are commonly used for optical detection in the near-IR. Further, Ge and various InGaAsSb and InGaAs alloys are common sub-cell

materials in multi-junction solar PV technologies. Ongoing research efforts in these areas may benefit the performance and cost metrics of corresponding cell materials in TPV pairs.

6.4 Si TPV cells

As discussed at length in this thesis, it is desirable to adapt higher bandgap cell materials for use in TPV systems. Regarding TPV performance, higher bandgap materials generally achieve better bandgap utilization (i.e., higher open-circuit voltage relative to the bandgap). This translates to higher power output. Si is a leading candidate cell material among higher bandgap materials because of its technological maturity and superior cost metrics relative to III-V semiconductors. These factors make development of Si TPV cells one of the most promising directions for the field.

To operate Si TPV cells with competitive efficiencies at moderate emitter temperatures (i.e., <1700°C), it will be necessary for Si cells to realize similar out-of-band absorptance to that demonstrated for InGaAs cells in this thesis. My research collaborator Byungjun Lee recently reported preliminary findings on the development of a highly reflective proof-of-principle Si air-bridge structure.[8] Figure 6.1 shows that a Si optical structure with an air-bridge architecture is observed to exhibit ~97% out-of-band reflectance as weighted by a 1700°C blackbody emitter. Continued development of air-bridge Si TPV cells may ultimately enable practical use of the material for TPV systems, a prospect once thought impractical because of the bandgap-emitter temperature mismatch.

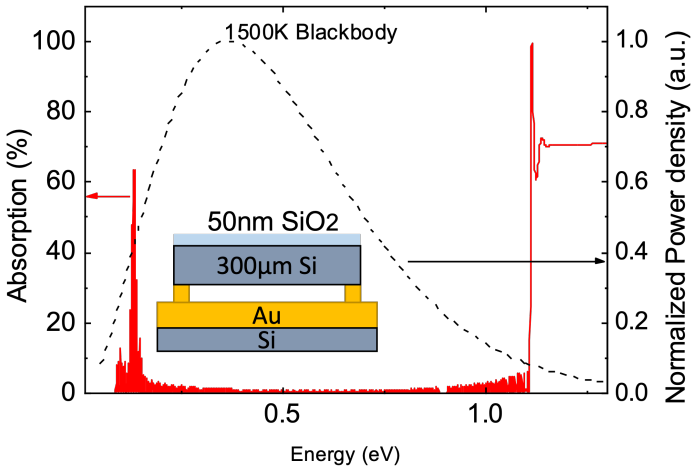

Figure 6.1. Preliminary air-bridge Si reflectance.

6.5 Tandem TPV cells

The benefits of implementing a tandem (i.e., multi-junction) cell architecture in a TPV system are two-fold. Firstly, tandem TPV cells enable decreased thermalization losses, similar to tandem solar PV cells. Secondly, as described in Chapter 2, section 2.6, addition of a secondary absorber layer can decrease current densities, therefore limiting Ohmic losses, and can decrease the cell's sensitivity to out-of-band losses.[9] Recent work from LaPotin, *et al.* reports >40% conversion efficiency for a tandem cell under illumination by an emitter at 2400°C,[10] demonstrating the benefits of reduce thermalization loss in tandem TPV cells.

Integration of the air-bridge architecture into a tandem TPV cell represents an opportunity to marry low out-of-band loss with decreased thermalization loss for high energy photons. Realization of this concept would enable spectral efficiencies surpassing the thermodynamic limits of photon management for single junction cells and conversion efficiencies exceeding 50%.[10]

Further, the air-bridge architecture has the potential to eliminate an additional loss pathway characteristic of tandem cells. The rear Au support grid at the back of a standard, single-juction air-bridge cell acts as a transparent conductor, enabling transmission of photons and conduction of electrons. I propose here the use of a secondary, intermediate Au support grid in place of a conventional tunnel junction. Use of such a secondary Au grid would eliminate any out-of-band free carrier absorption losses characteristic of conventional, highly doped tunnel junctions. Figure 6.2 depicts the described double air-bridge tandem architecture concept.

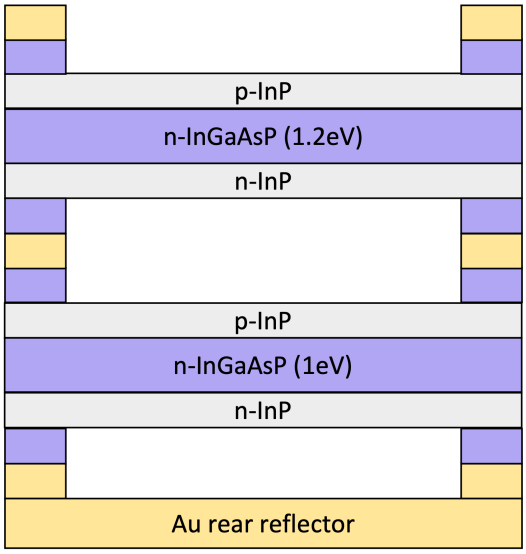

Figure 6.2. Double air-bridge architecture concept for tandem TPV cells. InGaAsP absorbers of variable compositions and bandgaps may be grown monolithically and lattice-matched to InP.

6.6 References

1. Swanson, R.M. (1980). Recent developments in thermophotovoltaic conversion. In 1980 International Electron Devices Meeting (IRE), pp. 186–189.
2. Narayan, T.C., Nizamian, D.P., Luciano, C., Johnson, B.A., Limpinsel, M., Young, A.R., Briggs, J.A., Kuritzky, L.Y., Ponec, A.J., Perl, E.E., et al. (2021). Platform for Accurate Efficiency Quantification of gt; 35% Efficient Thermophotovoltaic Cells. In 2021 IEEE 48th Photovoltaic Specialists Conference (PVSC), pp. 1352–1354.
3. Narayan, T.C., Kuritzky, L.Y., Nizamian, D.P., Johnson, B.A., Tervo, E.J., Young, A.R., Luciano, C., Arulanandam, M.K., Kayes, B.M., Perl, E.E., et al. (2020). World record demonstration of gt; 30% thermophotovoltaic conversion efficiency. In 2020 47th IEEE Photovoltaic Specialists Conference (PVSC), pp. 1792–1795.
4. Wilt, D., Wehrer, R., Palmisiano, M., Wanlass, M., and Murray, C. (2003). Monolithic interconnected modules (MIMs) for thermophotovoltaic energy conversion. Semicond. Sci. Technol. *18*, S209–S215.
5. Horowitz, K.A., Remo, T.W., Smith, B., and Ptak, A.J. (2018). A Techno-Economic Analysis and Cost Reduction Roadmap for III-V Solar Cells.
6. Lee, K., Zimmerman, J.D., Hughes, T.W., and Forrest, S.R. (2014). Non-Destructive Wafer Recycling for Low-Cost Thin-Film Flexible Optoelectronics. Adv. Funct. Mater. *24*, 4284–4291.
7. Lee, K., Shiu, K.T., Zimmerman, J.D., Renshaw, C.K., and Forrest, S.R. (2010). Multiple growths of epitaxial lift-off solar cells from a single InP substrate. Appl. Phys. Lett. *97*, 10–12.
8. Lee, B. (2021). Thin-Film III-V Devices for Low-Cost Detection and Energy Conversion.
9. Raman, V.K., Burger, T., and Lenert, A. (2019). Design of thermophotovoltaics for tolerance of parasitic absorption. Opt. Express *27*, 31757.
10. LaPotin, A., Schulte, K.L., Steiner, M.A., Buznitsky, K., Kelsall, C.C., Friedman, D.J., Tervo, E.J., France, R.M., Young, M.R., Rohskopf, A., et al. (2021). Thermophotovoltaic Efficiency of 40%. arXiv Prepr. arXiv2108.09613.